Gating of Sec61 in Posttranslational Translocation Across the Endoplasmic Reticulum

By

Samuel Itskanov

A dissertation submitted in partial satisfaction of the

requirements for the degree of

Doctor of Philosophy

in

Biophysics

in the

Graduate Division

of the

University of California, Berkeley

Committee in charge:

Professor Eunyong Park, Chair
Professor James Hurley
Professor Stephen G. Brohawn
Professor Eva Nogales

Summer 2022

Gating of Sec61 in Posttranslational Translocation Across the Endoplasmic Reticulum

By
Samuel Itskanov

Abstract

Gating of Sec61 in Posttranslational Translocation Across the Endoplasmic Reticulum

By

Samuel Itskanov

Doctor of Philosophy in Biophysics

University of California, Berkeley

Professor Eunyong Park, Chair

The endoplasmic reticulum (ER) is a major site for protein biosynthesis, required for production of about a third of all proteins in eukaryotic cells. The heterotrimeric Sec61 complex is a protein-conducting channel which mediates the transport or membrane integration of a majority of the ER-targeted proteins, such as secretory proteins and membrane proteins. Using a sophisticated gating mechanism, Sec61 transports soluble amino acid segments through its vertical water filled pore, and integrates hydrophobic transmembrane helices laterally into the membrane. The Sec61 channel translocates client polypeptides either co- or post-translationally. The posttranslational mode requires the formation of a larger complex with the membrane proteins Sec62 and Sec63. Substrate translocation further requires the essential ER resident Hsp70, BiP. The post translational complex in fungal species is additionally associated with the non-essential proteins Sec71 and Sec72. The structure and mechanism by which these proteins activate Sec61 for transport of client proteins has been poorly understood.

Using cryo-electron microscopy (cryo-EM), we determined the structures of several variants of the Sec61–Sec62–Sec63–Sec71–Sec72 complex (shortly, the Sec complex) from *Saccharomyces cerevisiae* and *Thermomyces lanuginosus* and showed that Sec62 and Sec63 induce opening of the Sec61 channel. The structures reveal that Sec63 is positioned in the back of Sec61 and interacts with Sec61 and Sec71-Sec72, while Sec62 is flexibly associated with the complex in front of the lateral gate. The J-domain of Sec63 is optimally positioned under the channel pore to bind BiP and enable efficient polypeptide translocation. Sec63 associates with Sec61 tightly through interactions in cytosolic, transmembrane, and ER-luminal domains. These extensive interactions pry open Sec61's lateral gate. Association of Sec62 further opens the luminal end of the lateral gate causing dislocation of the small helix blocking the pore called the plug domain. A simultaneous disruption of the cytosolic and luminal interactions of Sec63 with Sec61 completely closes the channel and abolishes its binding with Sec62. The structures and molecular dynamics simulations suggest that Sec62 may also prevent lipids from invading the channel through the open lateral gate. Our studies show how Sec63 and Sec62 work together in a hierarchical manner to activate Sec61 for post-translational protein translocation.

Dedication

I dedicated this dissertation to my mother, Stella Itskanov.

Acknowledgements

All this work could not have been completed without the mentorship and guidance of my dissertation committee chair, Eunyong Pak. I want to acknowledge the past and present members of the Park lab who have given me helpful advice and discussions, including Kyle Tucker, Sue Sim, Kyungjin Min and Yuanyuan Chen. Additionally, I want to thank the members of my dissertation committee James Hurley, Stephen Brohawn and Eva Nogales for helpful comments and discussions. I want to thank Stephen Brohawn's lab with whom we conducted lab meetings during the first two years of our lab's operation. A portion of this work and its successful publication could not have been accomplished without support from our collaborators, and I want to thank James C. Gumbart and Katie Kuo from Georgia Tech for their outstanding work. I want to thank Dan Toso, John Remis, and Paul Tobias for assistance in microscope operations.

I want to thank Kate Chase and everyone in the UC Berkeley Biophysics graduate program. The grants and funding sources that supported my education include the Carl & Betty Helmholz Gateway Fellowship at International House, the Molecular biology Training Grant (MBTG), Vallee Scholars Program (to E.P.) and the National Institutes of Health (grant no. R01-GM123169 to J.C.G.).

I want to acknowledge all the excellent scientist, good friends, and new connections I have made during my time as a student. These people include Jessica Castrejon, Raoul Martin, Jose P. Jacob, Orr Jacob, Daniyal Dar, Cameron Williams, and Julian Hassinger. Lastly, I want to acknowledge my family. My mother, Stella Itskanov, has worked tirelessly to support my education with unconditional love and faith in my success. My father, Aleksei Itskanov, has made tremendous sacrifices for me to live in this country and always strived to give me the best opportunities to fulfill my potential.

Table of Contents

List of Figures

Chapter One

A review of the Sec61 channel and summary of findings

Portions of this chapter are submitted for publication as:

Itskanov S, Park E. Mechanism of protein translocation by the Sec61 translocon complex. *Cold Spring Harb Protoc.* 2022

1.1 Introduction to the Sec61/SecY channel

The existence of the ubiquitous protein-conducting channel Sec61 (SecY in bacteria) was first hypothesized, over 50 years ago, as a "binding factor" between the endoplasmic reticulum (ER) and the ribosome which is also necessary for recognition of N-terminal sequences of secretory proteins (1). This channel is now known to be essential for the biosynthesis of a significant portion of any organism's proteome. The Sec61 channel is a heterotrimeric complex that forms a water filled pore which facilitates translocation of hydrophilic segments of polypeptides through the membrane and integration of transmembrane helices (TMs) into the membrane (2). In eukaryotes Sec61 resides in the ER membrane, while in archaea and bacteria, the channel resides in the plasma membrane. The client proteins of Sec61 may be destined to remain in the ER, be transported to other organelles such as Golgi and lysosomes, or secreted to the extracellular space through vesicular transport. The ER-targeting signal of a client protein, although poorly conserved, is characterized by a hydrophobic stretch of ~10–30 residues which tend to form an α-helix (3,4). This signal may be cleaved (N-terminal signal sequence) or retained in the membrane as a transmembrane helix (signal anchor) (5,6).

1.2 Channel architecture

The functional unit of the Sec61 channel is formed by the Sec61α subunit (Sec61p in yeast and SecY in bacteria), and it forms 10 TMs organized into two pseudo-symmetric halves: TMs 1-5 and TM6-10 (2) (Fig. 1.1A). These halves are thought to be rigid and move with respect to one another through a hinge located at the back of the channel. The front of the channel, as viewed from the membrane, utilizes this hinged motion to open and close the lateral gate where the signal sequence or signal anchor exits. A proper seal (Fig 1.1B, left panel) of the lateral gate is crucial to maintain separation of the channel interior from the membrane and should open only during lateral release of hydrophobic protein segments or if additional accessory proteins can function as alternate barriers. The seal is formed by TMs 2-3 on the N-terminal halve and TMs 7-8 on the C-terminal half. The central pore of the channel is hourglass shaped and is divided into two water-filled cavities facing the cytosol or the lumen. The center of the pore is lined by a predominately aliphatic and hydrophobic ring of residues, termed pore ring, which form a gasket-like constriction (7,8). Another small helix, between TM1 and TM2 (often denoted TM2a), is positioned at the luminal cavity of the translocation pore, and functionally serves as a vertical gate as it is displaced during substrate engagement. This "plug" stays firmly put in an inactive channel through hydrophobic interaction with the pore ring to prevent leakage of molecules and ions across the membrane.

The other two subunits of the channel complex, Sec61β and Sec61γ (Sbh1p and Ssh1p in yeast respectively, and SecG and SecE in bacteria respectively), serve primarily as structural support. The eukaryotic Sec61β is a non-essential single pass transmembrane protein and may have some minor variability between organisms (bacterial SecG contains an additional TM) (9–11). On the other hand, Sec61γ seems to play a more crucial role in stabilizing the channel. It has one long diagonal TM and the protein wraps around the back of the channel suggesting it may tension the channel halves together.

The gating of Sec61 and SecY has been studied extensively, and recent structural work has shown multiple binding partner and substrate dependent conformational states. Binding of the ribosome with Sec61 yields a “primed” channel (12) where the lateral gate widens partially in the cytosolic portion (Fig. 1.1C). Upon engagement with a substrate the channel’s lateral gate widens further and the plug is displaced by the substrate (13) (Fig. 1.1B,D). The extent of lateral gate binding has also been reported in a signal anchor complex (14) (Fig. 1.1E) and in bacterial SecY-SecA substrate engaged complex (11) (Fig. 1.1F), demonstrating that the channel is dynamic and can adopt a spectrum of conformational states.

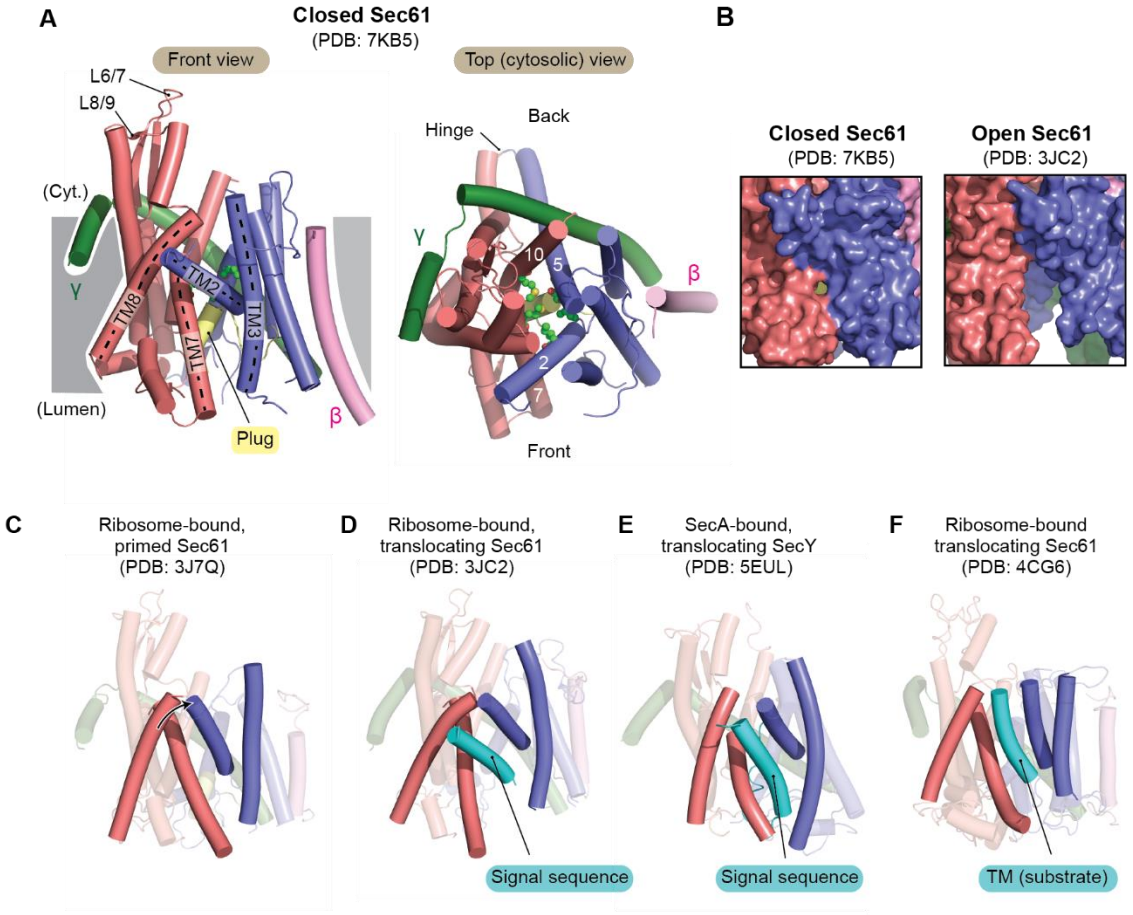

Figure 1.1 Architecture and gating mechanism of the Sec61 complex. A. Eukaryotic (yeast) Sec61 channel in a fully closed conformation. In the left panel, the lateral gate-forming TMs are indicated by dashed lines. In the right panel, the pore-forming TMs are indicated by numbers, and the pore ring residues are shown in green spheres**. B.** Surface representation of the lateral gate of the closed yeast Sec61 (left panel) and ribosome bound translocating Sec61 (right panel). Signal sequence is not shown. **C**. Lateral gate of primed Sec61 by a bound ribosome. A motion of TMs 2 and 3 (relative to the TMs 7 and 8) induced in priming of a closed channel is indicated by an arrow. **D**–**F**. Lateral gate of substrate-engaged Sec61/SecY complexes.

1.3 Functional modes of operation

In isolation, the Sec61 channel is closed and idle, and its activation requires recruitment of partner proteins. It can operate cotranslationally by forming a complex with the ribosome or posttranslationally with specialized proteins. While the cotranslational path is universally conserved in all organisms, the post translational path diverges between eukaryotes and bacteria, and the archaeal complex and mechanism is yet to be discovered. The utilization of these modalities is decided in part by the length of the client protein and the hydrophobicity of its signal sequence.

1.3.1 Cotranslational translocation

When a sufficiently hydrophobic signal sequence of a nascent polypeptide emerges from the ribosome, it is recognized by the M-domain of the signal recognition peptide (SRP) complex (15,16). SRP is a multi-subunit ribonucleoprotein that is associated with the ribosome. The interaction that is formed with between the M-domain and the nascent polypeptide is hydrophobic, and hydrophobic helices of varying lengths can bind the M-domain. Therefore, most signal sequences and all signal anchors utilize SRP for ER targeting. Upon recognition of the signal, a conformational change is induced in SRP which exposes its NG-domain to allow binding with the NG-domain of the SRP receptor (SR) on the membrane. The NG-domains of both these complexes are GTP binding proteins, and upon delivery of the substrate to Sec61, GTP is hydrolyzed and the complex breaks apart leaving the ribosome on Sec61 (17,18) (Fig 1.2).

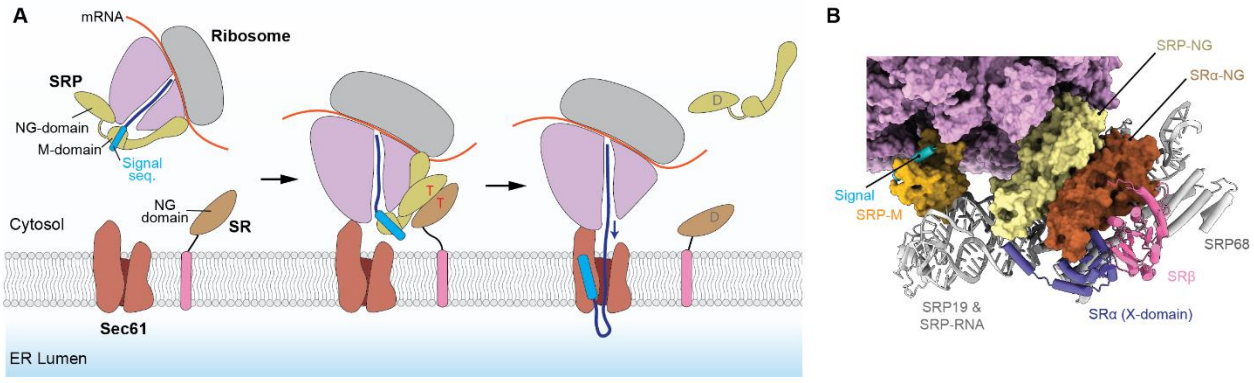

Figure 1.2 Co-translational targeting of nascent client proteins to the Sec61 complex. A. As the signal sequence or signal anchor emerges from the ribosome exit tunnel, it is recognized by SRP. The SRP targets the RNC to the ER membrane by an interaction with the ER-membrane protein SR. The ribosome docks onto the Sec61 complex. The

complex formation between the SRP and SR induces hydrolysis of two GTP molecules (indicated by “T”) each bound to the SRP and SR into GDP (indicated by “D”), and this leads to dissociation of the SRP–SR dimer. The signal and the following nascent polypeptide chain inserts into the Sec61 channel, followed by continued translocation of the polypeptide chain. **B**. Cryo-EM structure of an RNC–SRP–SR complex in a pre-handover state. (PDB 7OBQ; {Jomaa, 2021 #19}). Note that the mammalian SR is a heterodimeric complex formed by SRα (contains a NG domain) and SRβ (contains a membrane anchor, which is not shown).

1.3.2 Posttranslational translocation

If the signal sequence is able to evade the recognition of SRP due to insufficient hydrophobicity, or if the polypeptide is very short, the polypeptide will engage Sec61 posttranslationally. To enable peptide translocation, Sec61 forms a complex with two essential ER membrane resident proteins, Sec62 and Sec63 (19,20), which are conserved across eukarya, and in yeast the complex includes two additional, non-essential proteins, Sec71 and Sec72 (21). In addition to this core posttranslational complex (Sec complex) an ER resident HSP70 ATPase, BiP, is implicated in peptide translocation (22). Although the existence of Sec62 and Sec63 has been known for several decades, only a modicum of functional and structural data has been published. At its core, once a posttranslational client engages with Sec61, the J domain of Sec63, which is exposed to the lumen, promotes association of BiP with the emerging polypeptide. This interaction promotes ATP hydrolysis and tight binding of BiP with the polypeptide. By coating the emerging polypeptide with BiP molecules, backward translocation is prevented in a process termed Brownian ratcheting (23).

Although the overarching mechanism of eukaryotic posttranslational translocation has been established, the details have been absent. The human J domain of Sec63 is ~60 residues and represents only a minor structural domain of the full protein which is 760 residues. Furthermore, Sec62’s function remained entirely undefined. An understanding of the organization of these essential proteins with Sec61 is crucial to our understanding of their function within the context of posttranslational translocation. Structural studies of this complex and mutations of this complex may additionally shed a light on the intricacies of channel gating in the absence of ribosome.

There exist other molecular machineries that are capable of translocating protein onto the ER membrane posttranslationally. One class of these targeted proteins are C-terminal tail-anchored (TA) proteins. These membrane proteins have a single membrane spanning helix at their C-terminus, that evade SRP mediated targeting because translation completes before activation of the SRP pathway. The targeting of these clients can be achieve using the Get1-Get2 complex or the ER membrane complex (EMC) (24). Both Get1 and EMC3 are proteins that belongs to an evolutionarily separate class of insertases that include YidC and Oxa1 (25).

1.4 Modification of the client polypeptide during translocation

The fate of the different polypeptides that are translocated by Sec61 may diverge substantially after translocation, however, several key modifications are made during translocation or very shortly after. The modifying complexes are often associated with Sec61 to optimize the rate and consistency of these modifications. Recent publications have managed to capture many of these complexes with cryoEM and have shed light on their mechanisms.

The modification that most commonly occurs is the cleavage of the signal sequence. The composition of the signal sequence lacks obvious homology besides the presence of a short hydrophobic helical segment that is not long enough to fully span the membrane. Two other notable regions have been observed: a basic N-terminal region (N-region) which orients the N-terminus to the cytosol during translocations, and a neutral but polar C-terminal region (C-region) containing a cleavage site. While bacteria utilize a single protein, SPase I, to cleave signal sequences, the eukaryotic signal peptidase complex (SPC) contains 4 transmembrane subunits with multiple luminal and cytosolic domains. A structure of the human SPC has been modeled using cryo-EM and computational techniques (26). The structure reveal that the binding domain of the complex form a short cavity in the membrane that can accommodate the approximate length of the signal sequence, but not the length of a full transmembrane. Although SPases have been proposed to interact directly with Sec61 (27), how signal sequences arrive to SPase is currently unknown.

Another frequent modification that must occur in the ER is protein asparagine-linked glycosylation (N-glycosylation) (28). Both cotranslational and posttranslational clients are subject to glycosylation via two oligosaccharide transferases, OST-A and OST-B respectively. Functionally, both these complexes recognize the three-residue motif Asn-X-[Ser/Thr] (N-X-S/T; X can be any amino acid except proline), and attach a glycan to the amide nitrogen of the aspragine side chain. In mammals the composition of the two complexes is similar with partially overlapping subunits. The catalytic subunit in OST-A and OST-B is STT3A and STT3B respectively. The most notable and functionally relevant different between the two complexes is that OST-A contains the subunits DC2 and ribophorin 1 (RPN1). DC2 mediates the association of between the OST-A complex with Sec61, and RPN1 connects OST-A to the ribosome. The cryo-EM map of the OST-A bound to Sec61 and the ribosome reveals that the catalytic site of OST-A is ~6.5 nanometers away from the channel's site of egress, explaining both the efficiency of the process and why glycosylation sites that are very close to the signal sequence are often skipped (Fig 1.3).

The mammalian heterotetrameric TRAP complex has also been observed in the ribosome-Sec61-OST-A complex, positioned adjacent to the C-terminus of Sec61 opposite of OST-A (Fig 1.3). The function of TRAP is not fully characterized, but has been proposed to facilitate channel engagement of signal sequences (29,30) and be involved in N-glycosylation and topogenesis of certain client proteins (31,32). A large stable domain is visible clearly under the Sec61 channel, but higher resolution would be necessary to fully understand its functional role.

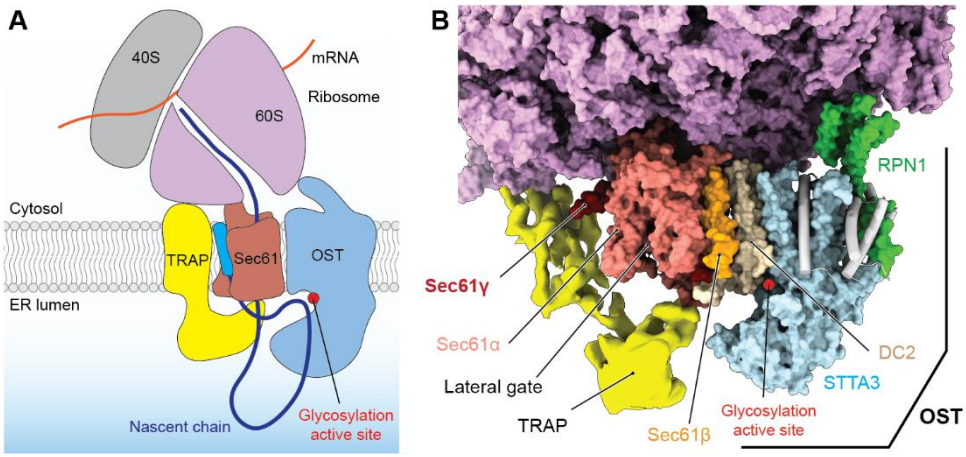

Figure 1.3 N-glycosylation by the oligosaccharyltransferase (OST) during co-translational translocation. Schematic diagram (A) and cryo-EM structure (B; PDB 6FTG) of a mammalian co-translational translocon complex containing the OST and TRAP. In B, the unmodeled TRAP complex (yellow) is shown with cryo-EM densities (EMD-4315). In addition to the STT3A, DC2 (OSTC), and RPN1 (OST1) subunits, the OST structure contains DAD1 (OST2), OST4, TMEM258 (OST5), OST48, and RPN2 (some are shown in gray and the other subunits are located behind STT3A).

1.5 Membrane protein integration by Sec61

Unlike soluble client polypeptides, proteins that are destined to span the membrane do not require a cleavable signal sequence. The topological arrangement the transmembrane helices (TMs) in a multispanning protein is a field of active study and the arrangement and orientation of the TMs can be categorized into multiple classes (for review see (33)). To understand how TMs are integrated, the simplest membrane protein would be a single spanning N-terminal TM. Similar to a signal sequence, the TM will be inserted into the channel as a loop with the N-terminus remaining in the cytosol (also referred to as “inside”). The orientation of N_{Cyt}-C_{Exo} is influenced by charge repulsion between the phospholipid head group and the N-terminus which is often negatively charged. The TM moves to the lateral gate as the rest of the peptide continues to translocate through the central pore (Fig. 1.4A).

When the membrane protein has more then one TMs, it may initiate translocation with N_{Cyt} configuration like the single TM situation described above. When the second TM (TM2) approaches the channel, it will engage the later gate with an inverse topology to TM1, creating a peptide loop in the ER lumen (Exo, also referred to as “outside”). This causes the downstream sequence of the peptide to stay in the cytosol until a third TM may re-engage with the channel pore. Since TM3 engages from the cytosol it will enter as a like TM1, and reversing the topology again. Subsequent TMs will follow these alternating topologies until all the TMs are integrated (Fig. 1.4B)

An inverted N_{Exo}-C_{Cyt} topology with the N-terminus in the ER lumen can also occur. The initial opposite insertion may be initiated with a signal sequence that enters with an N_{Cyt}-C_{Exo} conformation, which is eventually cleaved. However, it is believed that EMC may also function to insert the initial TM, followed by insertion of the remaining TMs by Sec61. Topologically, each TM will engage and disengage from the channel in an alternating fashion analogous to the N_{Cyt}-C_{Exo} case (Fig 1.4C). An erroneous N_{Exo}-C_{Cyt} insertion by Sec61 may be harmful to a cell, and a recently it was suggested that a P-type ATPase pump (P5A-ATPase) may act as a quality control factor that can extract mis-inserted TMs from the ER membrane (34).

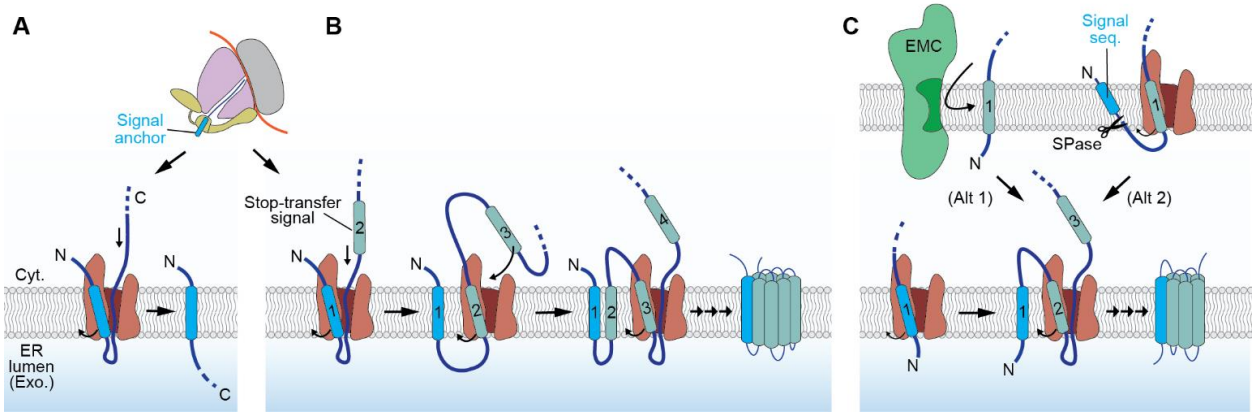

Figure 1.4 Membrane protein biogenesis by the Sec61 complex. **A**, Integration of the single-spanning membrane protein with an N_{Cyt}-C_{Exo} orientation. Integration occurs through a loop insertion as in the translocation of a secretory protein containing a signal sequence. **B**, A model for integration of a multi-pass membrane protein with the cytosolic N-terminus (N_{Cyt}). The first TM inserts as in panel A. The second TM releases into the membrane through the lateral gate when it reaches the central pore (thus this TM is often termed a stop-transfer signal). The third TM enables

re-engagement with Sec61 as a loop. **C**, A model for integration of a multi-pass membrane protein with the N-terminus in the ER lumen or extracellular side (N_{Exo}). A short N-terminus can directly be translocated by the Sec61 channel while the first TM integrates into the membrane through the lateral gate. The second TM engages with Sec61 in a loop configuration. Alternatively, the EMC inserts TM1 first, and then TM2 and the following segment are integrated by Sec61 (Alt 1). Some membrane proteins start with a cleavable signal sequence (cleaved later by the signal peptidase; SPase), which allows the TM1 and the preceding segment to insert with an N_{Exo}-N_{Cyt} orientation (Alt 2).

1.6 Summary of findings

We have employed cryo-electron microscopy (cryo-EM) techniques to solve structures of the heteroheptameric Sec complex from *Saccharomyces cerevisiae* (*Sc*Sec) and *Thermomyces lanuginosus* (*Tl*Sec) in multiple compositional, conformational, and mutated states. First, we discovered that the *Sc*Sec61 channel is in a fully opened conformation in the heteroheptameric Sec complex. The opening is prompted by extensive interaction with Sec63. Additionally, we found that a specific interaction between a Sec63 β-strand and Sec61 β-sheet tethers the J domain of Sec63 and stabilizes it for engagement with BiP.

From further cryo-EM structural analysis of the WT *Sc*Sec complex, WT *Tl*Sec complex and multiple mutational variants, we found that the Sec complex is a dynamic complex, and Sec63 and Sec62 can influence the gating of both the vertical and lateral gates of Sec61. Sec63 initially engages with the channel and opens the lateral gate while the plug remains immobilized. Contingent on this partially opened channel complex, Sec62 stabilizes in front of the lateral gate and induces further opening of the lateral gate in ER lumen side, which consequently disrupts the hydrophobic interactions between the pore ring and the plug, causing dislocation of the plug and opening of the vertical gate.

Chapter Two

Structure of the posttranslational Sec protein-translocation channel complex from yeast

Portions of this work were published as:

Itskanov S, Park E. Structure of the posttranslational Sec protein-translocation channel complex from yeast. *Science*. 2019 Jan 4;363(6422):84-87.

2.1 Introduction

The Sec61 protein-conducting channel mediates transport of many proteins, such as secretory proteins, across the endoplasmic reticulum (ER) membrane during or after translation. Posttranslational transport is enabled by two additional membrane proteins associated with the channel, Sec63 and Sec62, but its mechanism is poorly understood. We determined a structure of the Sec complex (Sec61-Sec63-Sec71-Sec72) from *Saccharomyces cerevisiae* by cryo–electron microscopy (cryo-EM).The structure shows that Sec63 tightly associates with Sec61 through interactions in cytosolic, transmembrane, and ER-luminal domains, prying open Sec61's lateral gate and translocation pore and thus activating the channel for substrate engagement. Furthermore, Sec63 optimally positions binding sites for cytosolic and luminal chaperones in the complex to enable efficient polypeptide translocation. Our study provides mechanistic insights into eukaryotic posttranslational protein translocation.

2.2 Results and discussion

2.2.1 Structure determination of the complex

To stabilize the posttranslational Sec complex in *Saccharomyces cerevisiae* and influence association of the Sec61 complex with the Sec62-Sec62 complex, we fused a copy of Sec61β to the N-terminus of the endogenous Sec63 locus and removed the endogenous Sbh1. Additionally, we attached a cleavable green fluorescent protein (GFP) to the C-terminus of the endogenous Sec63 locus and used resin conjugated with anti-GFP nanobodies for affinity purification. Upon solubilization in mild detergent and purification (see section 1.4.1-1.4.2) we determined a structure of the Sec complex at 3.7-Å resolution by cryo–electron microscopy (cryo-EM) (Fig. 2.1 and Fig. 2.9). Many side chains are clearly visible in the density map, enabling modeling of an accurate atomic structure (Fig. 2.1B). The map also allowed us to improve the model for the eukaryotic Sec61 channel, which was previously built into maps at ~4- to 5-Å local resolutions (12,35). However, Sec62 and the ER-luminal J domain of Sec63, which transiently interacts with BiP (22,36–38), were not sufficiently resolved for model building, likely because of their flexible motions (Fig. 2.1A).

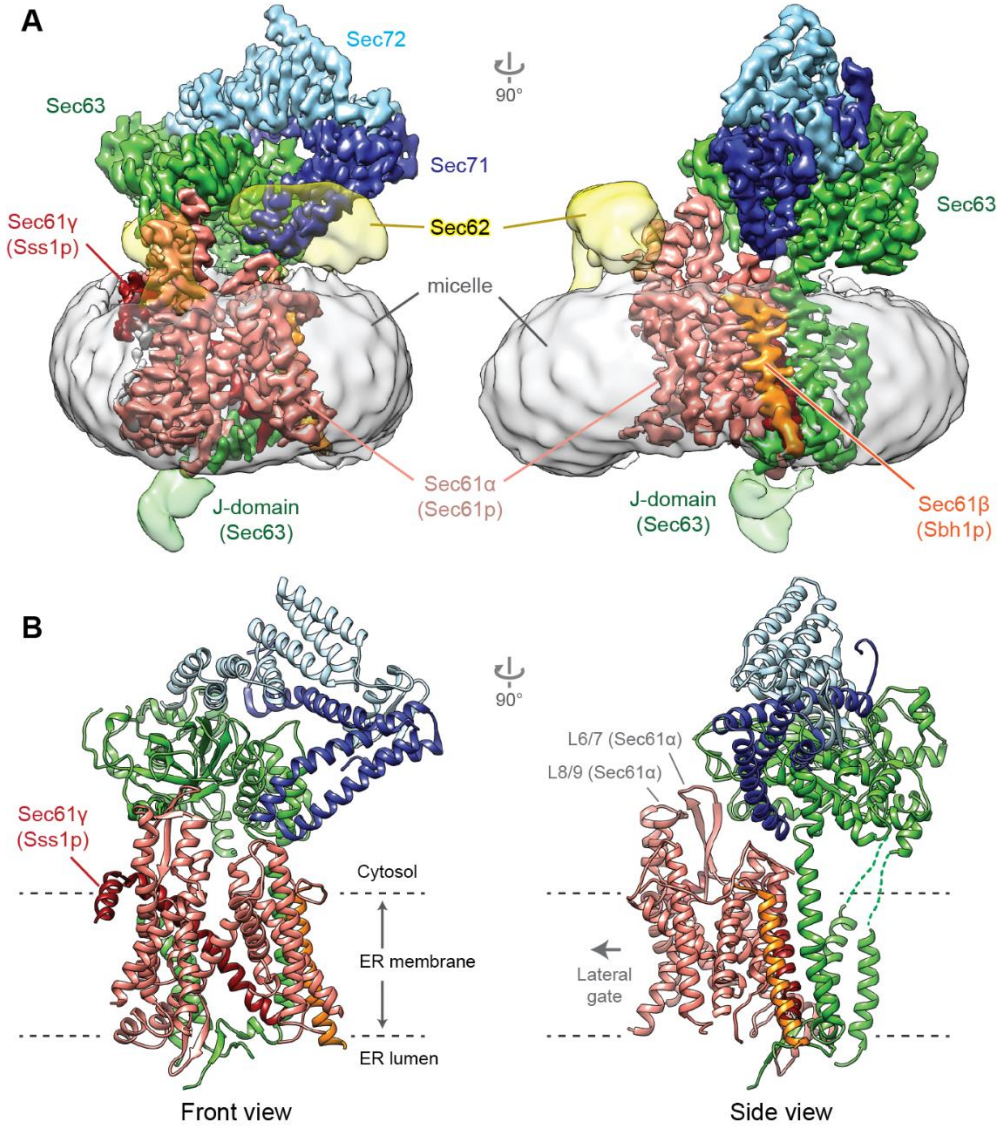

Figure 2.1 Structure of the yeast Sec complex. (A) Cryo-EM density map and **(B)** atomic model of the yeast posttranslational protein translocation complex. The front view is a view into the lateral gate.

Table 2. 1. Cryo-EM data collection, refinement and validation statistics

	*Sc*Sec Complex (EMD-0336, PDB 6N3Q)	Sec61PM *Sc*Sec Complex (Unpublished)	Sec61PM-Sec63βΔ6 *Sc*Sec Complex (Unpublished)
Data collection and processing			
Magnification	43,103x	64,000x	64,000x
Voltage (kV)	200	300	300
Electron exposure (e^{-}/Å^2)	50	48.8	48.8
Defocus range (μm)	-0.8 to -2.4	-0.8 to -2.5	-0.8 to -2.5
Pixel size (Å)	1.16	1.15	1.15
Symmetry imposed	*C*1	*C*1	*C*1
Initial particle images (no.)	358,961	195,916	294,118
Final particle images (no.)	208,049	92,820	142,228
Map resolution (Å)	3.68	3.64	4.51
FSC threshold	0.143	0.143	0.143
Map resolution range (Å)	3.42 – 9.18	3 – 10	3.5 – 11
Refinement			
Model resolution (Å)	3.7		
FSC threshold	0.5		
Map sharpening *B* factor (Å^2)	-104.7		
Model composition			
Non-hydrogen atoms	9,931		
Ligands	-		
B factors (Å^2)			
Protein	97.8		
Ligand	-		
R.m.s. deviations			
Bond lengths (Å)	0.006		
Bond angles (°)	0.972		
Validation			
MolProbity score	1.42 (97%)		
Clashscore	4.48 (95%)		
Poor rotamers (%)	0		
Ramachandran plot			
Favored (%)	96.84		
Disallowed (%)	0		

2.2.2 Architecture of the Sec complex

The structure reveals that Sec63 together with Sec71-Sec72 forms a large soluble domain, which sits on the cytosolic side of the Sec61 channel (Fig. 2.1). Sec63 consists of an N-terminal domain containing three TMs and a J domain between the second and third TMs and a C-terminal cytosolic domain (Fig. 2.3A-B). The cytosolic domain contains two a helical domains (HD1 and HD2) and an immunoglobulinlike [fibronectin type-III (FN3)] domain, which are arranged similarly to the homologous region of the Brr2RNA helicase (39). Sec71-Sec72, the structure of which is similar to a recent crystal structure of *Chaetomium thermophilum* Sec71-Sec72 (21), clamps Sec63's cytosolic domain like tongs.

Although a structural study of Sec62 is inaccessible due to its low resolution in this cryo-EM map, we can presume it resides in front of the lateral gate. Two cytosolic features are visible flanking both sides of the lateral gate (Fig. 2.1A), which likely represent the N-

and C-termini of the protein. Since Sec62 has two transmembrane helices, it is reasonable to assume that they will intercept the lateral gate to connect the cytosolic domains. Nevertheless, because the resolution here is too low, a more careful examination is necessary to verify this conjecture (see chapter 2).

2.2.3 Structure of Sec63

Sec63 makes extensive contacts with the channel through its transmembrane, cytosolic, and luminal domains, indicative of a major role in regulating the channel's function (Fig. 2.3C-E). In the membrane region, the TMs of Sec63 are located at the back (opposite from the lateral gate) of the Sec61 channel, interacting with the TMs of Sec61β and Sec61γ as well as TM1 and TM5 of Sec61a (Fig. 2.3C). Considering the extensive interactions between these elements, the TMs of Sec63 likely make a main contribution to the association between Sec61 and the rest of the Sec complex. In the cytosolic region, the FN3 domain of Sec63 interacts with the loop between TM6 and TM7 (L6/7) of Sec61a through antigen-antibody–like binding. Like other FN3 domains, FN3 of Sec63 has a canonical b-sandwich fold composed of seven b strands (referred to asA to G) but contains unusually long A-B, B-C, and D-E interstrand loops (Fig. 2.2). With both A-B and B-C loops, FN3 creates a binding surface for L6/7, which uses a combination of surface complementarity and electrostatic and hydrophobic interactions (Fig. 2.2E).

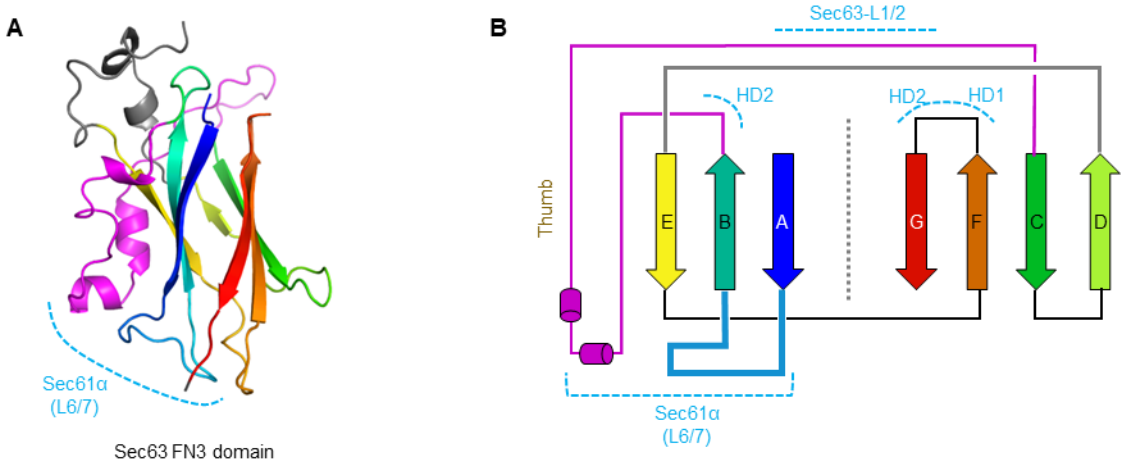

Figure 2. 2 Structure of Sec63 FN3 domain. A. Yeast Sec63 FN3 domain. **B**. schematic representation of Sec63 fibronectin type-3 (FN3) domain. β sheets are depicted as arrows and two small α-helices in the "thumb" are depicted as cylinders. Regions which interact with other parts of the Sec complex are highlighted with cyan dashed lines. The color schemes in B follows that of A.

Although sequence conservation is not obvious, metazoan Sec63s have similar extensions in the A-B and B-C loops. We expect analogous interactions between Sec63 and Sec61 in other eukaryotes. The interaction between FN3 and L6/7 is noteworthy because L6/7, together with L8/9, forms a docking site for the ribosome (12,40,41). Accordingly, superimposition of the Sec complex with a ribosome-bound Sec61 structure shows massive steric clashes between the ribosome and the cytosolic domains of Sec63 and Sec62, explaining why Sec61 in the Sec complex cannot bind to the ribosome (22,42). In the ER luminal side, a segment preceding TM3 of Sec63 is directed into the luminal funnel of the Sec61 channel through the crevice present between TM5 of Sec61a

and the TM of Sec61g (Fig. 2.3D). This segment makes an antiparallel β sheet together with a β hairpin looping out in the middle of Sec61a's TM5. This β-augmentation is further buttressed by hydrophobic interactions with the N-terminal segment of Sec63. These features are highly conserved throughout eukaryotes and thus likely play an important role in optimal positioning of the J domain.

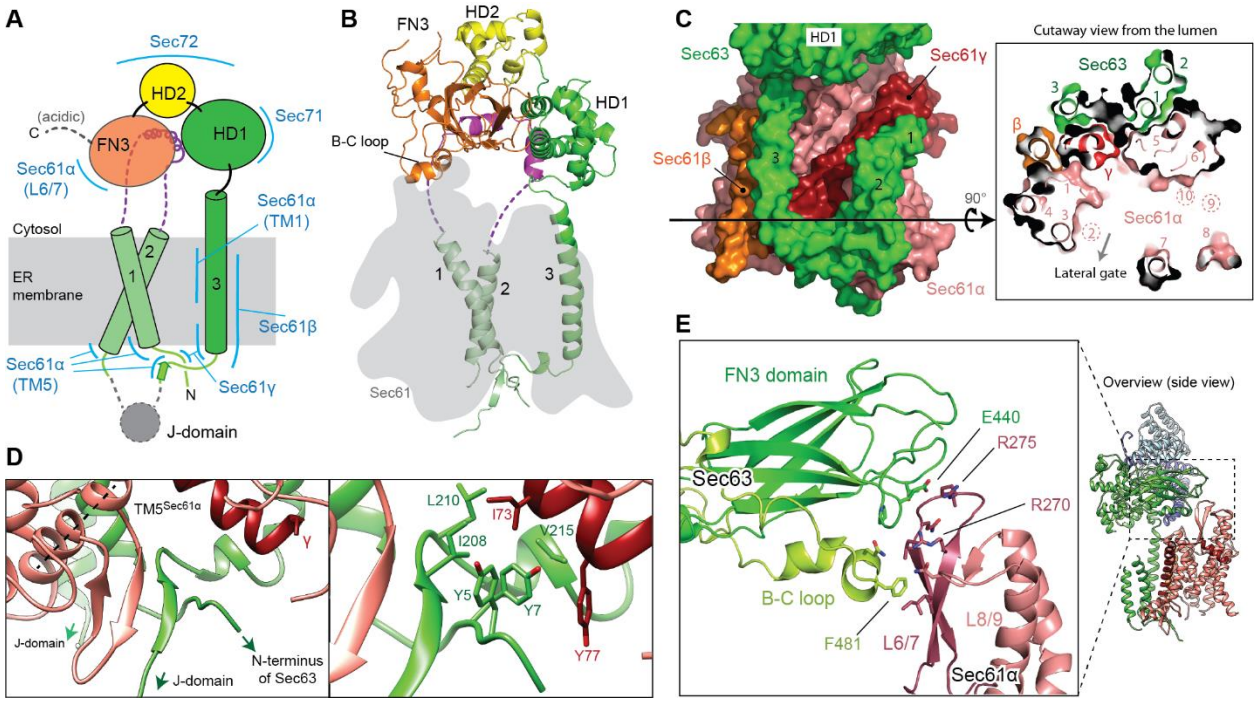

Figure 2.3 Structure of Sec63 and its interactions with the channel. (A) Schematic of Sec63 domains. Regions interacting with other parts of the complex are indicated by blue lines. Unmodeled regions are shown with dashed lines. **(B)** Structure of Sec63 (front view). The position of Sec61 is shaded in gray. **(C)** Interactions between TMs of Sec63 and Sec61. On the left is a view from the back; on the right is a cutaway view from the ER lumen. The black arrowed line represents the cross-sectional plane. TMs 2, 9, and 10 of Sec61a are located above the cross-sectional plane. **(D)** Interactions between Sec63 and Sec61 in the luminal side. On the left is a b sheet formed between Sec61a (TM5 indicated by a dashed line) and the segment between Sec63 TM3 and the J domain. On the right is a magnified view with side chains shown as sticks. **(E)** Interactions between the FN3 domain and the cytosolic loop L6/7 of Sec61a (also see Fig. 2.1B). L, Leu; I, Ile; V, Val; Y,Tyr; E, Glu; R, Arg; F, Phe.

2.2.4 The Sec61 channel is fully open

One pronounced feature of the Sec complex structure is a fully open channel (Fig. 2.4, A and B). The Sec61/SecY channel has a characteristic clamshell-like topology, in which its central pore can open toward the lipid phase through the lateral gate formed between TM2 and TM7. Compared with previous Sec61/SecY structures (2,9,11–13,43), the channel in the Sec complex displays a substantially wider opening at its lateral gate, through which a signal sequence can readily pass as an a helix (Fig. 2.4 and Fig. 2.5). This contrasts with structures of channels associated with the ribosome or the bacterial posttranslational translocation motor SecA (9,11–13,43), in which the channel shows an only partially open lateral gate (Fig. 2.4, C to F), which was proposed to be further opened by interaction with the hydrophobic signal sequence during the initial substrate insertion.

The opening is achieved by a largely rigid-body movement between the two halves (TMs 1 to 5 and 6 to 10) of Sec61a and additional motions of the lateral gate helices. The fully open conformation appears to be a result of the extensive interactions with Sec63. For example, binding between FN3 and L6/7 perhaps pulls the C-terminal half of Sec61a to open the lateral gate. However, further investigation will be necessary to understand the precise mechanism and the dynamics of channel gating in the native membrane environment. At the open lateral gate slit, there is a weak density feature, which likely represents bound detergent molecules (Fig. 2.4, A and B). In the native membrane, lipid molecules may occupy this site and facilitate initial binding of signal sequences.

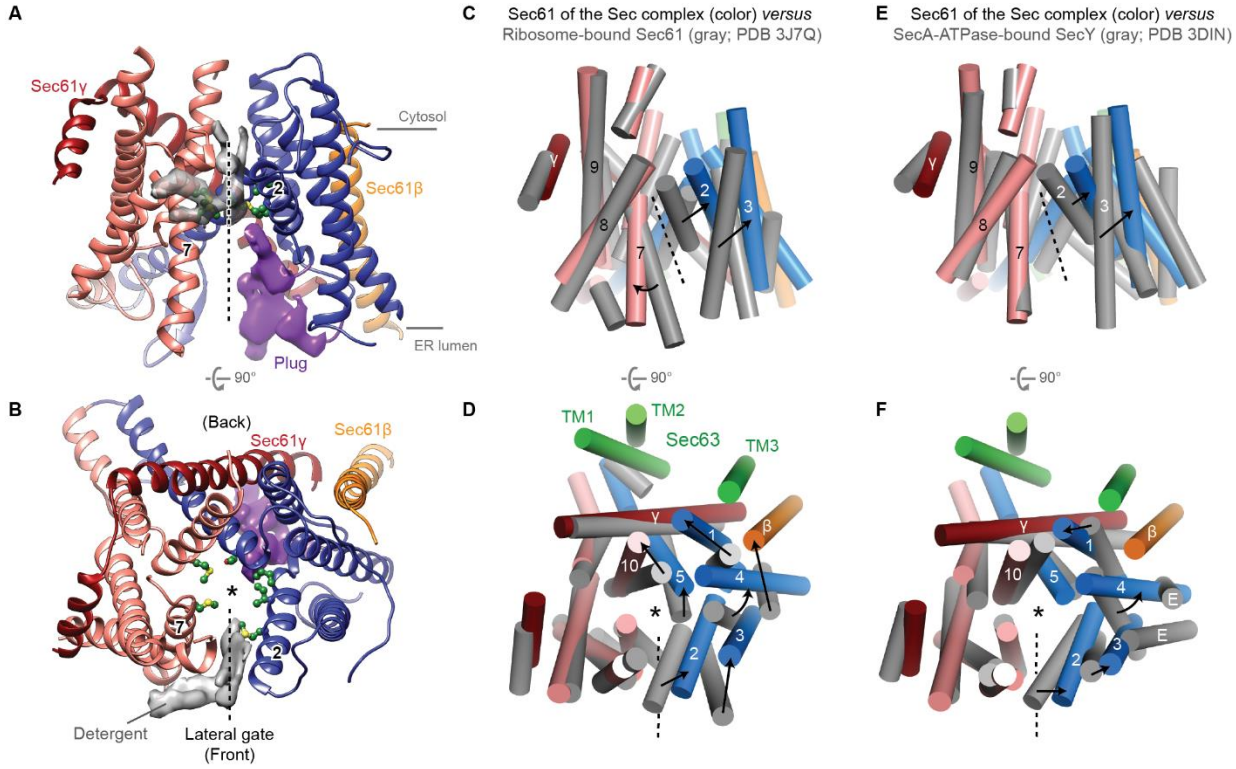

Figure 2.4 A fully opened Sec61 channel in the Sec complex. (**A** and **B**) Structure of the Sec61 channel. The N- and C-terminal halves of Sec61a are in blue and salmon, respectively. The gray density feature is presumed detergent molecules. Pore lining residues are shown as green balls and sticks. The density feature for the plug is in purple. Numbers "2" and "7" indicate TM2 and TM7, respectively. (**C** to **F**) Comparison of Sec61 of the Sec complex (colored) with Sec61 of the cotranslational ribosome-Sec61 complex [gray; (C) and (D)] or SecY of a bacterial posttranslational SecA-SecY channel complex [gray; (E) and (F)]. The structures are aligned with respect to the C-terminal half of Sec61a [(C) to (F)]. Shown are the front [(A), (C), and (E)] and cytosolic [(B), (D), and (F)] views. Numbers indicate corresponding TMs. Dashed lines represent the lateral gate. Asterisks indicate the translocation pore. For simplicity, L6/7 and L8/9 of Sec61a are not shown. In (D) and (F), TMs of Sec63 are also shown (green). In (F), TMs of SecG are indicated by "G." Also see Fig. 2.5A-D for comparisons to archaeal SecYand substrate-engaged channels. ATPase, adenosine triphosphatase; PDB, Protein Data Bank.

Our channel structure likely also represents a fully open state of the translocation pore (Fig. 2.4B and Fig. 2.5). The radius of the pore constriction is ~3 Å, large enough to pass an extended polypeptide chain. The opening would also permit passage of small hydrated ions and polar molecules in the absence of a translocating polypeptide (7,44), although the relatively positive electrostatic potential around the pore may disfavor

permeation of positively charged species (Fig. 2.5H). Yeast Sec61 has a relatively less hydrophobic pore constriction compared with nonfungal Sec61 and prokaryotic SecY (Fig. 2.5G). In prokaryotes, reduction of hydrophobicity in the pore constriction has been shown to lead to membrane potential dissipation (7), and similarly, in higher eukaryotes it might cause calcium leakage from the ER. However, yeast may tolerate ion leakage because calcium is stored primarily in the vacuole. In resting or primed channels, the pore is closed or narrow (<2 Å in radius) and further blocked by a small a-helical plug in the luminal funnel (2,9,12). By contrast, in our structure, the plug seems flexible and displaced from the pore (Fig. 2.4, A and B).

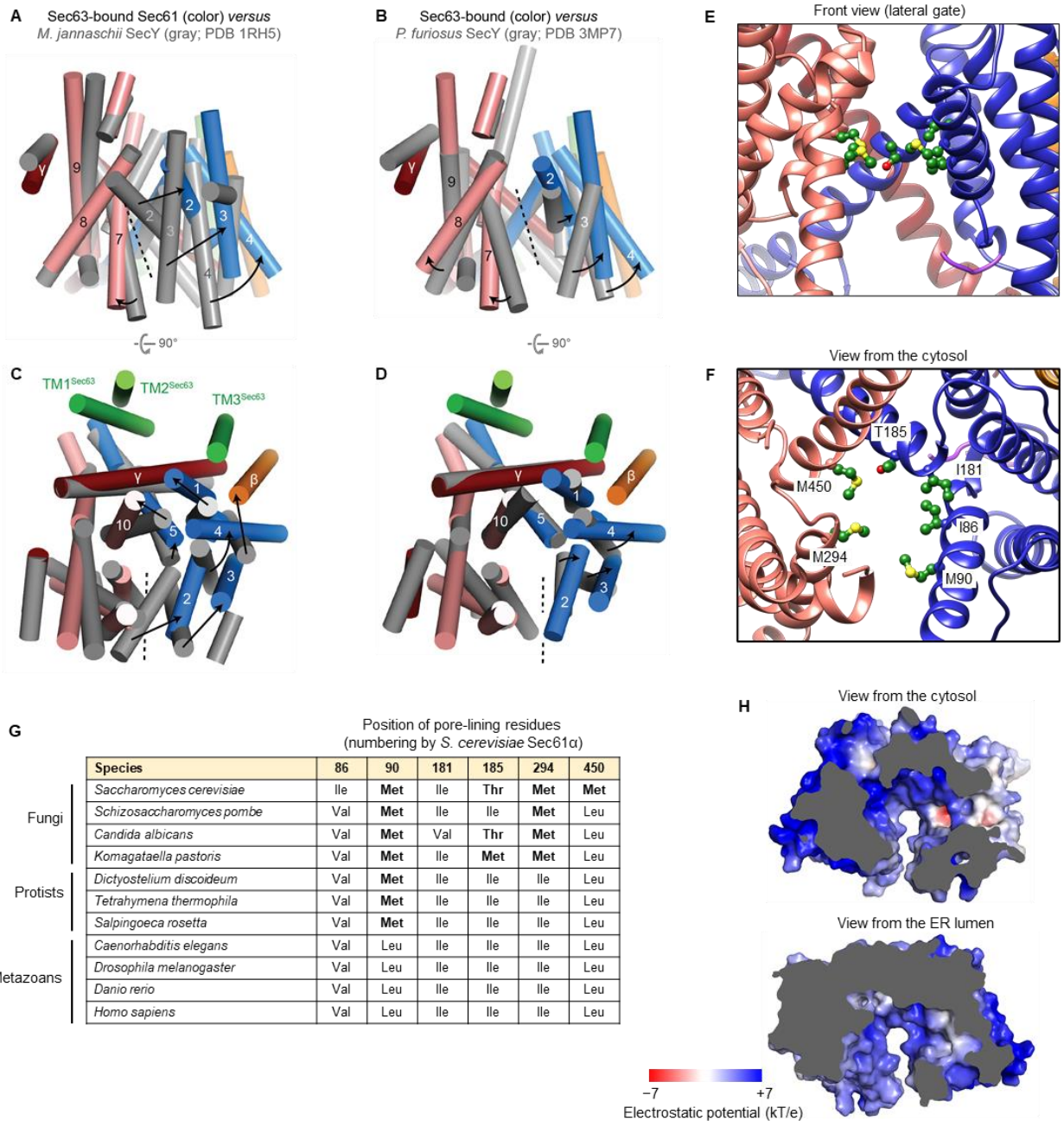

	Species	86	90	181	185	294	450
Fungi	*Saccharomyces cerevisiae*	Ile	**Met**	Ile	**Thr**	**Met**	**Met**
	Schizosaccharomyces pombe	Val	**Met**	Ile	Ile	**Met**	Leu
	Candida albicans	Val	**Met**	Val	**Thr**	**Met**	Leu
	Komagataella pastoris	Val	**Met**	Ile	**Met**	**Met**	Leu
Protists	*Dictyostelium discoideum*	Val	**Met**	Ile	Ile	Ile	Leu
	Tetrahymena thermophila	Val	**Met**	Ile	Ile	Ile	Leu
	Salpingoeca rosetta	Val	**Met**	Ile	Ile	Ile	Leu
Metazoans	*Caenorhabditis elegans*	Val	Leu	Ile	Ile	Ile	Leu
	Drosophila melanogaster	Val	Leu	Ile	Ile	Ile	Leu
	Danio rerio	Val	Leu	Ile	Ile	Ile	Leu
	Homo sapiens	Val	Leu	Ile	Ile	Ile	Leu

Figure 2.5 Opened lateral gate and translocation pore of Sec61 in the Sec complex. A–D, as in Fig 2.3 C, E, D and F, but the Sec61 channel was compared with the "closed" *M. jannaschii* SecY channel structure (PDB ID: 1RH5) (A and C) or the "open" *P. furiosus* SecY channel structure (PDB ID: 3MP7) (B and D). Shown are front (A and B; view into the lateral gate) and top (C and D; view from the cytosol) views. The N- and C- terminal halves of yeast Sec61α are shown in blue and salmon. To show a relative movement between the two halves, the structures are aligned with respect to the C-terminal half. Sec61β and Sec61γ are shown in orange and red, respectively. *M. jannaschii* and *P. furiosus* SecY channels are in gray. Numbers indicate corresponding TMs. In C and D, the TMs of Sec63 are also shown (green). Dashed line, lateral gate. Note that *P. furiosus* SecY was crystallized in an open state. Although the mechanism of this opening is unclear, it has been suggested that this occurred by interactions between the TM10s of two neighboring SecY molecules in a crystal contact (Egea and Stroud, 2010). Also note that yeast Sec61 is significantly more open than *P. furiosus* SecY. **E** and **F**, magnified views into the yeast Sec61 pore ring. **G**. comparison of the Sec61 pore ring amino acids from various species. **H**, surface electrostatic potential of Sec61's cytosolic (upper panel) and ER luminal (lower panel) funnels.

2.2.5 The Sec63 β-tether stabilizes the J domain

To determine whether the β-augmentation provides a tether for the J domain we tested the viability of yeast with deletions in the Sec63 β-strand. We transformed yeast with the chromosomal Sec63 controlled under tetracycline-repressible promoter (45) with centromeric autonomously replicating (CEN/ARS) plasmid expressing mutated Sec63 under endogenous promoter. Expression of Sec63 with deletions in the β-strand were not unable to fully rescue cell viability, and the phenotype was exacerbated in lower temperatures (Fig 2.6B). Although activity of BiP in different temperatures is unknown, the sensitivity in lower temperature is consistent with reduced activity of BiP as a function of being a heat-shock protein.

The hydrophobicity of the pore ring of Sec61 may be a variable in modulating how wide the channel opens, where increasing hydrophobicity would disfavor opening. Since the yeast pore ring is less hydrophobic than other organisms (Fig. 2.5G), it may favor an active translocating complex. Introduction of hydrophobic residues may therefore compound the effects of β-tether deletion. We mutated the pore ring residue to emulate those found in humans (M90L/T185I/M294I/M450L, termed Sec61PM) (Fig. 2.5E-G). While the Sec61PM mutation on its own does not affect yeast viability, a combination of Sec61PM with deletion of Sec63 β-tether was more lethal than either alone (Fig. 2.6C). To verify that the effect was the dislocation of the J domain we obtained cryo-EM maps of each of these mutants and found that deletion of the β-tether caused a complete disappearance of the J domain density (Fig 2.6D).

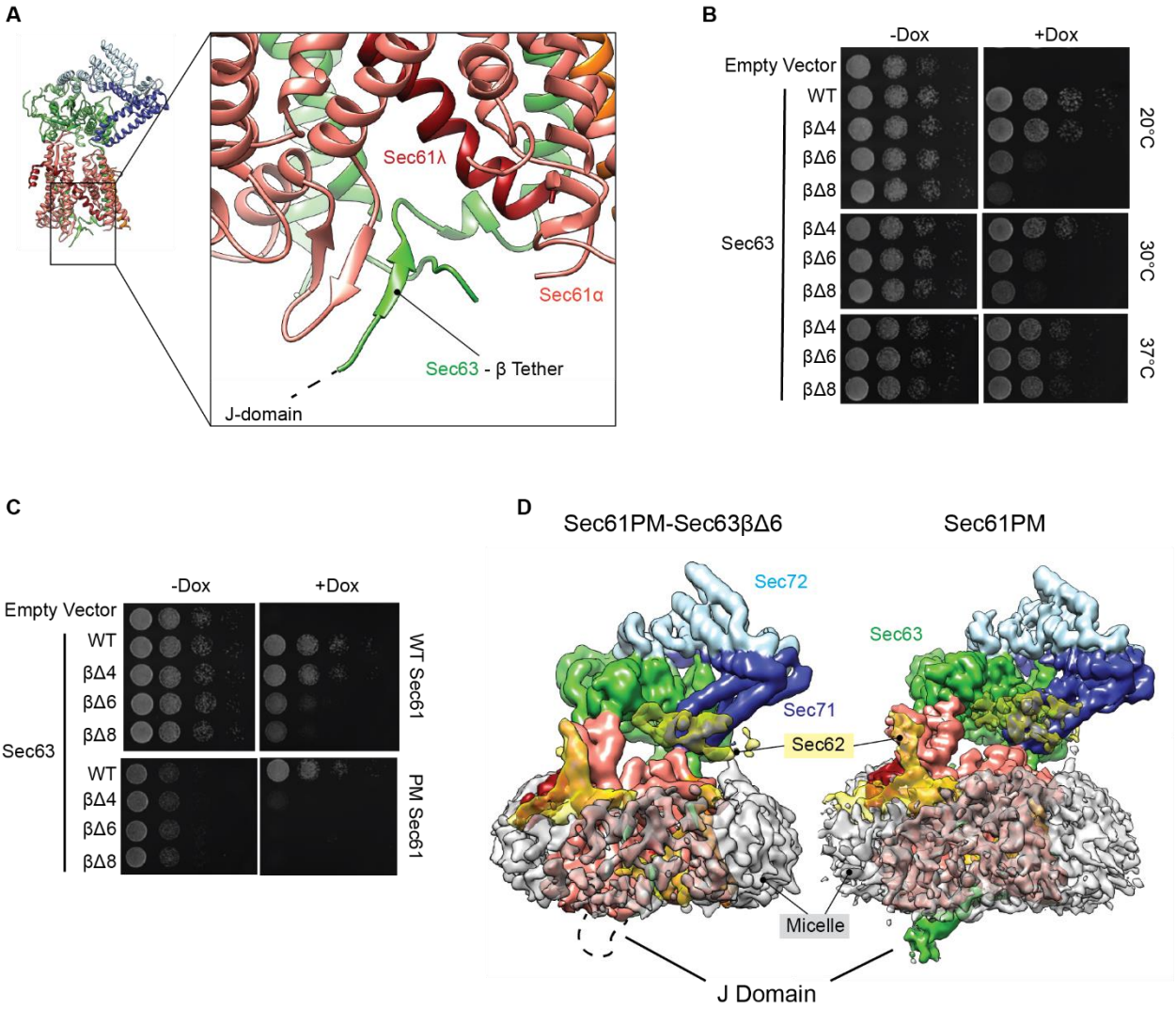

Figure 2.6 J domain is disordered when Sec63 β-tether is deleted. A. Magnified view of the β sheet interaction of Sec63 with sec61 to form the β tether. **B.** Spot test analysis of deletion of 4, 6 or 8 residues (starting at residue 205) of the Sec63 β tether at 3 different temperatures. Cells with endogenous Sec63 under the control of tetracycline-repressible promoter (45) were transformed with CEN/ARS plasmids with mutated Sec63, and 10 µg/ml doxycycline (Dox) was added to repress endogenous Sec63 expression **C**. Same as (b) but endogenous Sec61 pore ring residues were mutated to be more hydrophobic (M90L/T185I/M294I/M450L). **D**. Cryo-EM maps of Sec61 with pore ring mutation (Sec61PM, right) and combined pore ring mutation and deletion of 6 residues in the Sec63 β tether (Sec61PM Sec63 βΔ6, left). The absent J domain is outlined with dashed curve.

The spatial arrangement of Sec63 and Sec71- Sec72 with respect to the Sec61 channel suggests how these components play roles in accepting a polypeptide substrate from a cytosolic chaperone and handing it over to the channel and subsequently to BiP. Studies of *C. thermophilum* Sec72 have suggested that Sec72 provides a docking site for the cytosolic Hsp70 chaperone Ssa1p (21), which prevents substrates from premature folding or aggregation before translocation (20). Superimposition of the cocrystal structure of Sec72 and an Ssa1p C-terminal tail shows that the Ssa1pbinding site is ~60 Å above

the channel's pore (Fig. 2.7A). While the cytosolic domain of Sec63-71- 72 sits on top of Sec61, its position is tilted such that the polypeptide can insert straight down to the pore. Similarly, Sec62 is also positioned off the translocation path (Fig. 2.1A). Thus, upon release from Ssa1p, a substrate would efficiently engage with the pore without obstruction. The structure also allows us toproposehowBiPHsp70 may catch the substrate in the ER lumen. Despite the low resolution of the J domain (Fig. 2.1A), we could dock a homology model into the EM density map based on the shape of the feature and the orientations of the flanking segments (Fig. 2.7A). We then superimposed a recent crystal structure of a bacterial J domain–Hsp70 complex (46) to our EM structure (Fig. 2.7A). This modeling exercise showed that a peptide-binding cleft of the Hsp70 [called substrate-binding domain b (SBDb)] would be placed directly below the translocation pore. Thus, the J domain seems optimally positioned to allow BiP to grasp the substrate polypeptide as it emerges from the channel.

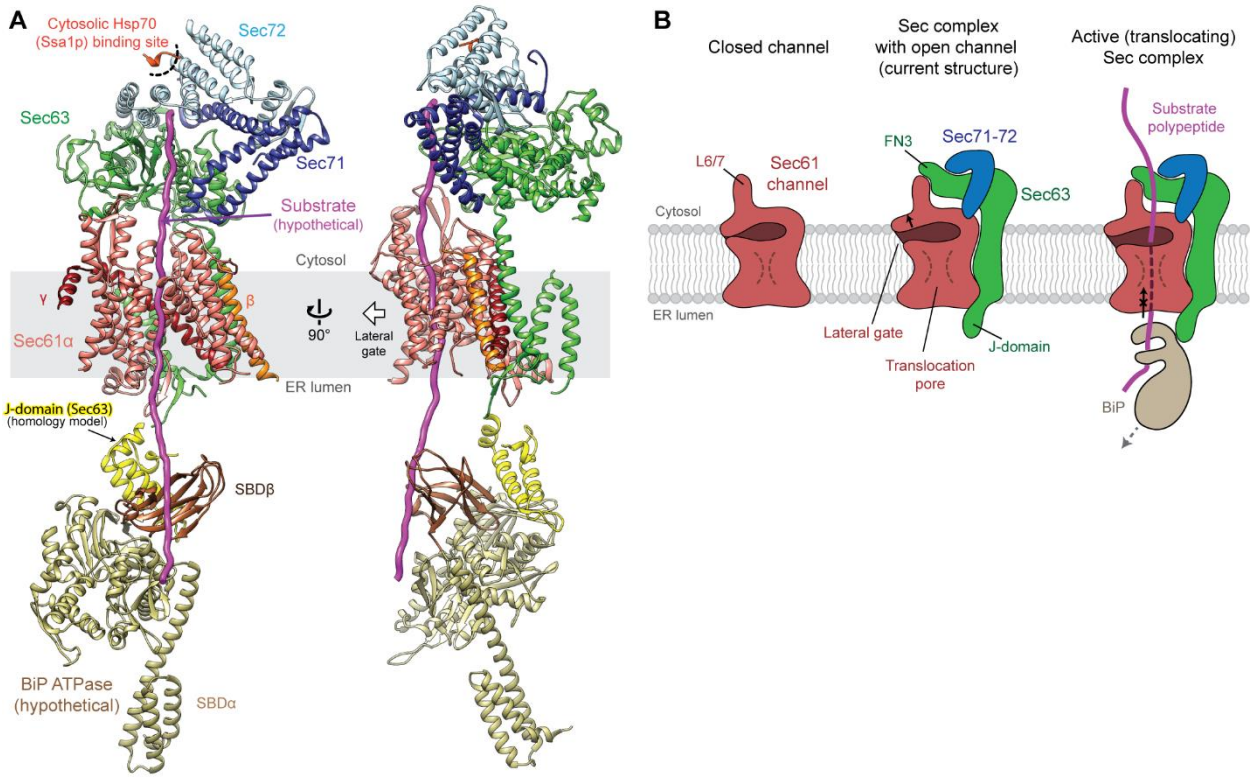

Figure 2.7 Model of an active translocation complex. A. The Sec complex structure superimposed with an Ssa1p C-terminal peptide (red orange; PDB ID: 5L0Y) and DnaK Hsp70 as a model for BiP (yellow and brown; PDB ID: 5RNO). **B.** Schematics for a closed Sec61 channel in isolation (left), an open channel in association with Sec63 (middle), and an active Sec complex engaged with a substrate [right; corresponding to the model in (A)].

2.3 Conclusion

Our cryo-EM maps and structure offer a model for how Sec63 enables posttranslational translocation (Fig. 2.7B) and provides a more complete picture of how the Sec61/SecY channel works together with different binding partners (i.e., ribosomes, Sec63, or SecA)

to enable transport of a range of substrates. Association of Sec63 seems to induce full opening of the channel, a conformation in which the channel can readily accept a substrate polypeptide. Such a conformation, compared with a partially open channel seen with the other modes, is likely advantageous for many posttranslational-specific substrates, which tend to have a less hydrophobic signal sequence (47–49). Additionally, the proper placement of the J domain is tied to an short β-sheet formation with Sec61, without which yeast viability is hindered and the J domain become too flexible to be captured by cryo-EM.

2.4 Material and Methods

2.4.1 Construction of plasmids and yeast strains

To enable efficient purification of the endogenous heptameric Sec complex from yeast, *Saccharomyces cerevisiae* strain BY4741 was modified to encode the fusion protein of Sbh1p (Sec61β)–Sec63p–GFP (green fluorescent protein) from the SEC63 locus. In addition, the fusion construct contains a 15-amino-acid Gly/Ser linker between Sbh1p and Sec63p (amino acid sequence: …GKLF (Sbh1p)–GGSGGSGGSGGSGGS (linker)–PTNY…(Sec63p)) and a tobacco etch virus (TEV) protease cleavage site between Sec63 and GFP (amino acid sequence: …ESPE (Sec63p)–AGGATTASGTG (linker)–ENLYFQG (TEV site)–TASGGGS (linker)–KGEELF…(GFP)). To attach the GFP tag to the C-terminus of Sec63p, a PCR product was generated to contain a 50-bp 5’ homology arm (immediately before the SEC63 stop codon; 5’-at act gat atc gat acg gat aca gaa gct gaa gat gat gaa tca cca gaa-3’), TEV, GFP, a nourseothricin resistance cassette, and a 50-bp 3’ homology arm (downstream of SEC63; 5’-cat ttt agc tct tag acg tat ata ttt cat ctt tat aaa aat aga tac at-3’). DNA was introduced to yeast cells by a standard lithium acetate/polyethylene glycol transformation protocol, and the cells were placed on a YPD agar medium (1% yeast extract, 2% peptone, 2% glucose, and 2% bacto-agar) containing 100 μg/mL nourseothricin. Colonies were isolated after 2 days at 30°C and recombination was confirmed by PCR. Fusion of Sbh1p and Sec63 was carried out similarly. We first generated a pGEM vector containing a ~3-kb genomic fragment in the SEC63 (~2kb upstream and ~1kb downstream of the SEC63 start codon), and then the OSW1 gene (upstream of SEC63) was replaced with hygromycin resistance cassette. This was then followed by insertion of the SBH1 coding sequence and a Gly/Ser linker immediately upstream of the SEC63 start codon). The resulting pGEM was linearized by restriction enzymes and used for transformation. Integration of the Sbh1p-encoding segment was confirmed using Sanger sequencing. The endogenous copy of SBH1 was replaced with a G418 resistance marker (5’-homology arm: 5’-ggg aaa aga ttt caa cca cca ctt caa aac acc aca ctc tac ctc cta cca tac tcc ata-3’; 3’-homology arm: 5’-taa gaa ttt tct tca gta atg att cag ctt tta tcc acc cta ttt gac aaa aca aga cta-3’) and the deletion was confirmed by PCR. The resulting strain, named ySI7, grew comparably to the wild-type, indicating that the fusion does not interfere with protein translocation in vivo. In addition to the fusion, we also slightly overexpressed the remaining five subunits of the heptameric complex (Sec61p, Sss1p, Sec62p, Sec71p and Sec72p) using a yeast CEN-ARS plasmid (with a URA marker) containing each gene (under their own endogenous promoter) in tandem. We note that transformation of this plasmid did not significantly change the band

intensities of subunits in SDS-PAGE (data not shown), suggesting that Sec63 was already saturated without the plasmid.

To enable purification of the PM *Sc*Sec complex, we generated strain ySI8a by modifying ySI7. We first clone the complete SEC61 gene (from 1,965 bp upstream to 668 bp downstream of the Sec61-coding sequence (CDS) of BY4741) upstream of the nourseothricin (NAT) cassette of the pSK-B399 plasmid (a gift from S. Klinge, Rockefeller University). We then inserted 543 residues of the upstream genomic sequence of Sec61 upstream of the NAT selection marker cassette (amplified by PCR using BY4741 as a template, a forward primer: 5′- gaaagagctcCTATATATATGTATGCGCAAATAATTCCT-3′, and a reverse primer: 5′- gaatactagtCAATCTTCGCCTTCAAATTC-3′, upper case for yeast genome-specific sequences and lower case for SacI and SpeI restriction sites respectively). Pore mutations (M90L/T185I/M294I/M450L) were introduced to Sec61 by site-specific mutagenesis. The resulting plasmid was then linearized by cutting the plasmid backbone with PciI. The DNA fragment was introduced into ySI7 by a standard lithium acetate/poly(ethylene glycol) transformation protocol. Recombinants were selected on a YPD agar plates. Supplemented with 100 µg/ml NAT. Incorporation of the mutations was verified by PCR and Sanger sequencing of single colonies.

To generate the yeast strain with Sec63 β-tether deletion, a yeast CEN-ARS plasmid (with a Leu marker) containing Sec63 fused on its N-terminus to Sbh1p with a 15xGS linker and on its C terminus to TEV cleavable GFP as in the wild type ySI7 strain (under the Sec63 own endogenous promoter: 187 bases upstream of Sec63 coding sequence, and terminator: 93 bases downstream of Sec63 coding sequence). The β-tether was deleted using site directed mutagenesis. A version of these mutants without the Sbh1p fusion was used for spot test analysis and transformed into ySI7 (to form ySI25) or into ySI8a (to form ySI25a), and the full version into ySI8 to form ySI25b and be used for protein purification.

2.4.2 Protein purification

Yeast cells were grown in YPD medium (1% yeast extract, 2% peptone, and 2% glucose) in shaker flasks at 30 °C. Upon reaching an optical density (OD600) of ~3, cells were harvested by centrifugation at 4,600g for 10 min. Cell pellets were frozen in liquid nitrogen and stored in −80 °C until use. Cell lysis was performed by cryo-milling (SPEX SamplePrep) at liquid-nitrogen temperature. All subsequent steps were carried out at 4 °C. Pulverized cells were resuspended in buffer containing 50 mM Tris pH 7.5, 200 mM 3 NaCl, 1 mM EDTA, 10% glycerol, 2mM DTT, 5 µg/ml aprotinin, 5 µg/ml leupeptin, 1 µg/ml pepstatin A, and 1.2 mM PMSF. To solubilize membranes, 1% lauryl maltose neopentyl glycol (LMNG; Anatrace) and 0.2% cholesteryl hemisuccinate (CHS; Anatrace) were added to the cell lysate. After 1.5-h incubation, the lysate was then clarified by ultracentrifugation (Beckman Type 45 Ti rotor) at 125,000g for 1 h. The clarified lysate was incubated by gentle rotation with agarose beads conjugated with anti-GFP nanobody (Chromotek) for 2.5 h. The beads were then packed in a gravity column and washed with approximately 20 column volumes of buffer containing 50 mM Tris pH 7.5, 200mM NaCl, 1.0 mM EDTA, 2 mM DTT, 0.02% glycol-diosgenin (GDN; Anatrace), and 10% glycerol. The Sec complex was eluted by incubating the beads with ~10 µg/mL TEV protease (approximately 1:15 weight ratio to the Sec complex) for ~14 h. The eluate was concentrated using an AmiconUltra centrifugal filter (100-kDa cut-off; Millipore) and injected into a Superose 6 Increase column (GE Lifesciences) equilibrated with 20 mM

Tris pH 7.5, 100 mM NaCl, 1mM EDTA, 2 mM DTT, and 0.02% GDN. Peak fractions were pooled and concentrated to ~5 mg/mL. The sample was immediately used for cryo-EM grid preparation (Fig 2.8).

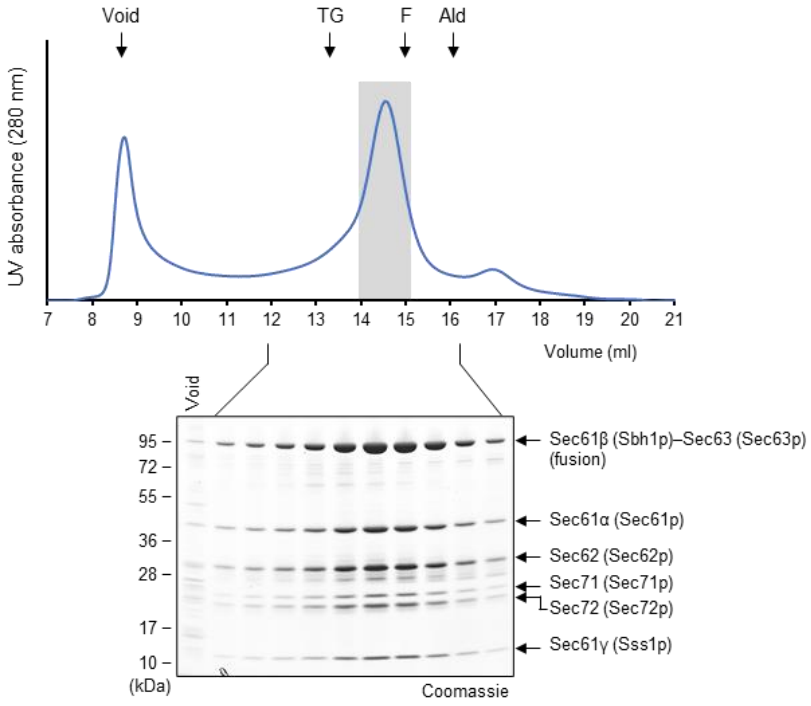

.

Figure 2.8 Purification of the Sec complex. Size-exclusion chromatography of the affinity-purified Sec complex. Upper panel, UV absorbance profile of the eluate. Arrowheads indicate the positions of the void peak and molecular weight standards: TG, thyroglobulin (670 kDa); F, ferritin (440 kDa); Ald, aldolase (158 kDa). Lower panel, Coomassie-stained SDS-PAGE gel of the indicated fractions.

Purification of the PM Sec61 mutant followed the same purification steps. To purify the PM Sec61 and βΔ6 Sec63 double mutant, the cells were initially grown in a leucine drop-out synthetic complete (SC(−Leu)) agar medium until OD600 of ~1.2 before harvest. The purification steps that follow are equivalent to those described for the wild-type complex.

2.4.3 Cryo-EM analysis

Right before grid freezing, 3 mM fluorinated Fos-Choline-8 (FFC8; Anatrace) was added to the purified Sec complex. Gold Quantifoil R 1.2/1.3 holey carbon grid (Quantifoil) was glow-discharged for 20 s in Ar/O2 (75%:25%) using a Gatan Solarus plasma cleaner or in air using a PELCO easiGlow glow discharge cleaner. 3 µL of the sample were applied to a glow-discharged grid. After incubating at 4 °C and 100% humidity for 10 s, the grid was blotted with Whatman No. 1 filter papers for 3 s and plunge-frozen in liquid-nitrogen-cooled liquid ethane using Vitrobot Mark IV (FEI).

The data sets were collected on an FEI Talos Arctica electron microscope operated at an acceleration voltage of 200 kV (Table 2.1). Dose-fractionated images (movies) were recorded on a Gatan K2 Summit direct electron detector operated in the super-resolution mode (with a physical pixel size of 1.16 Å) using SerialEM software (50). The total

exposure was 8 s at a frame rate of 0.2 s/frame and a dose rate of 1.25 e− per Å2 per frame. Target defocus values were from −0.8 μm to −2.4 μm.

A summary of the single-particle analysis procedure is shown in Figs. 2.9-2.10. First, the movies were subjected to whole-frame-only motion correction using MotionCor2 (51). The corrected movies were then 2x frame-binned by averaging each two frames, resulting in a total of 20 frames per movie. All subsequent image processing was performed using cryoSPARC v2 (52). Defocus values were estimated on the summed micrographs using CTFFIND4 (53) implemented in cryoSPARC. Micrographs that were not suitable for image analysis (containing crystalline ice and displaying large motion drifts) were removed by manual inspection (resulting in 2,162 movies). After automatically picking particles (407,288 particles), the particles were polished by per-particle motion correction with the 2x frame-binned movies (358,961 particles; the remaining particles were rejected due to proximity to the micrograph edges). The particle images were extracted with a box size of 256 pixels. The particle images were then subjected to reference-free 2D classification. After removing empty detergent micelle particles, which constituted the majority of discarded particles, and low-quality particles, 208,049 particles were selected. These particles were used for generation of three initial models (ab-initio 4 reconstruction), followed by 3D classification (heterogeneous refinement). About 83% of the particles populated one class that reached 4.75-Å resolution and showed prominent features of the Sec complex. The particles from this class was further refined by non-uniform refinement of cryoSPARC, leading to the final map at 3.68-Å resolution (based on gold-standard Fourier shell correlation (FSC) of independently refined half maps and the 0.143 cut-off criterion; Fig. 2.9E). Local resolution estimation was also performed in cryoSPARC (Fig. 2.9F). The map shown in Figures is a combined map, which was sharpened (B-factor of −104.7 Å2) and lowpass-filtered at 3.68 Å, except for the density map for Sec62, the J-domain, and the detergent micelle (Fig. 2.1A), which were lowpass-filtered according to local resolution values.

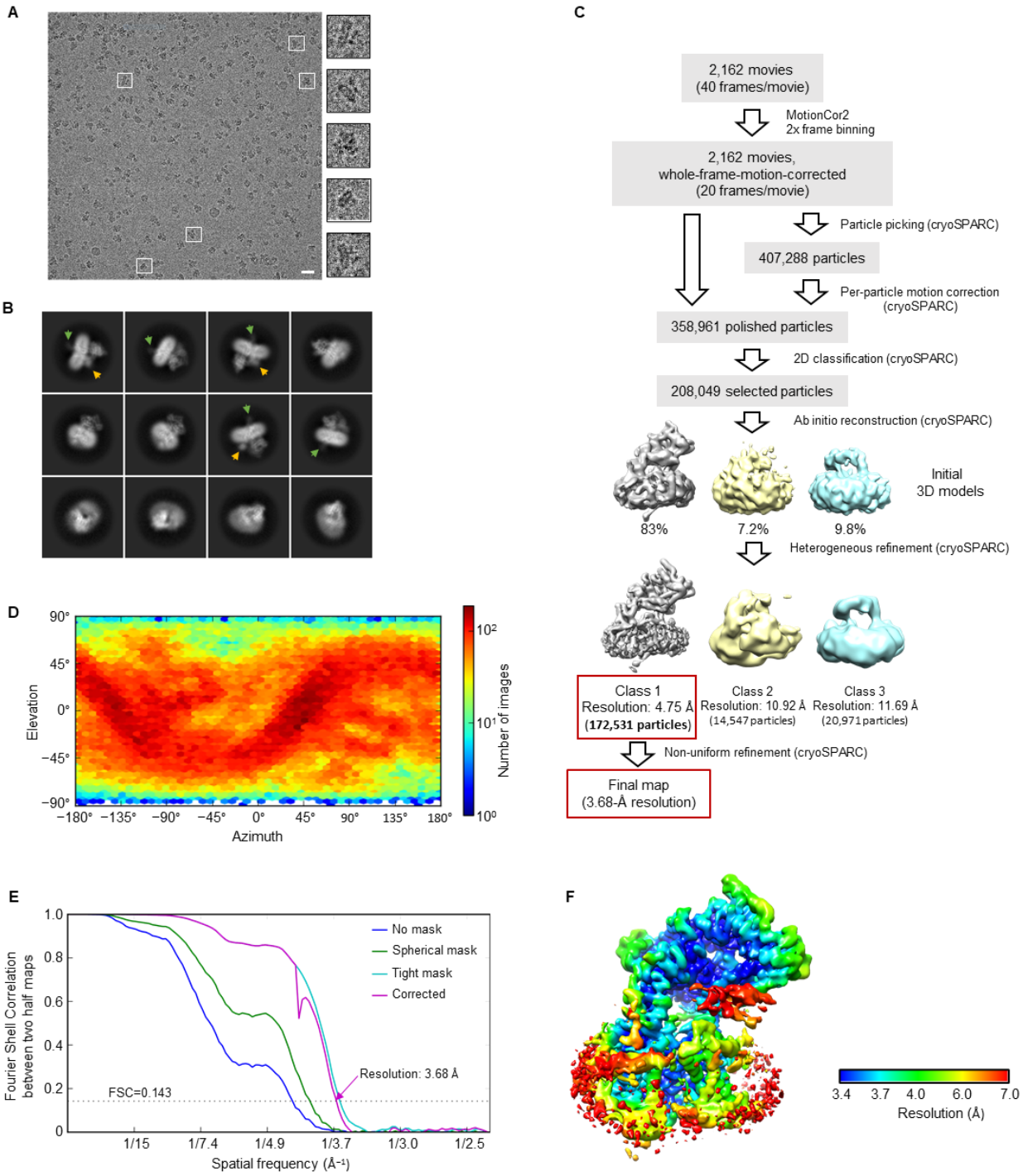

Figure 2.9 cryo-EM single-particle analysis of the Sec complex. A. A representative cryo-EM micrograph. Magnified images of particles outlined with white squares are shown in the right panels. Scale bar, 20 nm. **B**. Selected 2D class averages of particles (box width, 297 Å). Green and orange arrowheads indicate flexible J-domain of Sec63 and cytosolic domain of Sec62. **C**. Summary of single-particle image analysis procedure. **D**. Distribution of particle orientations. **E**. Fourier Shell Correlation (FSC) between the two half maps of the final 3D reconstruction. **F**. Local resolution map. The shown map is unsharpened, unfiltered map.

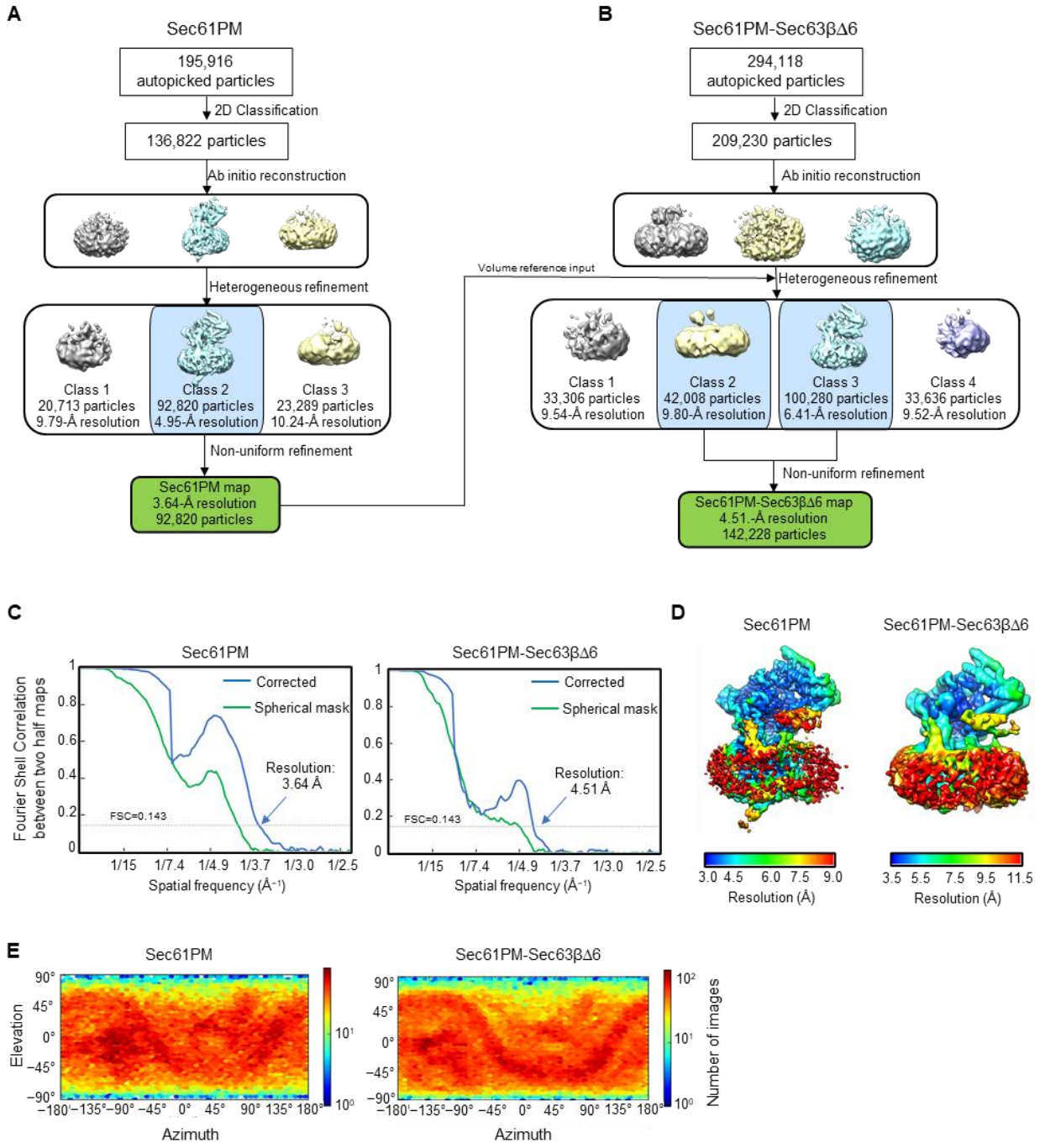

Figure 2.10 Cryo-EM image processing workflow and quality analysis of Sec61 PM mutant and Sec61 PM and Sec63 β-tether deletion double mutant.A-B. CryoEM image processing workflow for Sec complex with Sec61 pore mutant (PM) (A) and Sec complex with Sec61 PM and Sec63 β-tether deletion (B). **C**. Fourier Shell Correlation (FSC) between two half maps of final 3D reconstruction for Sec61PM (left) or Sec61PM-Sec63βΔ6 (right). **D**. Local resolution distribution, for Sec complex with Sec61PM (left) and Sec61PM-Sec63βΔ6 (right). **E**. Particle orientation distribution of maps derived from Sec complexes with Sec61PM (left) and Sec61PM-Sec63βΔ6 (right).

2.4.4 Atomic model building and model refinement

The atomic model was built using Coot (54) and the sharpened, lowpass-filtered combined map. The models for Sec61 and Sec63 were built de novo, except for some parts of Sec61α (TM2 and TM7) where prior structural information from the *Methanocaldococcus jannaschii* (PDB ID: 1RH5) and *Pyrococcus furiosus* (PDB ID: 3MP7) SecY channel structures were used. An initial model for Sec71-72 was generated by the SWISS-MODEL homology modeling webserver using the *Chaetomium thermophilum* Sec71-72 crystal structure (PDB ID: 5L0W) as a template, and the model was rebuilt in Coot.

Model refinement was done in real space using Phenix 1.14 (55) and the combined map. (Table 2.1). To prevent overfitting, the weight of 2 was used such that when refinement was performed with one of two half maps, the FSC curves between the refined model and either half map (FSCwork and FSCfree, respectively) do not significantly separate. We also slightly blurred (by a B-factor of 30 Å2) the lowpass-filtered map prior to model refinement to minimize the fitting into high-frequency noises. The refinement resolution limit was set to 3.7 Å. MolProbity (56) and EMRinger (57) were used for structural validation (Table 2.1). The following amino acid segments were not modeled because they were either invisible or insufficiently resolved in the density map: N–9, 57–72 (plug), 143–146, 311–359, and 469–480(C) of Sec61α (Sec61p); N-50 of Sec61β (Sbh1p); N–25 of Sec61γ (Sss1p); 37–53, 79–92, 116–201 (J-domain), 551-556 and 613–663(C) of Sec63 (Sec63p); N–68 of Sec71 (Sec66p); and all of Sec62. Protein electrostatics were calculated using the Adaptive Poisson-Boltzmann Solver (www.poissonboltmann.org) (58) with default parameters. UCSF Chimera (59) and PyMOL (Schrödinger) were used to prepare Figures in the paper amorphous.

Chapter Three

Stepwise gating of the Sec61 protein-conducting channel by Sec63 and Sec62

Portions of this work were published as:

Itskanov S, Kuo KM, Gumbart JC, Park E. Stepwise gating of the Sec61 protein-conducting channel by Sec63 and Sec62. *Nat Struct Mol Biol*. 2021 Feb;28(2):162-172.

3.1 Introduction

Many proteins are transported into the endoplasmic reticulum by the universally conserved Sec61 channel. Post-translational transport requires two additional proteins, Sec62 and Sec63, but their functions are poorly defined. In the present study, we determined cryo-electron microscopy (cryo-EM) structures of several variants of Sec61–Sec62–Sec63 complexes from *Saccharomyces cerevisiae* and *Thermomyces lanuginosus* and show that Sec62 and Sec63 induce opening of the Sec61 channel. Without Sec62, the translocation pore of Sec61 remains closed by the plug domain, rendering the channel inactive. We further show that the lateral gate of Sec61 must first be partially opened by interactions between Sec61 and Sec63 in cytosolic and luminal domains, a simultaneous disruption of which completely closes the channel. The structures and molecular dynamics simulations suggest that Sec62 may also prevent lipids from invading the channel through the open lateral gate. Our study shows how Sec63 and Sec62 work together in a hierarchical manner to activate Sec61 for post-translational protein translocation.

3.2 Results

3.2.1 Cryo-EM analysis of two fungal Sec complexes

To determine how the gates are regulated in the Sec complex, we first analyzed a large cryo-EM dataset of the wildtype (WT) Sec complex from S. cerevisiae (*Sc*Sec), which yielded three structures at 3.1–3.2-Å resolutions with distinct conformations (Fig. 3.1A-B, Table 3.1, and Fig. 3.11). While reconstruction from approximately 1 million particles yielded a 3.0-Å-resolution consensus map (Fig. 3.11B,H), we found that the particle set contained subpopulations lacking Sec62 or Sec71-Sec72, despite apparent sample homogeneity (Fig. 3.9A). We therefore performed additional three-dimensional (3D) classifications to separate particles with and without Sec62 (referred to as Sec62+ and Sec62−) (Fig. 3.11A). Furthermore, the Sec62+ class could be further separated into two distinct subclasses (referred to as C1 and C2), which show notable conformational differences in Sec62, the lateral gate, and the plug (Fig 3.1B and Fig. 3.2E; see below). Although an atomic model for Sec62 could not be built due to insufficient local resolution, the classification significantly improved Sec62 features, enabling unambiguous assignment of individual domains (Fig. 3.1D).

To gain insights into structural and mechanistic conservation across species, we also determined structures of the Sec complex from the thermophilic fungus *Thermomyces lanuginosus* (*Tl*Sec) at overall resolution of 3.6 to 3.9 Å (Fig. 3.1C, Table

3.1, and Fig. 3.20). *Tl*Sec classes with and without Sec62 closely resemble the *Sc*Sec [C2] and [Sec62−] structures, respectively (brackets denote classes). We could not isolate a C1-equivalent class from the *Tl*Sec dataset perhaps because the specimen freezing condition (4°C) might have biased the conformation distribution of this thermophilic complex towards C2. The structure of *Tl*Sec[Sec62−] is essentially identical to a separately determined structure of a mutant complex completely lacking Sec62 (ΔSec62 *Tl*Sec) (Fig. 3.13G and Fig. 3.21). Importantly, the domain arrangement of *Tl*Sec62 is the same as that of *Sc*Sec62 despite ~30% overall sequence identity (Fig. 3.1C and Fig. 3.3). Compared to *Sc*Sec62, *Tl*Sec62 is better resolved such that we could register amino acids to its TM1.

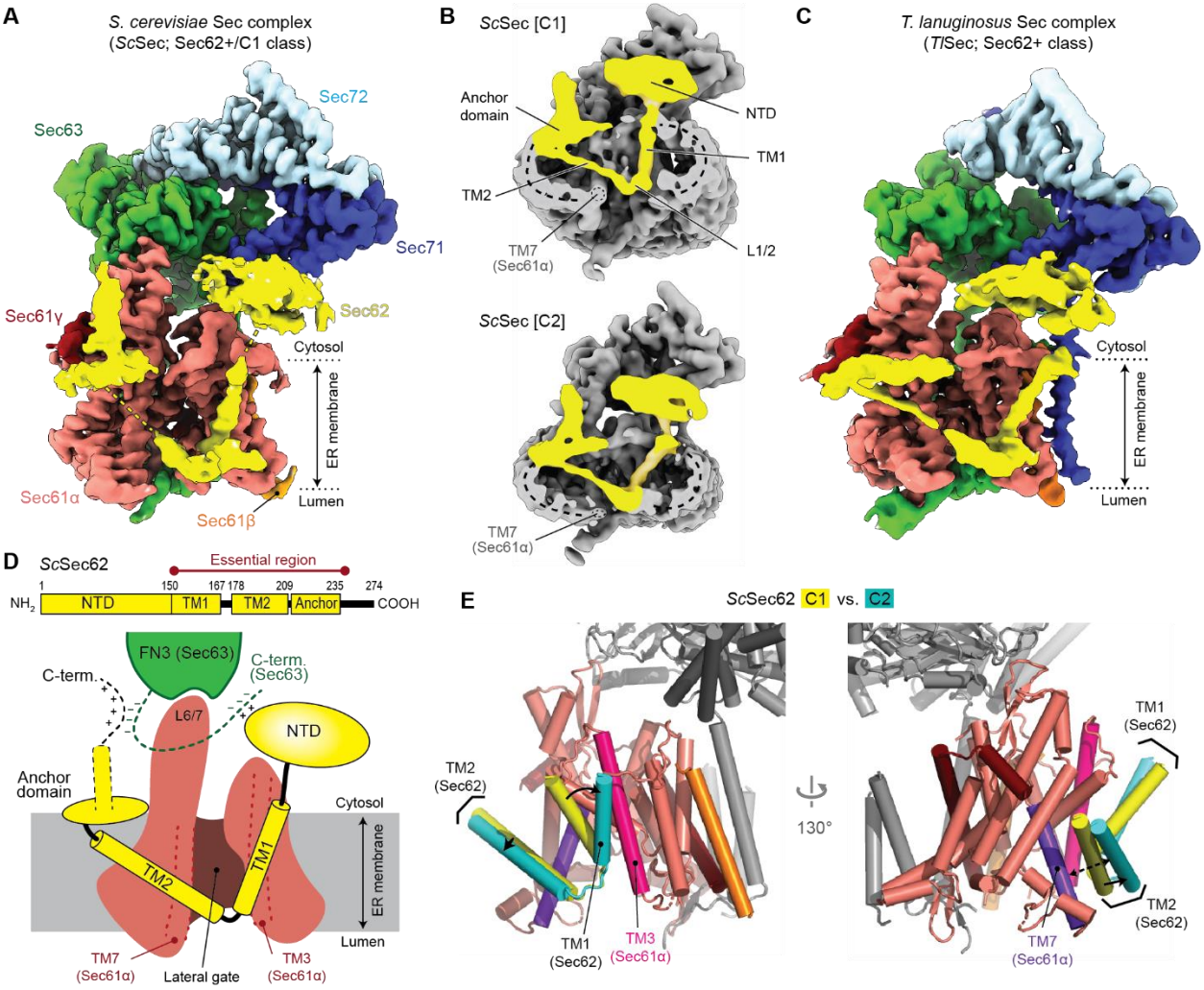

Figure 3 1 Cryo-EM analysis of fungal Sec complexes and the structure of Sec62. A. The 3.1-Å-resolution cryo-EM reconstruction of the yeast Sec complex (front view into the lateral gate). Yellow dash lines indicate the connections that are visible at a lower contour level (see panel B). In yeast nomenclature, the α, β, and γ subunits of the Sec61 complex are called as Sec61p, Sbh1p, and Sss1p, respectively. **B**. Cutaway views showing Sec62 (yellow). Shown are 6-Å-lowpass-filtered C1 (upper panel; a tilted view from the ER lumen) and C2 (lower panel; front view) maps. Dashed line, detergent micelle. **C**. The 3.8-Å-resolution reconstruction of the *T. lanuginosus* Sec complex (the consensus Sec62+ map). **D**. Domain organization of Sec62. Previous studies suggest an interaction between the NTD of Sec62 and the C-terminal tail of Sec63 (43,60). In addition, based on the proximity, the C-terminal tails of Sec62 and Sec63 may also interact with each other through an electrostatic interaction. **E**. Interactions between the Sec62 TMs and

lateral gate. Dashed arrow, a gap between Sec61α TM7 and Sec62 TM2 in the C2 conformation. The color scheme for Sec61 is the same as in a. Sec63, Sec71, and Sec72 are in grey.

Table 3.1. Cryo-EM data collection, refinement and validation statistics of wildtype *Sc*Sec

	*Sc*Sec [Sec62−] (EMD-22770, PDB 7KAH)	*Sc*Sec[C1] (EMD-22771, PDB 7KAI)	*Sc*Sec[C2] (EMD-22772, PDB 7KAJ)
Data collection and processing			
Magnification	64,000x	64,000x	64,000x
Voltage (kV)	300	300	300
Electron exposure (e^{-}/Å^2)	49.1	49.1	49.1
Defocus range (μm)	-0.8 to -2.5	-0.8 to -2.5	-0.8 to -2.5
Pixel size (Å)	1.19	1.19	1.19
Symmetry imposed	*C*1	*C*1	*C*1
Initial particle images (no.)	2,686,839	2,686,839	2,686,839
Final particle images (no.)	391,885	193,263	193,661
Map resolution (Å)	3.1	3.2	3.1
FSC threshold	0.143	0.143	0.143
Map resolution range (Å)	2.6 – 11	2.8 – 12	2.7 – 12
Refinement			
Initial model used	PDB 6N3Q	PDB 7KAH	PDB 7KAH
Model resolution (Å)	3.2	3.3	3.3
FSC threshold	0.5	0.5	0.5
Map sharpening *B* factor (Å^2)	86.6	80.8	75.9
Model composition			
Non-hydrogen atoms	10,495	10,718	10,712
Protein residues	1,349	1,399	1,399
Ligands	-	-	-
B factors (Å^2)			
Protein	73	61	58
Ligand	-	-	-
R.m.s. deviations			
Bond lengths (Å)	0.003	0.003	0.003
Bond angles (°)	0.522	0.508	0.513
Validation			
MolProbity score	1.43	1.42	1.33
Clashscore	4.61	4.14	3.87
Poor rotamers (%)	0	0	0
Ramachandran plot			
Favored (%)	96.83	96.58	97.01
Allowed (%)	3.17	3.42	2.99
Disallowed (%)	0	0	0

Table 3.2. Cryo-EM data collection, refinement and validation statistics of wildtype and mutant *Tt*Sec complexes

	*Tt*Sec [Sec62−] (EMD-22773, PDB 7KAK)	*Tt*Sec [Plug-open] (EMD-22774, PDB 7KAL)	*Tt*Sec [Plug-closed] (EMD-22775, PDB 7KAM)	ΔSec62 *Tt*Sec (EMD-22776, PDB 7KAN)	Δanchor *Tt*Sec (EMD-22777)
Data collection and processing					
Magnification	36,000x	36,000x	36,000x	36,000x	64,000x
Voltage (kV)	200	200	200	200	300
Electron exposure (e^{-}/Å^2)	50.0	50.0	50.0	50.0	49.1
Defocus range (μm)	-0.6 to -2.4	-0.6 to -2.4	-0.6 to -2.4	-0.9 to -2.2	-0.7 to -2.9
Pixel size (Å)	1.14	1.14	1.14	1.14	1.19
Symmetry imposed	*C*1	*C*1	*C*1	*C*1	*C*1
Initial particle images (no.)	1,632,659	1,632,659	1,632,659	546,712	229,825
Final particle images (no.)	155,601	114,704	143,227	222,047	76,726
Map resolution (Å)	3.9	4.0	3.8	3.7	4.4
FSC threshold	0.143	0.143	0.143	0.143	0.143
Map resolution range (Å)	3.4 – 13	3.3 – 13	3.3 – 12	3.3 – 12	3.7 – 14
Refinement					
Initial model used	PDB 7KAN	PDB 7KAN	PDB 7KAN	PDB 6N3Q	-
Model resolution (Å)	4.1	4.2	4.0	4.0	-
FSC threshold	0.5	0.5	0.5	0.5	-
Map sharpening *B* factor (Å^2)	110.3	90.7	105.2	127.8	-
Model composition					
Non-hydrogen atoms	10,438	10,794	10,921	10,661	-
Protein residues	1,371	1,429	1,445	1,371	-
Ligands	-	-	-	2	-
B factors (Å^2)					
Protein	117	126	74	30	-
Ligand	-	-	-	34	-
R.m.s. deviations					
Bond lengths (Å)	0.002	0.002	0.003	0.003	-
Bond angles (°)	0.524	0.489	0.521	0.623	-
Validation					
MolProbity score	1.51	1.42	1.48	1.55	-
Clashscore	6.33	5.62	5.60	6.18	-
Poor rotamers (%)	0	0	0	0	-
Ramachandran plot					
Favored (%)	97.09	97.42	96.96	96.72	-
Allowed (%)	2.91	2.58	3.04	3.28	-
Disallowed (%)	0	0	0	0	-

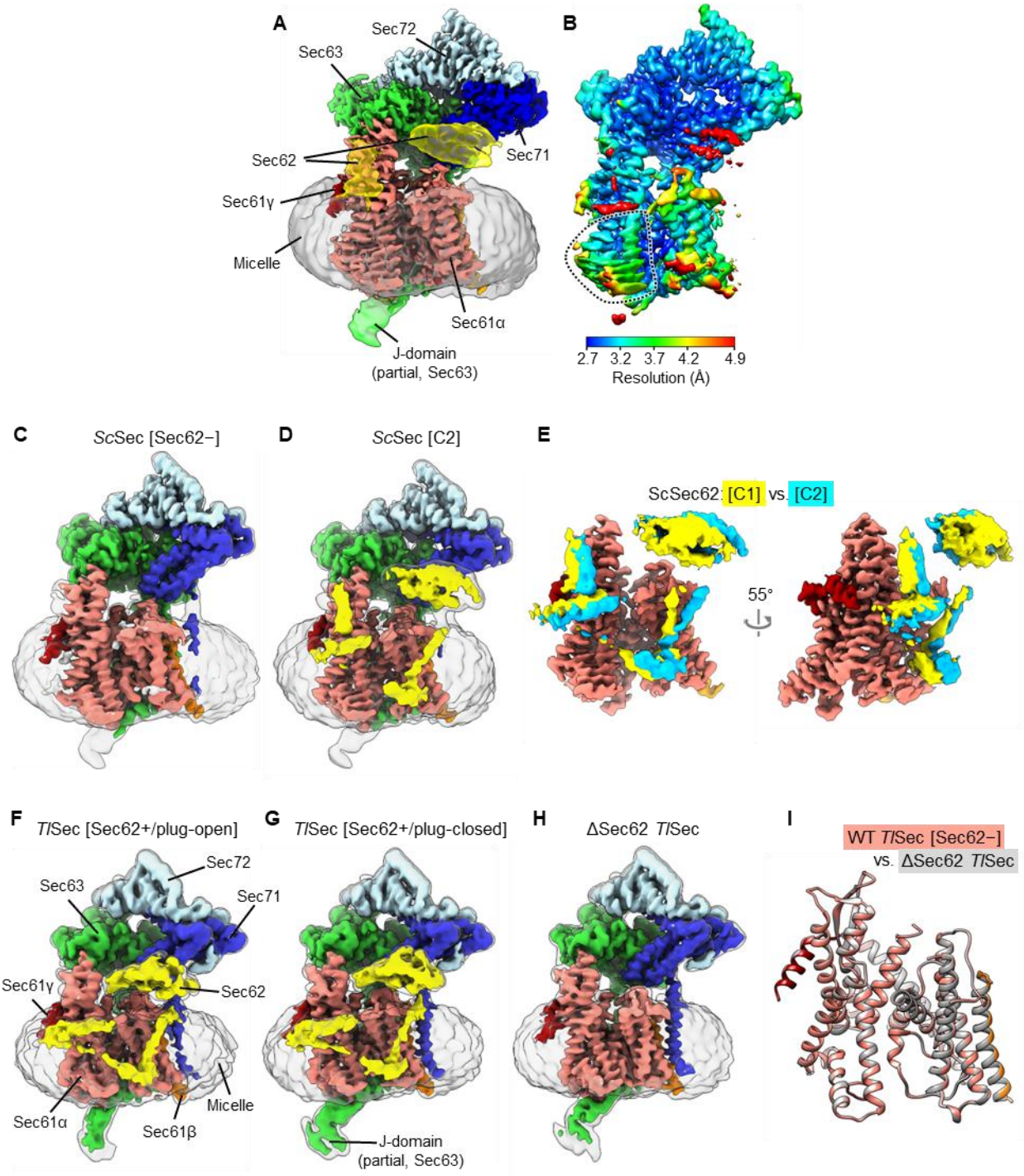

Figure 3.2 Conformational and compositional variability of Sec complex in the *S. cerevisiae* and *T. lanuginosus*. **A**. The 3.0-Å-resolution consensus map of *Sc*Sec. Salmon, Sec61α; orange, Sec61β; red, Sec61γ; yellow, Sec62; green, Sec63; blue, Sec71; light blue, Sec72; Grey, detergent micelle. Semitransparent surface, lowpass-filtered (5 Å for Sec62 and the J-domain and 7 Å for the micelle) maps shown at a lower contour level. **B.** As in A, but showing a local resolution map. Note that in addition to Sec62, the TM7-TM8 region of Sec61α (dotted line) displays noticeably lower solution than the overall resolution due to conformational heterogeneity (see Fig. 3.4A). **C**. As in A, but with the 3.1-Å-resolution map of the Sec62− class. Semitransparent surface, 6-Å-lowpass-filtered map at a lower contour level. **D**. As in A, but with the 3.1-Å-resolution map of the Sec62+/C2 class. **E**. The Sec62 densities of the C1 (yellow) and C2 (cyan) classes were compared after aligning the two cryo-EM maps. For simplicity, only Sec61 (from the C1 class) and Sec62 are shown. **F**. he 4.0-Å-resolution map of the Sec62+/plug-open class of WT *Tl*Sec. The

color scheme is the same as in Fig. 1. Semitransparent surface, a 7-Å-lowpass-filtered map shown at a lower contour level. **G**. As in F, but showing the 3.8-Å-resolution map of the Sec62+/plug-closed class. **H**. As in F, but with the 3.7-Å-resolution map of ΔSec62 *Tl*Sec complex. **I**. The atomic models of the Sec61 complexes from the Sec62− class of WT *Tl*Sec (in color) and the ΔSec62 *Tl*Sec structure (in grey) were aligned and compared (RMSD of Cα atoms is 0.24Å).

3.2.2 Sec62 forms a V-shaped Structure

Sec62 consists of a cytosolic, globular N-terminal domain (NTD), two TMs (TM1 and TM2) connected by a short ER luminal loop (L1/2), and a cytosolic C-terminal segment (Fig. 3.1D). Functionally essential regions have previously been mapped to the two TMs and a segment of ~30 amino acids immediately following TM2 (43). The TMs of Sec62 are arranged as a V shape in front of the lateral gate with L1/2 directed to the lateral gate opening (Fig. 3.1A-D). The contact with the channel is mainly formed by an interaction of Sec62-TM1 with the TM3 and N-terminal segment of Sec61α.

Following TM2, Sec62 contains an oval-shaped structure lying flat on the membrane interface (Fig. 3.1A-D). This amphipathic structure, which we termed the anchor domain, is most likely formed by an ~20-residue-long conserved segment within the abovementioned 30 amino acids, and is rich in hydrophobic amino acids (Fig. 3.3). While single-point mutations of these hydrophobic residues caused no growth defect, alanine substitutions of three consecutive residues in positions 215–220 were lethal (Fig. 3.3D), suggesting that decreased hydrophobicity interrupts its functionally essential interaction with the membrane. The structure of a *Tl*Sec mutant (Δanchor *Tl*Sec) with the anchor domain replaced with a glycine/serine linker showed virtually no visible Sec62 features (Fig. 3.3E), suggesting Sec62 becomes too mobile without the domain. Taken together, these observations suggest that the function of the anchor domain is to properly position the V-shaped TMs of Sec62 at the lateral gate.

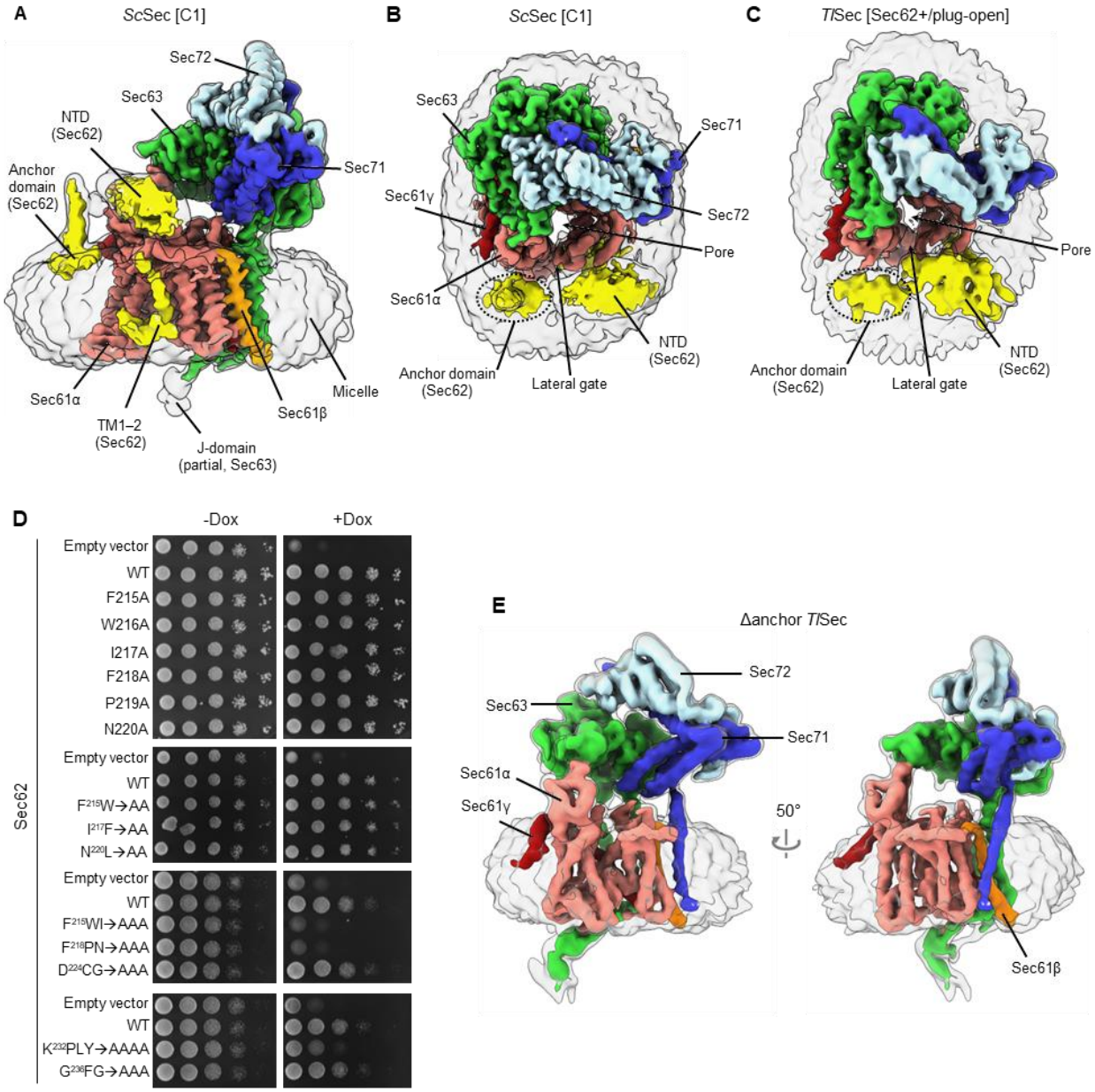

Figure 3.3 Structure and mutagenesis analysis of the anchor domain of Sec62. A. As in Fig. 3.1A, but a side view additionally showing a 6-Å-lowpass-filtered map at a lower contour level (semitransparent surface). **B**. As in a, but showing a view from cytosol. The anchor domain of Sec62 is indicated by a dotted oval. **C**. As in b, but showing the map of the Sec62+/plug-open class of *Tl*Sec. Semitransparent surface is a 7-Å-lowpass-filtered map. **D**. Yeast growth complementation tests for Sec62 anchor mutants. The yeast strain (ySI62) whose endogenous Sec62 is expressed under a tetracycline-repressible promoter was transformed with a CEN/ARS plasmid expressing WT or indicated mutant Sec62 under its native promoter. As a control, empty vector was used. In the right panels, 10 μg/mL doxycycline was included to repress the expression of endogenous Sec62. All growth assays were performed at 30 °C. The top two panels (single and double mutants) were grown on synthetic complete (SC) medium lacking leucine, and the bottom two panels (triple and quadruple Ala mutants) were grown on YPD medium. **E**. As in A, but showing the 4.4-Å-resolution map of Δanchor *Tl*Sec. Semitransparent surface, 7-Å-lowpass-filtered map at a lower contour level. We note that the conformation of Δanchor *Tl*Sec is essentially identical to ΔSec62 *Tl*Sec.

The revealed position and topology of Sec62 raise an important question about how the channel would engage with substrate polypeptides. During the initial stage of post-translational translocation, a substrate polypeptide is expected to insert into the channel as a loop with both its N- and C- termini exposed to the cytosol (61). While the N-terminal signal sequence may sit initially at the lateral gate as seen in structures of mammalian co-translational and bacterial post-translational complexes (8,11,13), later it must engage with the signal peptidase for cleavage (62). However, the presence of Sec62 would pose a problem because L1/2 of Sec62 would block the release of the signal sequence from the lateral gate. The answer may be provided by a conformational transition from C1 to C2 as visualized in the *Sc*Sec structure (Fig. 3.1E). While in both structures the seam between the Sec62-TM1 and Sec61α-TM3 is tight, a sufficient gap is formed on the other side of the lateral gate between the Sec62-TM2 and Sec61α-TM7 in the *Sc*Sec[C2] structure. A similar gap also exists in the *Tl*Sec structures. Thus, the signal sequence of the substrate likely exits through the gap transiently formed between Sec62-TM2 and Sec61α-TM7 during translocation.

3.2.3 Sec62 regulates the gates of Sec61

Three distinct classes of *Sc*Sec (i.e., C1, C2, and Sec62−) showed notable conformational differences in the lateral gate (Fig. 3.4A). Although open in all three structures, the extent of the lateral gate opening varies on the ER luminal side, with C1 most open and Sec62− least open. The C2 structure, in which Sec62-TM2 is disengaged, is open to an intermediate degree. The movement is mainly mediated by a rigid-body rotation of the TM7, TM8, and the intervening loop (L7/8) of Sec61α (Fig. 3.4A), which seems to be induced by the interaction between L1/2 of Sec62 and the lateral gate (Fig. 3.1A-D). Thus, this movement is distinct from the hinge-like motion between the two halves (TM1–5 and TM6–10) of Sec61α which mediates opening of the channel from the fully closed state (2,63–65).

Importantly, the motion of TM7–8 of Sec61α appears to control the position of the plug (Fig. 3.4B-E). In *Sc*Sec[Sec62−], the plug is clearly visible immediately below the pore constriction (‘plug-closed’ conformation; Fig. 3.4B,D, Fig 3.5C). By contrast, in *Sc*Sec[C1], the plug is displaced to a position near the C-terminus of Sec61γ (‘plug-open’ conformation; Fig. 3.4C,E), thus opening the pore. In *Sc*Sec[C2], the plug seems disordered, probably because it takes intermediate positions between the two conformations. Similar observations were also made with the *Tl*Sec structures: compared to the Sec62− and ΔSec62 structures, the Sec62+ structure shows a shifted position of Sec61α TM7–8 as in *Sc*Sec[C2] (Fig 3.5) and concomitant plug mobilization, where 53% and 42% particles classified into the plug- closed and open conformations, respectively (Figs. 3.20 and Fig3.5D-E). The plug displacement is likely caused by the Sec62-induced movement of Sec61α TM7 since the plug interacts with TM7 and L7/8 in the plug-closed conformation (63).

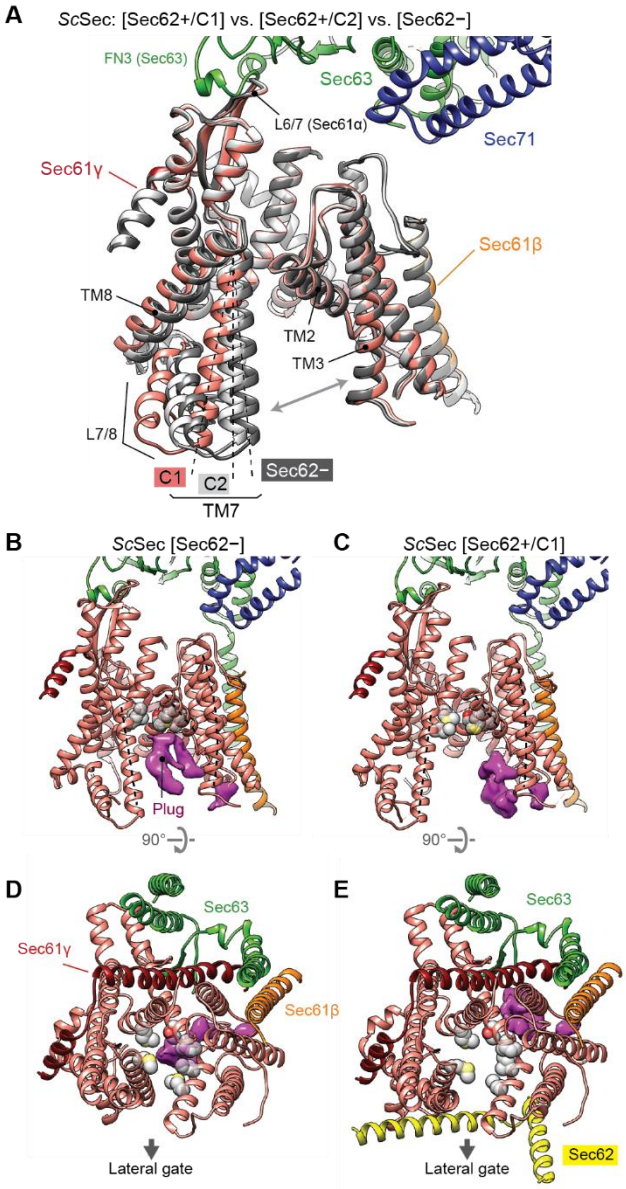

Figure 3.4 Regulation of the lateral and vertical gates by Sec62. A. A comparison of the Sec61 channel conformation between the three *Sc*Sec classes, C1 (in color), C2 (light grey) and Sec62− (dark grey). Dashed lines, TM7 of Sec61α. Grey arrows, the lateral gate. Sec62 is not shown. **B**–**E**, A comparison of the plug domain (purple density) between Sec62-lacking and -containing *Sc*Sec classes. Grey spheres, pore ring residues. Dashed lines, lateral gate helices (left to right: TM7, TM2, and TM3 of Sec61α). Shown are front views (B and C) and cytosolic views (D and E).

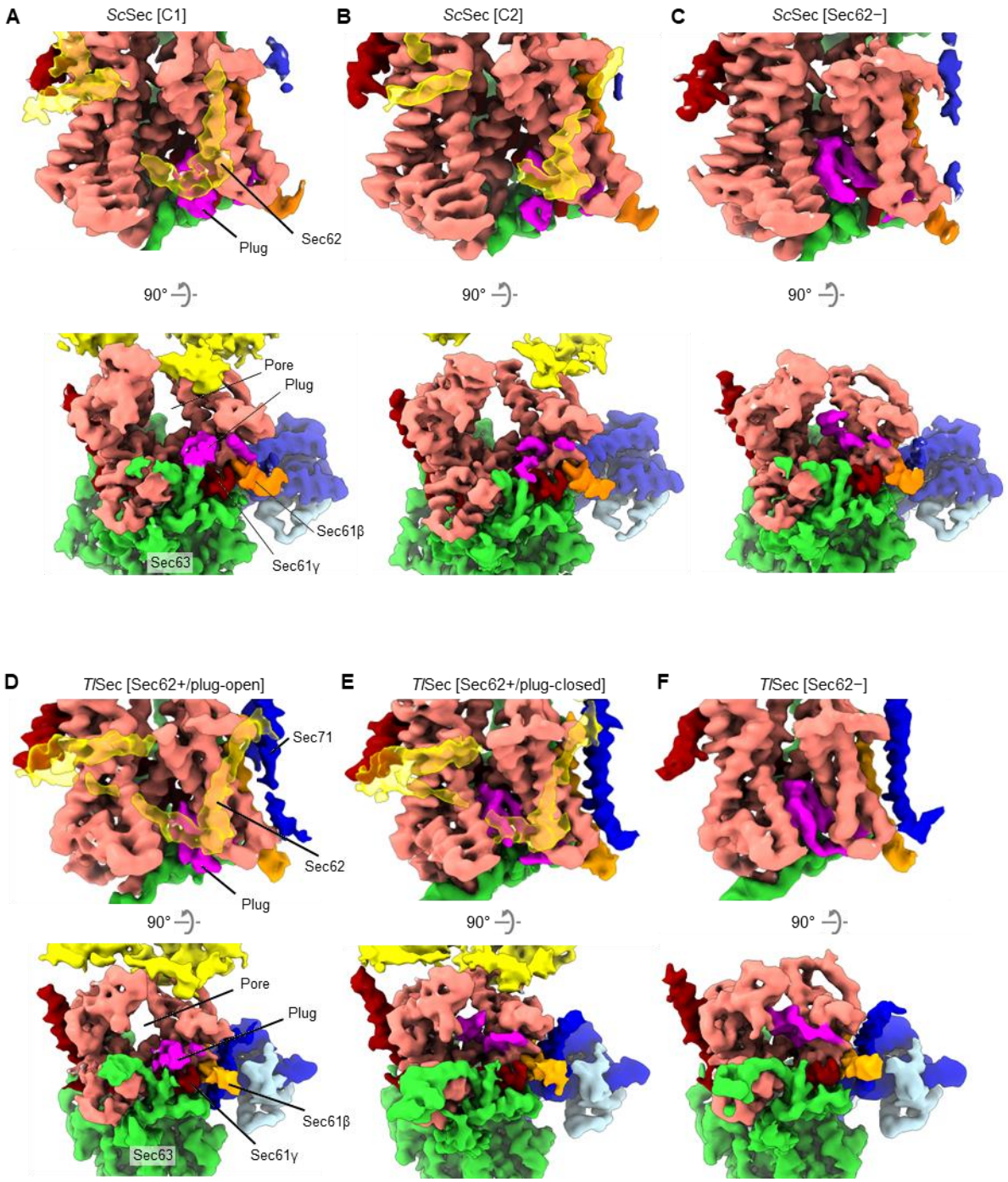

Figure 3. 5 The presence of Sec62 induces opening of the vertical gate of Sec61 by displacing the plug domain from the closed position.A-C. Views into the lateral gate (front view, top panel; bottom, view from ER lumen) of the three classes of the WT *Sc*Sec structure, C1, C2, and Sec62−. Color scheme: salmon, Sec61α; orange, Sec61β; red, Sec61γ; yellow, Sec62; green, Sec63; blue, Sec71; light blue, Sec72; magenta, the plug domain. **D**–**F**, As in A-C but with the WT *Tl*Sec structures. Shown are front views (upper panels) and views from the ER lumen (lower panels). We note that in both the plug-open and plug-closed classes, the conformation of Sec62 (yellow) is similar to that of the *Sc*Sec[C2] structure.

3.2.4 Partially open Sec61 is inactive

Despite the observed channel gating by Sec62, physiological importance of this role remained unclear. Without Sec62, the lateral gate can still be opened by Sec63. Even though the pore is blocked by the plug, it has been proposed that insertion of a substrate polypeptide would push the plug away (66). To investigate importance of the Sec62-dependent gating, we sought for mutations affecting Sec61 gating as ΔSec62 does, but independently of Sec62. If the gating function of Sec62 is essential, such mutations would be expected to compromise cell viability.

We first chose to mutate the fibronectin III (FN3) domain of Sec63, which interacts with the cytosolic loop 6/7 (L6/7) of Sec61α (Fig. 3.6A). L6/7 also provides a major interaction site for the ribosome in cotranslational translocation and the SecA ATPase in bacterial post-translational translocation and thus has been universally implicated in priming or activating the channel (10,12,23,40,41). We found that none of the FN3 mutants had a growth defect at 30°C (Fig. 3.6B, left). Only a mild defect was seen at 37°C even with the most severe mutant (FN3mut) (Fig. 3.7B). To understand this unexpectedly weak phenotype, we determined the structure of FN3mut *Sc*Sec (Fig. 3.6D,E, Table 3.2, Fig 3.17). The structure showed that the FN3 domain was indeed disengaged from L6/7 by the mutation, causing ~10° rotation of Sec61 along the membrane normal (Fig. 3.7E-F). Nonetheless, the lateral gate was still open (Fig. 3.6D). Importantly, the FN3mut complex still exhibited Sec62-induced TM7 movement and plug mobilization (Fig. 3.6D,E), which may explain the near-WT growth phenotype of the mutant.

Next, we mutated the pore of Sec61α. In closed SecY structures (2,10,12,67), the aliphatic amino acids lining the pore constriction (called the pore ring residues) make a hydrophobic interaction with the plug. Compared to other species, the pore ring of *Sc*Sec61α appears significantly less hydrophobic (68). Thus, we reasoned that a mutant with a more hydrophobic pore ring (M90L/T185I/M294I/M450L; collectively denoted PM) might bias the plug towards the closed conformation. In growth complementation assays, PM itself did not affect cell growth, but strikingly, strong synthetic growth impairment was observed when combined with FN3mut (Fig. 3.6B, right). Importantly, a plug deletion41 (ΔPlug) could rescue growth, suggesting that the growth inhibition originates from a gating defect (Fig. 3.6C). Consistent with this idea, the structures of the combined mutant (FN3mut/PM) showed a strong density of the plug in the closed conformation and no Sec62-dependent movement of lateral gate helices (Fig. 3.6F,G, and Fig. 3.7G), thereby closely resembling the gating state of *Sc*Sec[Sec62−] despite the presence of Sec62 in front of the lateral gate. On the other hand, PM alone still showed Sec62-mediated movements in the lateral gate and plug, similar to WT (Fig. 3.7H-I). Taken together, these results show that the channel conformation seen in the absence of Sec62 is inactive for post-translational translocation.

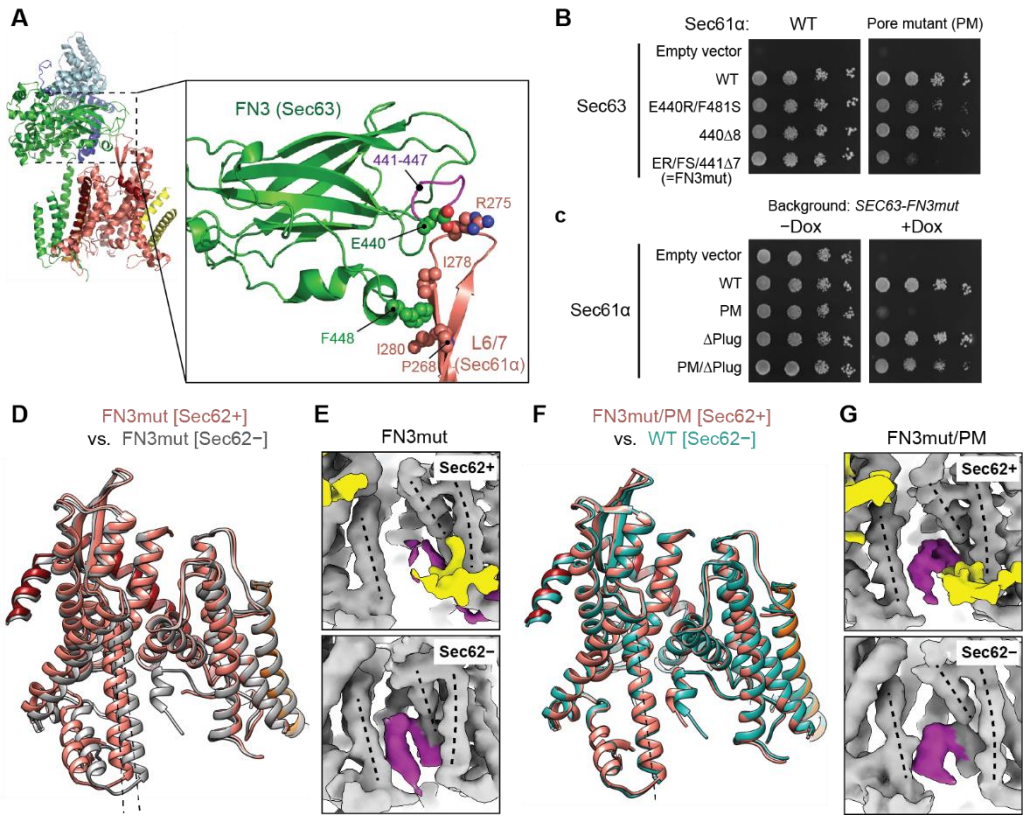

Figure 3.6 Structural and functional analysis of a gating-defective mutant complex. A. The interaction between the FN3 domain of Sec63 and the L6/7 loop of Sec61α. Amino acids involved in the interactions are indicated. **B**. Yeast growth complementation experiments (at 30°C) testing functionality of indicated FN3 mutants of Sec63 in the background of wild-type (left) or pore-mutant Sec61α (right). FN3mut refers to a combination of E440R (ER) and F481S (FS) mutations and a deletion of seven amino acids 441–447 (441Δ7). To repress chromosomal WT Sec63 expression (under a tetracycline promoter), doxycycline was added. Fig. 3.7A. **C**. As in B, but testing for indicated Sec61α mutants in the background of Sec63-FN3mut as a sole Sec63 copy. The addition of doxycycline (Dox) represses chromosomal WT Sec61α expression. **D**. As in Fig. 3.4A, but with the FN3mut *Sc*Sec structures with and without Sec62. **E**. A comparison of the plug domain (purple density) between the FN3mut *Sc*Sec structures with and without Sec62 (yellow). Dashed lines, lateral gate helices (left to right: TM7, TM2, and TM3 of Sec61α). **F**. As in D but comparing the Sec62-containing FN3mut/PM structure and the Sec62− class of WT *Sc*Sec. **G.** As in E, but with the FN3mut/PM *Sc*Sec structures.

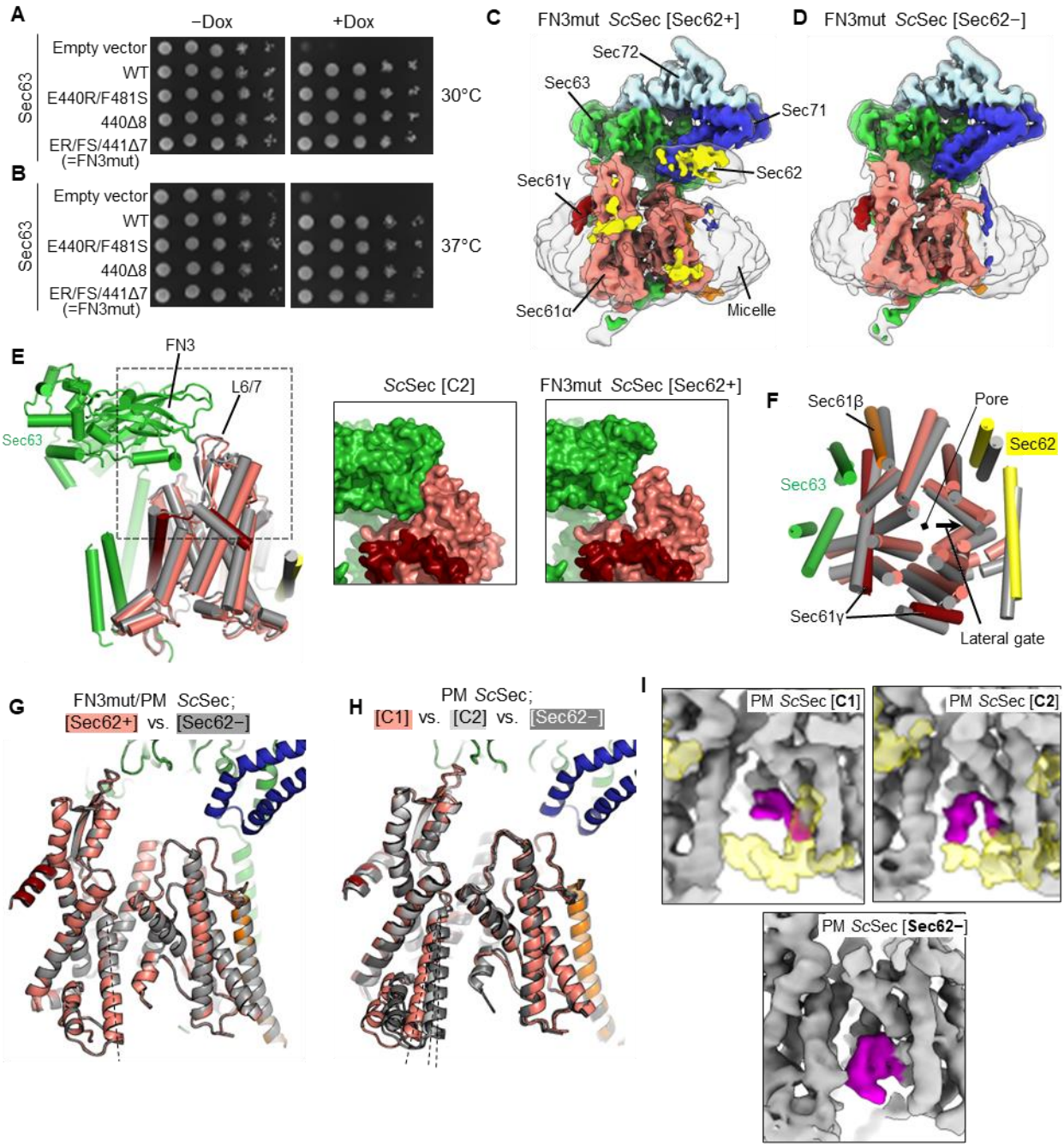

Figure 3.7 Structures of the *Sc*Sec complex containing mutations in the FN3 domain of Sec62 and the pore ring of Sec61α. A. The same yeast growth complementation experiment shown in Fig. 3.6B (left panel), but additionally showing a control without doxycycline. The experiments were repeated three times with similar results. **B**. As in a, but the plates were incubated at 37 °C. **C**. The 3.9-Å-resolution cryo-EM map of the Sec62+ class of the FN3mut *Sc*Sec complex. **D**. As in C, but with the 4.0-Å-resolution cryo-EM map of the Sec62− class of the FN3mut *Sc*Sec complex. **E**. The interaction between the FN3 domain of Sec63 and the L6/7 of Sec61α. Left, a side view showing Sec63 (green) and the Sec61 complex (grey, C2 class of WT *Sc*Sec; color, Sec62+ class of FN3mut *Sc*Sec). The structures were aligned with respect to Sec63. The area indicated by a grey dashed box is shown in the middle and right panels with a solvent-accessible surface representation. **F**. As in the left panel of E, but showing the cytosolic view into the Sec61 complex. **G**. As in Fig. 2a, but comparing the Sec62+ and Sec62− classes of FN3mut/PM *Sc*Sec. **H**. As in Fig. 3.4A, but comparing the three classes of PM *Sc*Sec. **I**. As in Fig. 3.6E, but with PM *Sc*Sec. We note that although

the plug domain is partly visible in the C1 and C2 classes of PM *Sc*Sec, its density is substantially weaker than that of the Sec62− class.

Table 3.3. Cryo-EM data collection, refinement and validation statistics of mutant *Sc*Sec complexes

	PM *Sc*Sec [Sec62−] (EMD-22778, PDB 7KAO)	PM *Sc*Sec [C1] (EMD-22779, PDB 7KAP)	PM *Sc*Sec [C2] (EMD-22780, PDB 7KAQ)
Data collection and processing			
Magnification	64,000x	64,000x	64,000x
Voltage (kV)	300	300	300
Electron exposure (e^{-}/Å^2)	48.8	48.8	48.8
Defocus range (μm)	-1.0 to -2.7	-1.0 to -2.7	-1.0 to -2.7
Pixel size (Å)	1.15	1.15	1.15
Symmetry imposed	*C*1	*C*1	*C*1
Initial particle images (no.)	195,915	195,915	195,915
Final particle images (no.)	35,573	17,341	16,679
Map resolution (Å)	4.0	4.1	4.0
FSC threshold	0.143	0.143	0.143
Map resolution range (Å)	3.5 - 14	3.5 - 17	3.5 - 16
Refinement			
Initial model used	PDB 7KAH	PDB 7KAI	PDB 7KAJ
Model resolution (Å)	4.2	4.2	4.2
FSC threshold	0.5	0.5	0.5
Map sharpening *B* factor (Å^2)	50.9	39.3	32.9
Model composition			
Non-hydrogen atoms	10,502	10,715	10,753
Protein residues	1,349	1,398	1,402
Ligands	-	-	-
B factors (Å^2)			
Protein	152	178	187
Ligand	-	-	-
R.m.s. deviations			
Bond lengths (Å)	0.003	0.003	0.002
Bond angles (°)	0.520	0.519	0.494
Validation			
MolProbity score	1.48	1.49	1.46
Clashscore	7.65	7.87	7.39
Poor rotamers (%)	0	0	0
Ramachandran plot			
Favored (%)	97.74	97.74	97.75
Allowed (%)	2.26	2.26	2.25
Disallowed (%)	0	0	0

Table 3.4. Cryo-EM data collection, refinement and validation statistics of mutant *Sc*Sec complexes

	FN3mut *Sc*Sec [Sec62−] (EMD-22781, PDB 7KAR)	FN3mut *Sc*Sec [Sec62+] (EMD-22782, PDB 7KAS)	PM/FN3mut *Sc*Sec [Sec62−] (EMD-22783, PDB 7KAT)	PM/FN3mut *Sc*Sec [Sec62+] (EMD-22784, PDB 7KAU)	FN3mut/ Δ210-216 *Sc*Sec (EMD-22787, PDB 7KB5)
Data collection and processing					
Magnification	64,000x	64,000x	64,000x	64,000x	45,000x
Voltage (kV)	300	300	300	300	200
Electron exposure (e^{-}/Å^2)	49.1	49.1	~48–49	~48–49	63
Defocus range (μm)	-0.8 to -2.7	-0.8 to -2.7	-1.1 to -2.2	-1.1 to -2.2	-0.7 to -2.0
Pixel size (Å)	1.19	1.19	1.19	1.19	0.9
Symmetry imposed	*C*1	*C*1	*C*1	*C*1	*C*1
Initial particle images (no.)	1,274,219	1,274,219	267,541	267,541	2,270,392
Final particle images (no.)	82,671	119,420	32,704	54,139	257,231
Map resolution (Å)	4.0	3.9	4.4	4.0	3.8
FSC threshold	0.143	0.143	0.143	0.143	0.143
Map resolution range (Å)	3.4 - 14	3.3 - 18	3.7 - 19	3.4 - 16	3.2 - 13
Refinement					
Initial model used	PDB 7KAH	PDB 7KAR	PDB 7KAH	PDB 7KAT	PDB 7KAH
Model resolution (Å)	4.2	4.1	4.5	4.2	4.0
FSC threshold	0.5	0.5	0.5	0.5	0.5
Map sharpening *B* factor (Å^2)	74.8	73.8	59.3	58.1	119.3
Model composition					
Non-hydrogen atoms	10,435	10,616	10,431	10,711	9,777
Protein residues	1,341	1,385	1,340	1,396	1,252
Ligands	-	-	-	-	-
B factors (Å^2)					
Protein	117	64	255	125	126
Ligand	-	-	-	-	-
R.m.s. deviations					
Bond lengths (Å)	0.003	0.004	0.002	0.003	0.004
Bond angles (°)	0.581	0.596	0.501	0.533	0.626
Validation					
MolProbity score	1.58	1.63	1.37	1.53	1.71
Clashscore	7.84	6.69	6.71	6.26	7.3
Poor rotamers (%)	0	0	0	0	0
Ramachandran plot					
Favored (%)	97.19	96.17	98.10	96.86	95.60
Allowed (%)	2.81	3.83	1.90	3.14	4.40
Disallowed (%)	0	0	0	0	0

3.2.5 Sec62 prevents invasion of lipids into channel

In addition to the role in channel gating, the ΔSec62 *Tl*Sec structure suggests another function of Sec62− preventing lipids from moving into the channel. In ΔSec62 *Tl*Sec, strong, well-ordered densities of lipid or detergent tails are visible at the lateral gate (Fig. 3.9A). The densities are vertically aligned along the hydrophobic groove of the open lateral gate (Fig. 3.9A and Fig. 3.8A). By contrast, in the Sec62+ structures, only weak fragmented densities were observed (Fig. 3.9B). In the cytosolic leaflet, a

lipid/detergent molecule seems to be accommodated with an outward rotation of the TM2–3 of Sec61α (Fig. 3.8B). Sec62 may inhibit lipids from entering the lateral gate by restricting this movement. In the ER luminal leaflet, the L1/2 of Sec62 seems to sterically block lipids from entering (Fig. 3.9B). We did not observe a strong lipid/detergent density in the lateral gate of *Sc*Sec[Sec62−], perhaps because of a lower affinity to lipid/detergent. However, one of the previous *Sc*Sec structures (66), the conformation of which resembles the ΔSec62 *Tl*Sec structure, has shown a lipid-like density at the lateral gate and movement of Sec61α TM2–3 similar to ΔSec62 *Tl*Sec (Fig. 3.8C-D). Collectively, these observations suggest that, in the absence zof Sec62, lipid molecules may penetrate the lateral gate that is opened by Sec63.

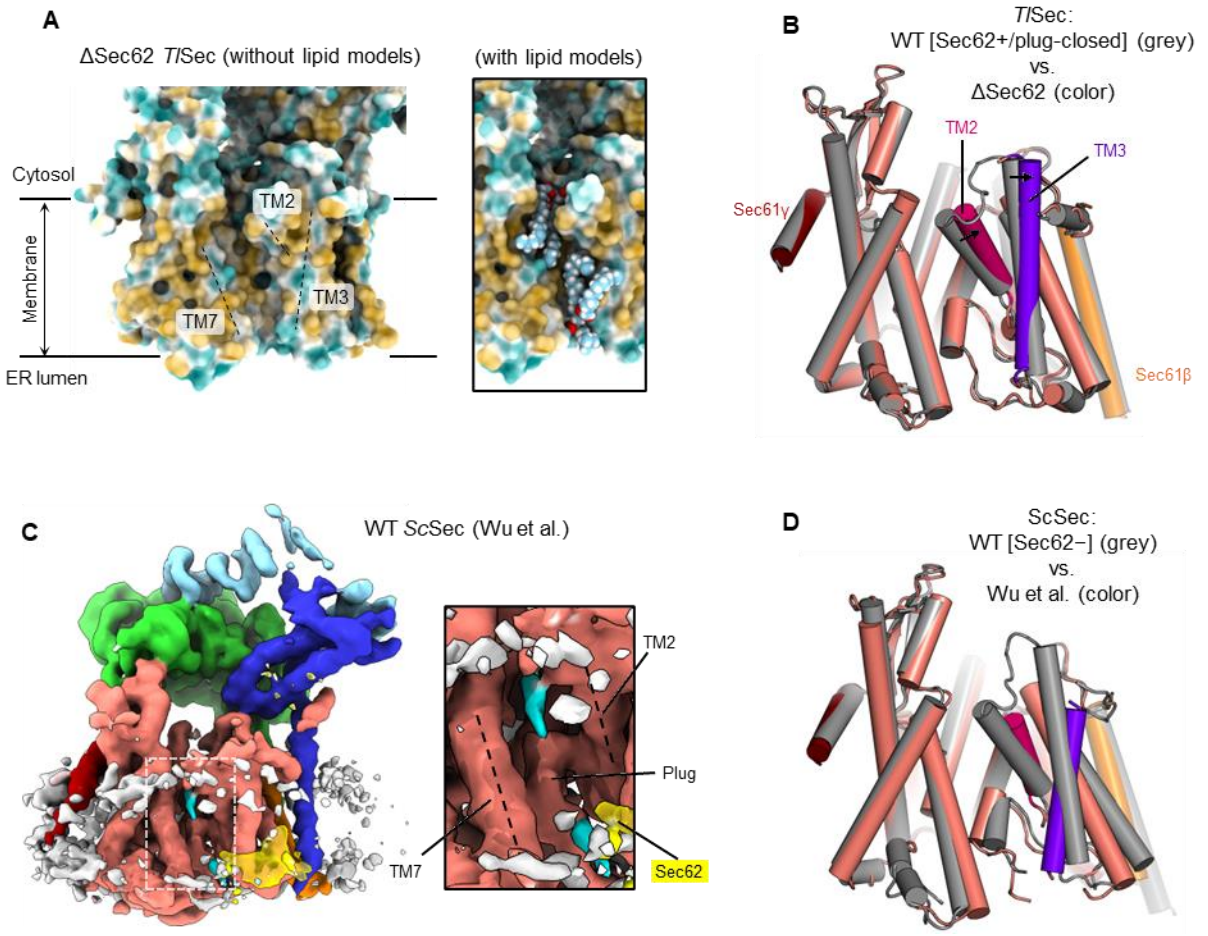

Figure 3.8 Lipid/detergent molecules at the lateral gate. A. A view into the lateral gate of the Sec61 channel in ΔSec62 *Tl*Sec. The left panel shows a surface representation of the complex (front view) showing the distribution of hydrophobic (yellow) and hydrophilic (cyan) amino acids. In the right panel, phosphatidylcholine lipid molecules modelled into the cryo-EM densities were additionally shown in a space-filling representation. **B.** A comparison of the Sec61 atomic models of ΔSec62 *Tl*Sec (in color) and WT *Tl*Sec [Sec62+/plug-closed] (in grey). Movements of TM2 (purple) and TM3 (violet) are indicated. **C**. As in Fig. 4a, but the WT *Sc*Sec structure by Wu et al. (EMDB-0440; ref. 29). Densities in cyan are detergent/lipid-like features. **D.** As in b, but comparing the structure by Wu et al. (in color; PDB 6ND1; ref. 29) and the *Sc*Sec[Sec62−] structure of the present study (in grey).

To further investigate a role of Sec62 in blocking lipid penetration, we performed 200-ns all-atom MD simulations (Fig. 3.9C-H). In simulations of the Sec62-containing

structures (that is, WT *Tl*Sec[Sec62+/plug-open] and WT *Sc*Sec[C1] and [C2]), the translocation pore largely remained unobstructed and devoid of lipids (Fig. 3.9C,F). Only one phospholipid molecule partially penetrated the lateral gate of *Sc*Sec in the cytosolic leaflet of the membrane, with its aliphatic tails remaining outside; further incursion is unlikely because the interior of the cytosolic half of the channel is highly polar42. Notably, no lipids penetrated the channel in the luminal leaflet during the entire duration of the simulations, despite a larger opening (~20 Å in *Tl*Sec and ~30 Å in *Sc*Sec) between TM3 and TM7 of Sec61α (Fig. 3.9F). As the plug is displaced in these structures, the luminal funnel of Sec61α remained completely unoccupied. By contrast, simulations of the Sec62-lacking structures (ΔSec62 *Tl*Sec and *Sc*Sec[Sec62−]) showed substantially deeper penetration of lipid molecules into the lateral gate (Fig. 3.9D,G). In both the cytosolic and luminal leaflets of the membrane, the lateral gate became occupied with lipids within ~80 ns. These results are consistent with the lipid/ detergent densities seen in the cryo-EM structure of ΔSec62 *Tl*Sec.

Our cryo-EM structures and MD simulations suggested that the V-shaped transmembrane domain of Sec62 effectively blocks lipids from entering the open lateral gate, particularly on the ER luminal leaflet. We thus hypothesized that, without Sec62, the pore may be invaded by lipids if both the lateral gate and the plug remain open. We tested this idea by running another set of MD simulations on *Tl*Sec[Sec62+] and *Sc*Sec[C1] but excluding the Sec62 subunit (Fig. 3.9E,H). The results indeed show that, in both *Tl*Sec and *Sc*Sec, lipids invaded the pore mainly from the luminal leaflet, substantially obstructing the translocation pathway. It is probable that lipid molecules occupying the pore would inhibit insertion of substrate polypeptides. Thus, Sec62 seems to play an important role in maintaining the functionality of Sec61 by keeping lipids away from the open channel.

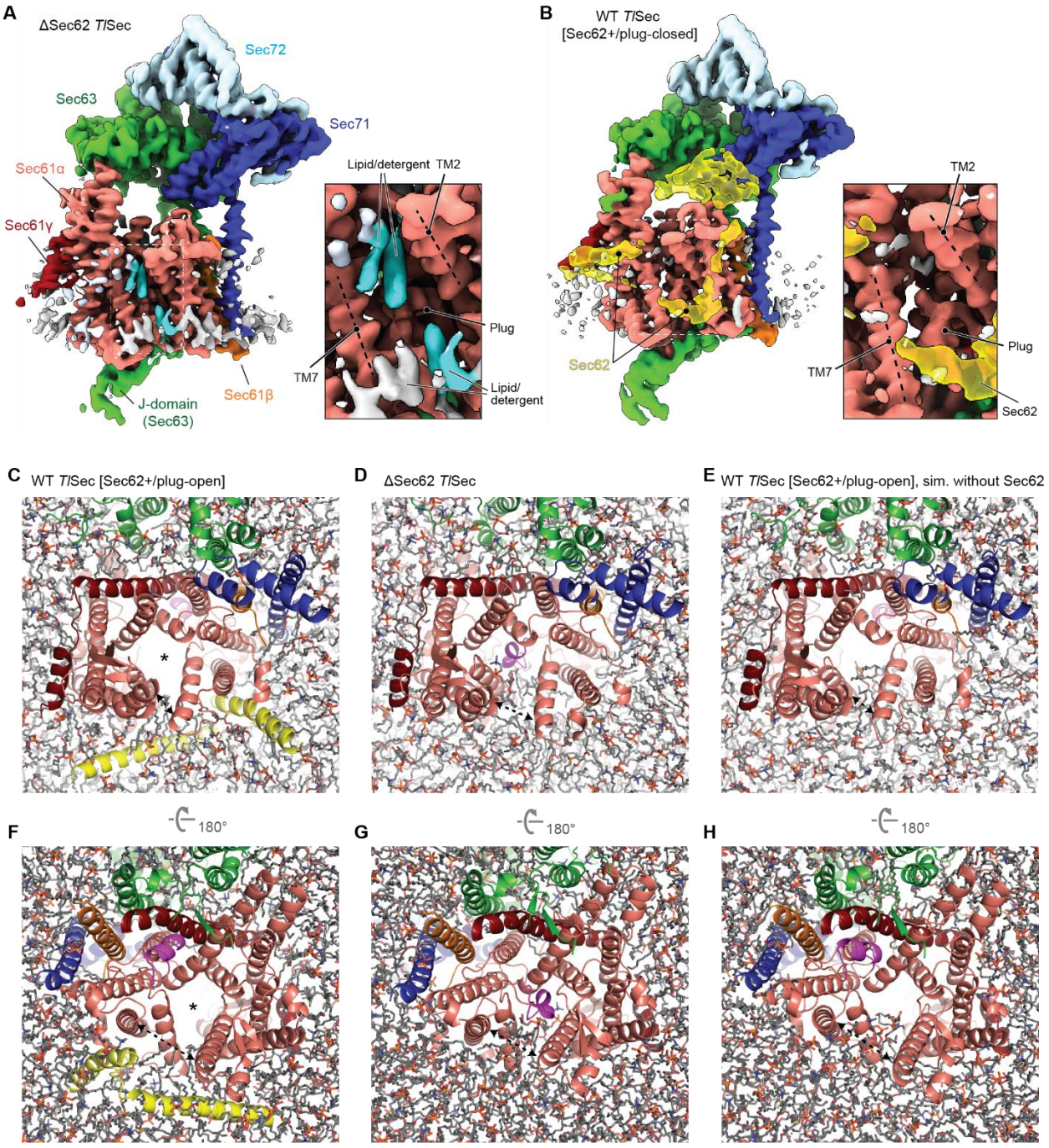

Figure 3.9 Sec62 prevents lipids from invading the Sec61 channel.A. Lipid/detergent molecules at the lateral gate in the *Tl*Sec structure lacking Sec62 (ΔSec62). The left panel is a front view. Non-protein densities are gray. Densities in cyan are lipid/detergent molecules intercalated at the lateral gate. The right panel is an enlarged view of the lateral gate (area indicated by the white dashed box in the left panel). **B**. As in a, but with the Sec62+/ plug-closed class of WT *Tl*Sec. We note that, similarly, the Sec62+/plug-open class does not show lipid/detergent densities at the lateral gate. **C**–**H**, All-atom MD simulations with indicated *Tl*Sec structures in a model membrane (C and F, WT *Tl*Sec[Sec62+/plug-open]; d and g, ΔSec62 *Tl*Sec; E and H, WT *Tl*Sec[Sec62+/plug-open] but without Sec62). The Sec complex is shown in ribbon representation in the same colors as in A and B. Lipids are shown in stick representation; C–E are views from the cytosol and F–H are views from the ER lumen. In C and F, the translocation pore is marked by an asterisk. The lateral gate openings are indicated by a dashed arrow. The frames are from 200 ns after the initiation of simulations.

3.2.6 Mechanism of Sec61 gating by Sec63

One unexpected finding was that the FN3-L6/7 interaction was dispensable for the protein translocation function of the Sec complex. This indicates that there must be another mechanism for Sec63 to open the lateral gate. Besides the FN3 domain, Sec63 forms major contacts with Sec61 through two other parts: TM3, which anchors Sec63 to the Sec61 complex, and a short ER luminal segment (residues 210–216) preceding TM3, which, together with the N-terminal segment of Sec63, interacts with a crevice on the back of the channel (opposite the lateral gate; Fig. 3.10A). We reasoned that the latter interaction might control lateral gating through a lever-like mechanism. In the WT background, replacement of this segment with a glycine/serine linker (Δ210–216) alone did not cause growth inhibition (Fig. 3.10B). However, when combined with FN3mut, cells did not grow (Fig. 3.10B).

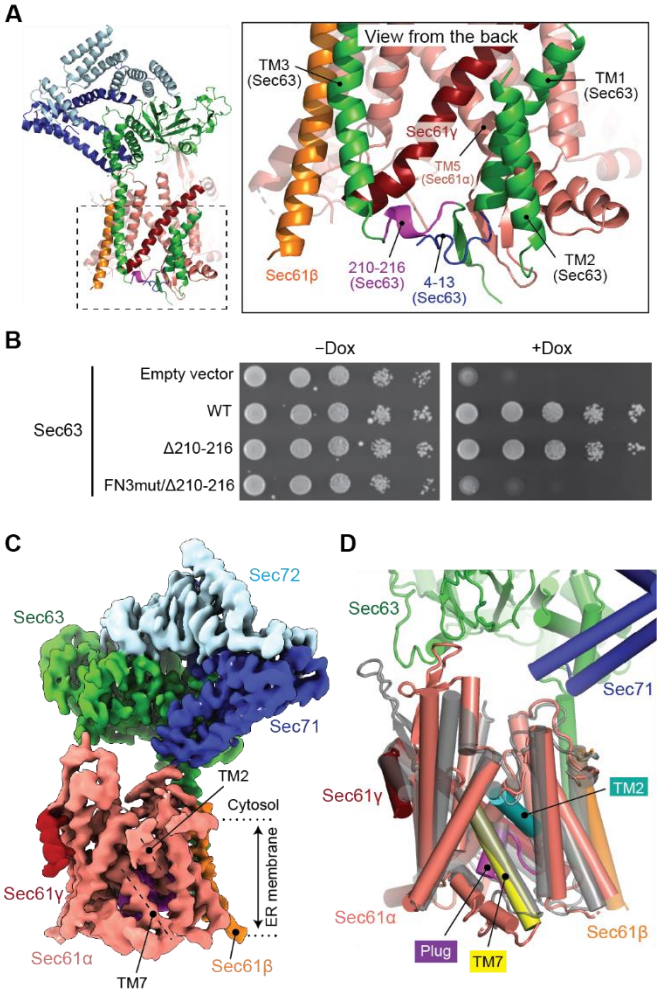

Figure 3.10 The structure of a fully closed Sec complex. A. The interaction between Sec61 and Sec63 in the ER lumen (view from the back). The N-terminal segment (positions 4–13) and the segment preceding TM3 (positions 210–216) of Sec63 are in blue and purple, respectively. The *Sc*Sec[C1] structure is shown. **B**. Yeast growth complementation (at 30 °C) testing the functionality of the indicated Sec63 mutants. The addition of Dox represses chromosomal WT Sec63 expression. The experiments were repeated twice with similar results. **C**. The 3.8-Å-resolution cryo-EM structure of the *Sc*Sec complex containing FN3mut/Δ210–216 double-mutant Sec63. The lateral gate helices

TM2 and TM7 are indicated. **D**. As in C, but showing the atomic model of the Sec61 complex. For comparison, the closed Methanocaldococcus jannaschii SecY structure (PDB 1RH5; semitransparent gray) is superimposed

To understand the structural basis of this synthetic defect, we determined the structure of the FN3mut/Δ210–216 *Sc*Sec complex (Fig. 3.10C and Fig. 3.19) The structure showed that, indeed, both the lateral and the vertical gates of the Sec61 channel are completely closed, resembling the idle archaeal SecY channel structure (2) (Fig. 3.10C). This demonstrates that Sec63 uses both its cytosolic and luminal domains to open the lateral gate in a two-pronged mechanism. The C-terminal cytosolic domain of Sec63 (following TM3) and Sec71–Sec72 are still attached to Sec61 through TM3 (Fig. 3.11). However, most of the parts preceding TM3 were invisible due to increased flexibility. Importantly, Sec62 was no longer visible either, despite copurification with the complex (Fig. 3.10C and Fig. 3.13E). Sec62 is probably associated with Sec63 through an electrostatic interaction with the C-terminal tail of Sec63 (69,70) (Fig. 3.1D), but it seems to no longer bind to the lateral gate due to structural incompatibility with the closed gate. Therefore, the lateral gate must be first opened by Sec63 before Sec62 can activate the channel for protein translocation.

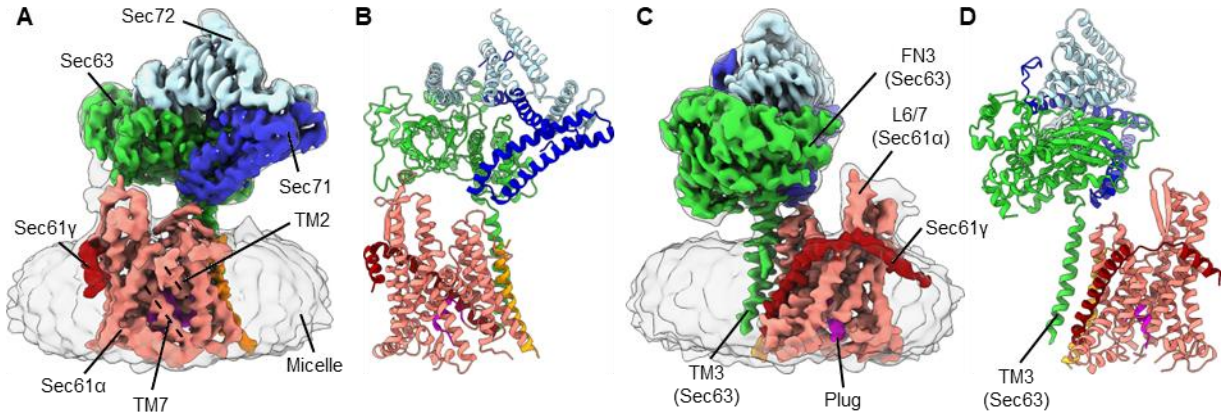

Figure 3. 11 Structure of a fully closed ScSec complex containing FN3mut/Δ210-216 Sec63. A–**D**, The cryo-EM map (A and C) and atomic model (B and D). The color scheme is the same as in Fig. 3.1 A,D. The plug domain is shown in magenta. Shown are front (A and B) and side (C and D) views.

3.3 Discussion and conclusion

In summary, our study defines the functions of Sec62 and reveals the mechanism by which Sec63 and Sec62 regulate the gates of the Sec61 channel. The function of Sec62 had been elusive for three decades since its discovery as an essential component in eukaryotic post-translational translocation (19,20,71). Our study shows that, once the lateral gate of the Sec61 channel is opened by Sec63, Sec62 fully activates the channel by further mobilizing the plug domain (Fig. 3.12). At the same time, Sec62 seems to prevent lipids from penetrating the channel interior through the open lateral gate by forming a barrier in front of the lateral gate. Such lipid penetration into the lateral gate and translocation pore would probably impair the protein translocation activity by competitively inhibiting insertion of polypeptide substrates into the channel. The lipids may also affect movements of polypeptides in later stages of protein translocation. The V-shaped

structure formed by the transmembrane domain of Sec62 is rather dynamic with respect to the rest of the complex and loosely associated with the lateral gate, as suggested by its relatively low-resolution densities in our cryo-EM maps. This flexibility may be important for insertion of signal sequences into and its egress from the lateral gate. It is also possible that the movement of Sec62 is modulated by binding of signal sequences and other protein translocation factors (for example, BiP) to the Sec61 channel.

The fully open conformation of the WT Sec complexes observed in our cryo-EM structures probably represents a resting state before substrate engagement. Although the channel's conformation and its dynamics in the native membrane environment remain to be determined, we speculate that this open state is probably a predominant form in the native ER membrane, based on the stable association of Sec61, Sec62 and Sec63. A pre-opened Sec61 channel in the post-translational complex contrasts with a relatively closed Sec61 channel seen with resting co-translational complexes, where the lateral gate is only marginally open, and the plug domain remains in the closed position (12). It has been generally thought that, during initial substrate engagement, the Sec61 channel would be opened by a hydrophobic interaction between the signal sequence (or TM helix) and the lateral gate (12–14,72,73). Our mutagenesis analysis, however, indicates that such a partially open state, similar to the one induced by Sec63 alone, is insufficient for post-translational protein translocation. This is probably because the plug domain in the closed position would impose too high an energy barrier for post-translational polypeptide substrates to insert into the pore.

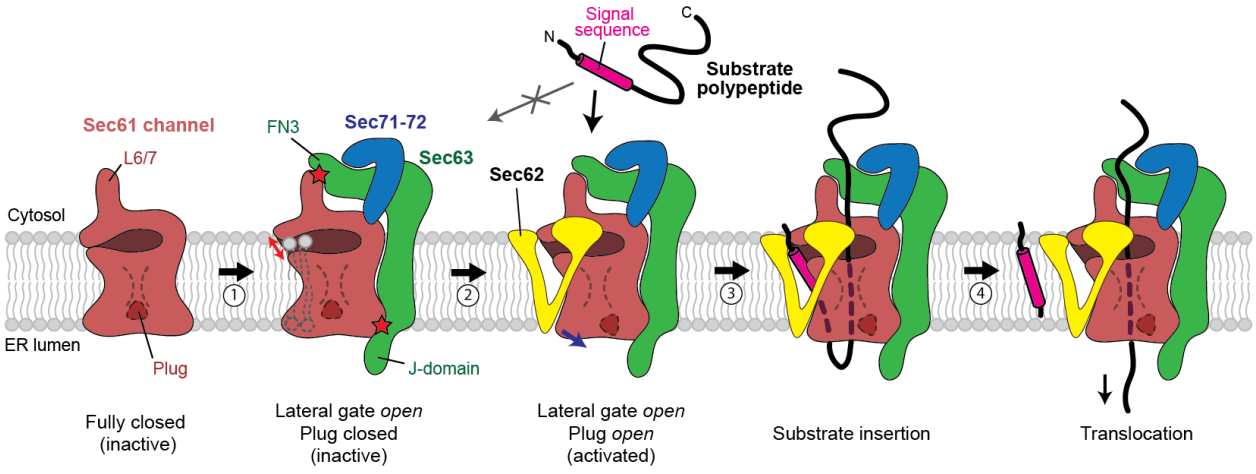

Figure 3.12 A model for the activation of the Sec61 channel by Sec62 and Sec63. The Sec61 channel alone assumes a fully closed conformation (the leftmost cartoon). Step 1: association of Sec63 opens the lateral gate (indicated by a red arrow) through interactions with Sec61 in both the cytosol and the ER lumen (indicated by red stars). The channel in this conformation is inactive due to the closed state of the plug domain. In addition, without Sec62, lipids may enter the open lateral gate. Step 2: Sec62 interacts with the lateral gate of Sec61 and further opens the lateral gate (blue arrow), which results in opening of the plug. The V-shaped transmembrane domain of Sec62 excludes lipids from the channel. Step 3: a substrate polypeptide inserts into the open pore of the channel as a loop with the signal sequence sitting at the lateral gate. Step 4: the signal sequence is cleaved by the signal peptidase (not shown), and the polypeptide is translocated into the ER lumen. For simplicity, the BiP ATPase, which drives translocation by interactions with the polypeptide and J domain, is not shown.

Many post-translational substrates are known to contain a signal sequence with relatively lower hydrophobicity (47). Eukaryotic post-translational substrates are also

expected to interact more transiently with Sec61 during initial insertion, because they are not tethered to the ribosome as in the co-translational mode or to the SecA ATPase as in the bacterial post-translational mode. These features of substrates for the Sec complex may require both the lateral and the vertical gates of the channel to be pre-opened for efficient insertion. A reduced energy barrier for substrate insertion by pre-opening the gates would allow polypeptides to promptly engage with the Sec61 complex, without which polypeptides may lose translocation competency because of premature folding or aggregation. Maintaining a stably open conformation by Sec63 and Sec62 may also be important for subsequent translocation steps because it may reduce friction in polypeptide movements. Our structural analysis shows that Sec63 and Sec62 open the gates of the Sec61 channel in a stepwise fashion to activate the channel, explaining their essentiality in cell viability. Given the high degree of sequence conservation of these components, the gating mechanism we discovered on the present study is probably conserved across all eukaryotic species.

3.4 Material and Methods

3.4.1 Yeast strains

A list of yeast strains used in this study is given in Supplementary Table 3.1.

The yeast strain (ySI7) used for purification of the WT *Sc*Sec complex has been described previously (68). Briefly, this strain expresses a fusion protein of Sec61β (Sbh1), Sec63 and a green fluorescent protein (GFP) from the genomic SEC63 locus under the endogenous promoter of SEC63 (the endogenous SBH1 copy is deleted). The C-terminus of Sbh1p and the N-terminus of Sec63 are separated by a glycine–serine linker that is 15 amino acids long. There is a flexible linker containing a tobacco etch virus (TEV) cleavage sequence between the C-terminus of Sec63 and GFP.

To enable purification of the PM *Sc*Sec complex, we generated strain ySI8 by modifying ySI7. We first clone the SEC61 gene (from 1,965 bp upstream to 668 bp downstream of the Sec61-coding sequence (CDS) of BY4741) into a pBlueScript-derived cloning vector (comprising a pUC origin and an ampicillin resistance gene). We then inserted a LEU2 selection marker cassette (amplified by PCR using pYTK075 as a template, a forward primer: 5′-agctaaataagatctTCGAGGAGAACTTCTAGTATATCTACATAC-3′, and a reverse primer: 5′- tatatataggagctcCTGCCTATTTAACGCCAAC-3′, upper case for LEU2-specific sequences and lower case for SEC61-specific sequences) was inserted between 125 bp and 126 bp downstream of the Sec61 stop codon by In-Fusion cloning (Takara Bio). Pore mutations (M90L/T185I/M294I/M450L) were introduced to Sec61 by site-specific mutagenesis. The resulting plasmid was then linearized by cutting the plasmid backbone with NotI. The DNA fragment was introduced into ySI7 by a standard lithium acetate/poly(ethylene glycol) transformation protocol. Recombinants were selected on a leucine drop-out synthetic complete (SC(−Leu)) agar medium. Incorporation of the mutations was verified by PCR and Sanger sequencing of single colonies.

To purify the FN3mut *Sc*Sec complex, we generated strain ySI73 by modifying strain TH_5187 (Horizon Discovery) from the Hughes' collection (45), where the expression of chromosomal Sec63 is under the control of a tetracycline-repressible

promoter. First, the endogenous copy of SBH1 of TH_5187 was replaced with a hygromycin resistance marker (hphMX) cassette. An hphMX cassette fragment was amplified by PCR using pFA6a-hphMX6 (74) as a template (forward primer: 5′-gggaaaagatttcaaccaccacttcaaaacaccacactctacctcctaccatactccataAGCTTGCCT CGTCCCC-3′; reverse primer: 5′-tagtcttgttttgtcaaatagggtggataaaagctgaatcattactg aagaaaattcttaCAGTATAGCGACCAGCATTCAC-3′; upper case for vector specific sequences and lower case for sequences homologous to yeast chromosomal sequences). The DNA fragment was transformed into TH_5187. Single colonies were isolated from YPD (1% yeast extract, 2% peptone, 2% glucose) agar plates containing 400 µg ml−1 of hygromycin (Gold Biotechnology) and integration was verified by PCR. The resulting strain (ySI48) was then further modified by integration of the FN3mut Sec63 construct into the HO locus using the transforming plasmid pSI74 (see below) linearized with HindIII, which cuts at the Escherichia coli kanamycin resistance marker (KanMX). Transformed cells were selected on SC(−Leu) agar medium and integration was verified by PCR.

For purification of the FN3mut/PM *Sc*Sec complex, we used strain ySI74. To generate ySI74, we first modified TH_5187 to contain the pore mutations in the SEC61 gene, similarly as described above for ySI8, but using a nourseothricin resistance cassette (natMX6) instead of the LEU2 marker. The natMX6 cassette was amplified from pFA6a-natMX6 (74) and inserted into the pBlueScript-Sec61 plasmid at 125 bp downstream of the Sec61 stop codon. After transformation of the linearized plasmid, recombinants were selected on YPD agar plates containing 100 µg ml−1 of nourseothricin (Gold Biotechnology), resulting in ySI42. Subsequently, SBH1 deletion and Sec63-FN3mut mutation were introduced to the strain as described for ySI73.

For purification of the FN3mut/Δ210–216 *Sc*Sec complex, we used strain ySI112. To generate ySI112 we modified strain ySI48 (TH_5187 sbh1Δ::hphMX6) by integration of the FM3mut/Δ210–216 Sec63 construct into the HO locus using the transforming plasmid pSI120 (see below) linearized with HindIII.

The WT and mutant *Tl*Sec complexes were expressed using the yeast strains ySI67 (for WT), ySI77 (for ΔSec62) and ySI113 (for Δanchor). These strains were generated from the parental strain yMLT62 (a gift from J. Thorner (75)), which expresses the β-estradiol-responsive chimeric transcription activator Gal4dbd.ER.VP16. All *Tl*Sec subunits were co-expressed with an integration vector (pYTK-e101) generated using MoClo Yeast ToolKit (YTK) (76) (see below). Expression of each gene is driven by a GAL1 promoter. The vector pYTK-e101 contains a natMX6 marker and URA3 homology sequences for chromosomal integration; pYTK-e101 encoding WT (pSI65) or mutant *Tl*Sec (pSI87 for ΔSec62 and pSI94 for Δanchor) was linearized with NotI and transformed into yMLT62. Recombinants were selected by growth on YPD agar plates containing 100 µg ml−1 of nourseothricin. Integration was verified by PCR as described (76).

For yeast growth complementation assays for Sec62, we generated ySI62, the chromosomal Sec62 expression of which can be repressed in the presence of doxycycline. The tetracycline response element (TRE), as well as the upstream kanMX cassette, were PCR amplified from genomic DNA of TH_5187 with primers containing 60-bp overhangs homologous to the N-terminus of Sec62 (forward primer: 5′-gacggaatagacgtgtcgttttcccaatactggcatacaaatcaagagggagaagagt

ggGGCGTTAGTATCGAATCG-3′; reverse primer: 5′-tgtagcagatccgccattga cactagcacctgcattgctacctggacctacggctgacatGGATCCCCCGAATTG- 3′; upper case for sequence specific to TRE-kanMX and lower case for sequences homologous to yeast chromosomal sequences). The amplicon was then transformed into the strain R1158 (the parental strain for TH_5187) which contains the 'tet activator'. Transformed cells were selected on 300 µg ml−1 of G418 (Fisher Chemical) containing YPD agar plates, and integration was verified by PCR.

Strain ySI89 was used for complementation assays testing synthetic growth defects of FN3mut Sec63 and Sec61 mutants (Fig. 3.6C). To generate this strain, TH_4087 (Hughes' strain with the chromosomal SEC61 expressing under a tetracycline-repressible promoter) was modified such that its endogenous Sec63 was mutated to FN3mut. A DNA segment encoding part of the FN3mut Sec63 was amplified by PCR from plasmid pSI16 (from amino acid 164 to the stop codon) and inserted into pFA6a-natMX6 immediately before an ADH1 terminator, which precedes the natMX6 cassette. The resulting construct was amplified by PCR to include 773 bp upstream of the first mutated amino acid (E440R) and 50 bp of the 3′-untranslated region of the SEC63 locus (forward primer: 5′-CCCTTACTGACGAATTGGTTAGGC-3′; reverse primer: 5′-atgtatctatttttataaagatgaaatatatacgtctaagagctaaaatgGGCCGCATAGGCCACTAG -3′; upper case for sequence specific to the plasmid and lower case for sequences homologous to yeast chromosomal sequence). The amplicon was transformed into TH_4087 and selected on 100 µg ml−1 of nourseothricin containing YPD agar plates. Incorporation of the mutation was verified using Sanger sequencing.

3.4.2 Plasmids

A list of plasmids used in this study is given in Supplementary Table 3.1.

The integration vectors pYTK-e101 and pYTK-e106, and CEN/ARS plasmid pYTK-e112, were generated using Golden Gate BsaI assembly of parts from MoClo YTK (76) (for pTYK-e101, part nos. were 8, 47, 73, 78, 86, 90 and 92; for pYTK-e106, part nos. were 8, 47, 73, 75, 88, 90 and 94; for pYTK-e112, part nos. were 8, 47, 73, 75, 81 and 84). The vector pYTK-e101 contains a natMX6 marker and integrates into the URA3 locus. The vector pYTK-e106 contains a LEU2 auxotroph marker and integrates into the HO locus.

The *Tl*Sec-expressing pYTK-e101 plasmids were generated using MoClo YTK as follows: first, gene fragments encoding *Tl*Sec subunits were chemically synthesized based on protein sequences of *T. lanuginosus* American Type Culture Collection 2000065 (https://gb.fungalgenomics.ca) and cloned into the YTK entry vector pYTK001 (76). Codons were optimized for yeast. In the case of the Sec63 and Sec61β subunits, a fusion construct (*Tl*Sec61β– GGSGGSGGSGGSGGS–*Tl*Sec63–TEV–GFP) was synthesized similarly to the expression of the *Sc*Sec complex. Each synthesized CDS was then cloned into the pYTK095 vector (76) as an expression cassette, together with a GAL1 inducible promoter, an ENO1 terminator and connector parts by Golden Gate BsaI assembly. Subsequently, the multigene expression construct was generated by Golden Gate BsmBI assembly of the pYTK095 plasmids and pYTK-e101, resulting in pSI65 (the Sec gene placed in tandem in the following order: *Tl*Sec61α, *Tl*Sec61γ, *Tl*Sec62, *Tl*Sec61β-*Tl*Sec63-GFP, *Tl*Sec71 and *Tl*Sec72). For ΔSec62 *Tl*Sec (plasmid pSI87), pYTK095-*Tl*Sec62 was replaced by a nonexpressing spacer cassette in the BsmBI

assembly. For Δanchor *Tl*Sec (plasmid pSI94), amino acid residues N319LF… WNE338 of *Tl*Sec62 were replaced with a Gly/Ser linker (GGSGGSGGS) before the multigene BsmBI assembly.

For expression of Sec63-mutant *Sc*Sec complexes (FN3mut and FN3mut/ Δ210–216), WT *Sc*Sec63 was first amplified from genomic DNA of BY4741 by PCR to include the endogenous promoter and terminator (187 bp upstream and 97 bp downstream of the CDS) and cloned into pYTK-e112 between the two BsaI sites (pSI5). This plasmid was then further modified to have Sbh1 and GFP flanking Sec63 as in other Sbh1–Sec63 fusion constructs (that is, Sbh1– GGSGGSGGSGGSGGS–Sec63–TEV–GFP). Then FN3mut (E440R/F481S/Δ441– 447) or FN3mut/Δ210–216 (FN3mut and residues L210PRFLVD216, replaced with SGSGGSG) mutations were introduced by site-specific mutagenesis. For generation of strains ySI74 and ySI112 (chromosomal integration of mutant Sec63 to the HO locus), the expression cassette for Sbh1–Sec63–GFP was transferred to pYTK-e106 by restriction digestion and ligation.

For growth complementation assays, SEC61 (710 bp upstream to 264 bp downstream of CDS) and SEC62 (251 bp upstream to 123 bp downstream of CDS) were amplified by PCR using genomic DNA of BY4741 and cloned into pYTK-e112, resulting in pSI123 and pSI39, respectively. Plasmids used for growth complementation assays of Sec63 mutants were derived from pSI5 (see above) by adding a TEV–GFP tag at the C-terminus of Sec63 (the Sbh1 fusion was not introduced, and thus the constructs have the native N-terminus).

3.4.3 Yeast growth complementation assays

The yeast strains were transformed with each pYTK-e112 plasmid encoding the indicated protein under its endogenous promoter. Cells were selected on SC(−Leu) agar medium. Single colonies were picked and grown overnight in SC(−Leu) medium. The cultures were diluted with water to an optical density of 600 nm (OD600) of 1.0 and further serially diluted by factors of 10 (in Fig. 3.6B,C, starting concentration was OD600 = 0.1). The diluted cultures (10 µl each) were spotted on SC(−Leu) agar plates. In the case of Fig. 3.3D (bottom two panels only), YPD agar medium was used. Where indicated, plates contained 10 µg ml−1 of doxycycline. Plates were incubated at 30 °C unless otherwise stated. The following strains were used for the indicated experiment: TH_5187 (Fig. 3.6B left panel, Fig. 3.10B and Fig. 3.7AB), ySI42 (Fig. 3.6B right panel), ySI89 (Fig. 3.6C) and ySI62 (Fig. 3.3D).

3.4.4 Protein purification

For purification of *Sc*Sec complexes, yeast cells (ySI7 for WT, ySI8 for PM, ySI73 for FN3mut, ySI74 for FN3/Δ210–216) were grown in YPD medium to OD600 of 2–3, before harvest. For purification of *Tl*Sec, cells were grown in YPD medium to OD600 of 1.0. After adding 50 nM β-estradiol, cells were further grown until reaching OD600 of 2–3. All cultures were grown in 30 °C, except for the FN3mut/PM and FN3/Δ210–216 variants of *Sc*Sec, for which cells were grown at 22 °C. Cells were harvested by centrifugation (8 min at 6,400g), washed once with ice-cold Tris-buffered saline (20 mM Tris, pH 7.5, and 150 mM NaCl), frozen in liquid nitrogen and stored at −75 °C before use.

All *Sc*Sec and *Tl*Sec complexes were purified as described previously (68). Briefly, cells were lysed by cryo-milling and resuspended in buffer containing 50 mM Tris, pH 7.5, 200 mM NaCl, 1 mM ethylenediaminetetraacetic acid (EDTA), 10% glycerol, 2 mM dithiothreitol (DTT), 5 μg l^{-1} of aprotinin, 5 μg l^{-1} of leupeptin, 1 μg ml^{-1} of pepstatin A and 1.2 mM phenylmethylsulfonyl fluoride. Membranes were solubilized by adding 1% lauryl maltose neopentyl glycol (Anatrace) and 0.2% cholesteryl hemisuccinate (Anatrace) directly to the whole-cell lysate for 1.5 h at 4 °C. The lysate was clarified by ultracentrifugation at 125,000g for 1 h. The Sec complex was bound to agarose beads conjugated with anti-GFP nanobody and the buffer was exchanged with 50 mM, Tris pH 7.5, 200 mM NaCl, 1.0 mM EDTA, 2 mM DTT, 0.02% glycol-diosgenin (Anatrace) and 10% glycerol. The complex was eluted by incubating the beads with TEV protease (~10 μg ml^{-1}) overnight and further purified by size-exclusion chromatography (Superose 6 Increase, GE Life Sciences) in 20 mM Tris pH 7.5, 100 mM NaCl, 1 mM EDTA, 2 mM DTT and 0.02% glycol-diosgenin. Peak fractions were concentrated to ~5 mg ml^{-1} and used immediately for cryo-EM. We note that the yields of all mutant *Sc*Sec complexes were comparable to those of the WT complex.

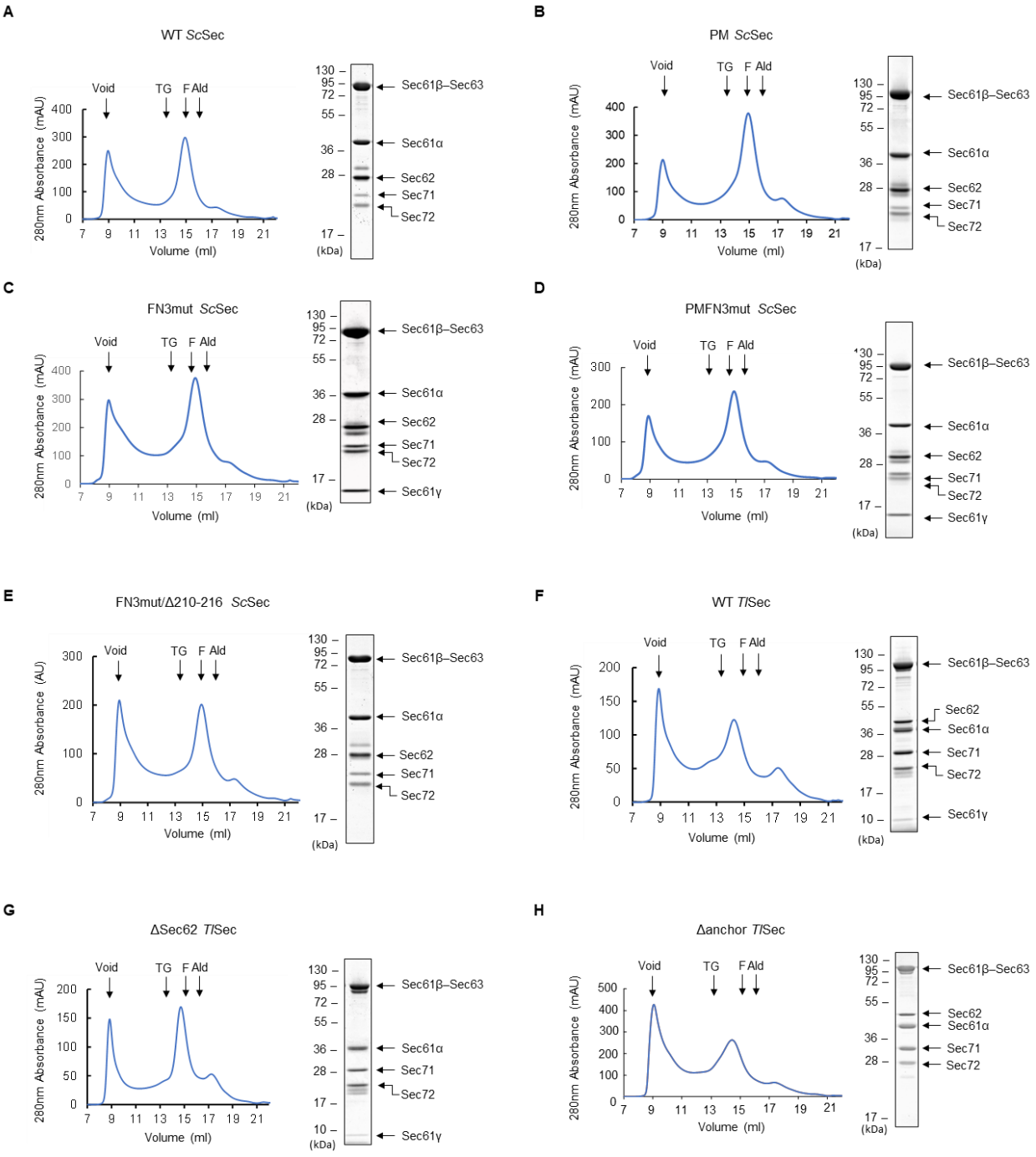

Figure 3.13 Purification of the Sec Complexes. A-H. Left panel, chromatogram from Superose 6 size-exclusion chromatography of the affinity purified Sec complexes (MW standards: Tg, thyroglobulin; F, ferritin; Ald, aldolase). Right panel, the Coomassie-stained SDS-PAGE gel of the Superose 6 peak fraction. In some of the gels, Sec61γ (~10 kDa) migrated off the bottom.

3.4.5 Cryo-EM grid preparation and data collection

Purified samples were supplemented with 3 mM fluorinated Fos-Choline-8 (Anatrace) before plunge freezing. The samples were applied on holey carbon gold grids (Quantifoil 1.2/1.3, 400 mesh) that were glow discharged for 35 s using PELCO easiGlow glow discharge cleaner. Plunge freezing was performed using Vitrobot Mark IV (FEI) set at 4 °C and 100% humidity. Whatman No. 1 filter paper was used to blot the samples.

Datasets for *Tl*Sec, ΔSec62 *Tl*Sec and FN3mut/Δ210–216 *Sc*Sec were collected on an FEI Talos Arctica electron microscope operated at an acceleration voltage of 200 kV. Datasets for WT *Sc*Sec, PM *Sc*Sec, FN3mut *Sc*Sec, FN3mut/PM *Sc*Sec and Δanchor *Tl*Sec were collected on an FEI Titan Krios electron microscope operated at an acceleration voltage of 300 kV and equipped with a Gatan Quantum Image Filter (a slit width of 20 eV). Both microscopes operated using SerialEM software (50). Videos were recorded on a Gatan K3 Summit direct electron detector under the super-resolution mode (with a physical pixel size of 1.14 Å for *Tl*Sec and ΔSec62 *Tl*Sec, 0.9 Å for FN3mut/Δ210–216 *Sc*Sec, and 1.19 Å for WT *Sc*Sec, FN3mut *Sc*Sec, FN3mut/PM *Sc*Sec and Δanchor *Tl*Sec) with the exception of PM *Sc*Sec, which utilized a Gatan K2 Summit direct election detector (with physical pixel size of 1.15 Å). The samples were exposed to a total dose of ~50 e− per Å2 applied over 42 frames. Defocus target was typically set between −0.8 µm and −2.4 µm. For detailed parameters, see also Tables 3.1 and 3.2.

3.4.6 Cryo-EM image analysis

Micrographs collected from the microscopes were preprocessed by Warp (77). Video stacks were corrected for gains and subjected to tile-based motion correction and CTF estimation (7 × 5 tiles for datasets from the K3 detector and 5 × 5 for datasets from the K2 detector). Particles were automatically picked using the BoxNet algorithm of Warp. Low-quality micrographs and particles, such as those containing crystalline ice or showing excessive motion blur, were removed by manual inspection. Motion-corrected videos were exported with 2× pixel and 2× frame binning. Local particle motion corrections were performed in cryoSPARC v.2 (52) after importing particle metadata and motion-corrected video stacks. Box sizes of extracted particle images were 256 pixels except for the FN3mut/Δ210–216 *Sc*Sec dataset, which was 320 pixels. All subsequent single-particle analyses were performed with cryoSPARC v.2 as described below. In the cases of the WT and FN3mut/Δ210–216 *Sc*Sec datasets, particle images extracted from Warp were directly used without local motion correction.

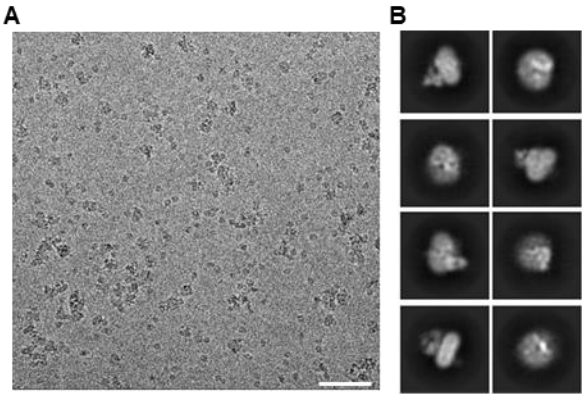

Figure 3.14 Representative cryo-EM micrograph and 2D class averages. A. Micrograph collected from WT *Tl*Sec complex. Scale bar, 50 nm. **B**. Select 2D class averages for WT *Tl*Sec.

(1) WT *Sc*Sec: the single-particle analysis procedure for WT *Sc*Sec is outlined in Fig. 3.15. First, 2,686,839 picked particles were subjected to two-dimensional (2D) classification, where empty micelles and classes of poor quality were removed. Selected 1,679,300 particles were then subjected to reconstruction from scratch to yield three initial models, followed by heterogeneous refinement using the initial maps (unless stated otherwise, particle images were 2× scaled down to 128 × 128 pixels^2 in all heterogeneous refinements). Features of the Sec complex appeared in only one class (1,172,728 particles), particles of which were subjected to a second iteration of heterogeneous refinement, with the three classes from the first heterogeneous refinement as references to further remove poor-quality particles. The resulting 995,878 particles were then subjected to a round of nonuniform refinement, local CTF refinement and another round of nonuniform refinement, yielding a map at 2.98-Å resolution (consensus map). To separate the particles into classes containing and lacking Sec62, the NTD density of Sec62 in the consensus map was manually erased using UCSF Chimera (59) and was used alongside the consensus map as initial references for heterogeneous refinement. This yielded two classes: *Sc*Sec[Sec62−] with 391,885 particles which is largely devoid of detectable Sec62 and *Sc*Sec[Sec62+] with 603,993 particles. After nonuniform refinement, both classes refined to a resolution of 3.07 Å. To further separate into subclasses containing different conformations of Sec62, the particles of *Sc*Sec[Sec62+] were subjected to a round of reconstruction from scratch and heterogeneous refinement to yield five new classes. This step produced two major classes: one lacking Sec71–Sec72 (142,768 particles) and one showing the full complex features (415,818 particles). Particles of the latter class were subjected to a second round of reconstruction from scratch and heterogeneous refinement, yielding five new classes. Of these, two major classes showing the prominent features of the Sec complex (the other three classes did not show clear features of *Sc*Sec) were further refined using nonuniform refinement to yield the final maps of *Sc*Sec[C1] (from 193,263 particles) and *Sc*Sec[C2] (from 193,661 particles) at overall resolutions of 3.16 and 3.14 Å, respectively.

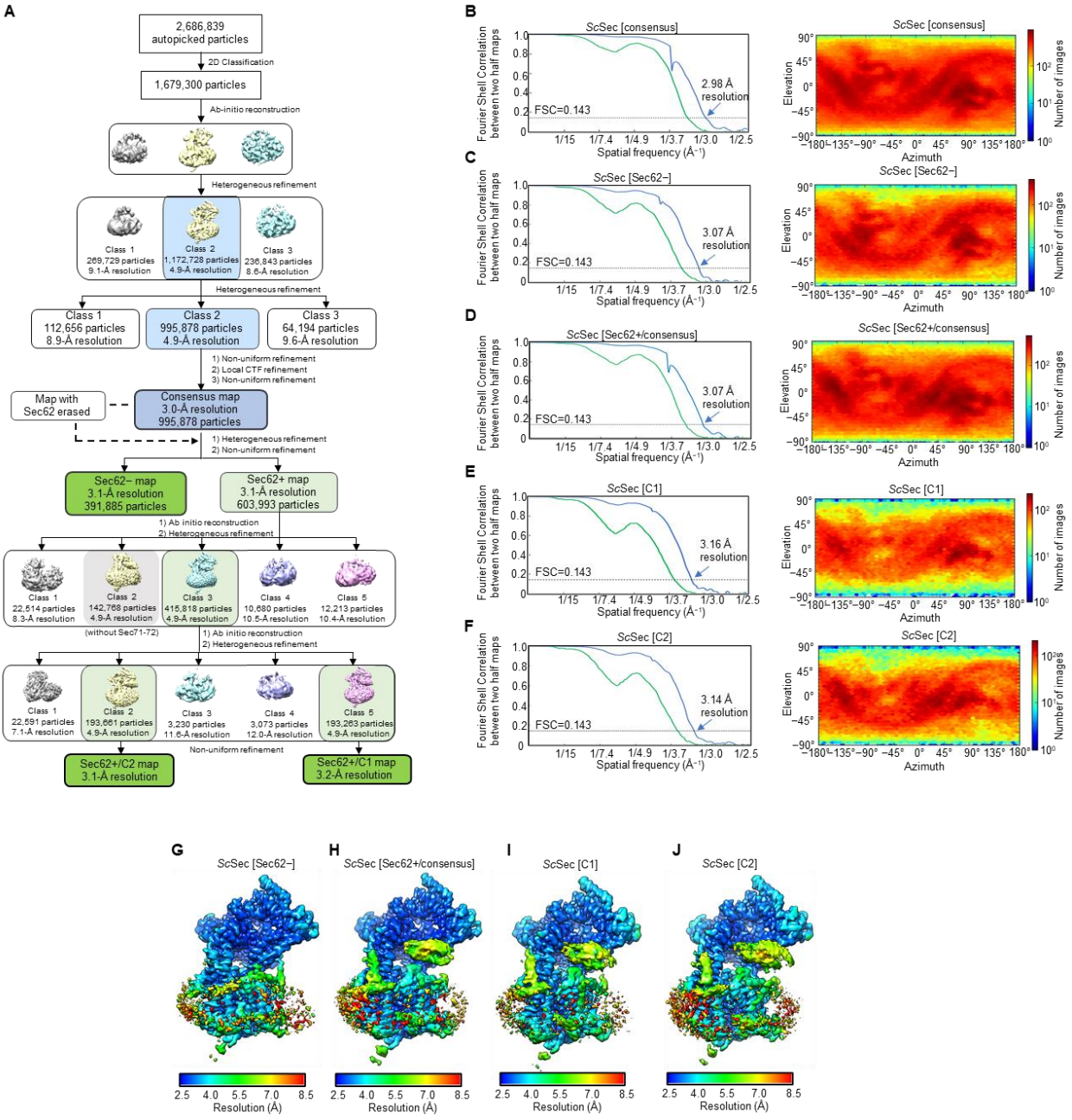

Figure 3.15 Cryo-EM analysis of the wild-type (WT) *S. cerevisiae* Sec complex (*Sc*Sec). A. A diagram of the cryo-EM single particle analysis procedure. **B-F**. Fourier shell correlations (FSCs, left) and cryo-EM particle orientations (right) for the *Sc*Sec complex consensus map (B), Sec62 lacking map (C), and the two conformations with Sec62, *Sc*Sec [C1] (E) and *Sc*Sec [C2] (F). Blue FSC curve is tight mask (corrected) curve and green is spherical mask curve. **G-J.** local resolution distribution for the *Sc*Sec complex consensus map (G), Sec62 lacking map (H), and the two conformations with Sec62, *Sc*Sec [C1] (I) and *Sc*Sec [C2] (J).

(2) PM *Sc*Sec: the PM *Sc*Sec dataset was analyzed using essentially the same procedure as for WT *Sc*Sec but starting with a dataset of 195,915 auto-picked particles (Fig. 3.16). After a round of 2D classification, reconstruction from scratch and heterogeneous refinement, the consensus class (91,813 particles) was obtained, which was subjected to nonuniform refinement to yield a 3.53-Å-resolution map. As with WT

*Sc*Sec, the particles were further classified to [Sec62−] and [Sec62+] classes by heterogeneous refinement (35,573 and 56,240 particles, respectively), and the structures were refined to maps at resolutions of 4.02 and 3.78 Å, respectively. Particles of the [Sec62+] class were further classified by reconstruction from scratch and heterogeneous refinement (five classes). One class (13,752 particles) lacked the Sec71–72 subunits and the main class (36,506 particles) showed features of the full complex. The particles from the latter class were subjected to another round of reconstruction from scratch and heterogeneous refinement, yielding two main classes, PM *Sc*Sec[C1] (17,341 particles) and PM *Sc*Sec[C2] (16,679 particles), which were further refined with nonuniform refinement to overall resolutions of 4.06 and 4.04 Å, respectively.

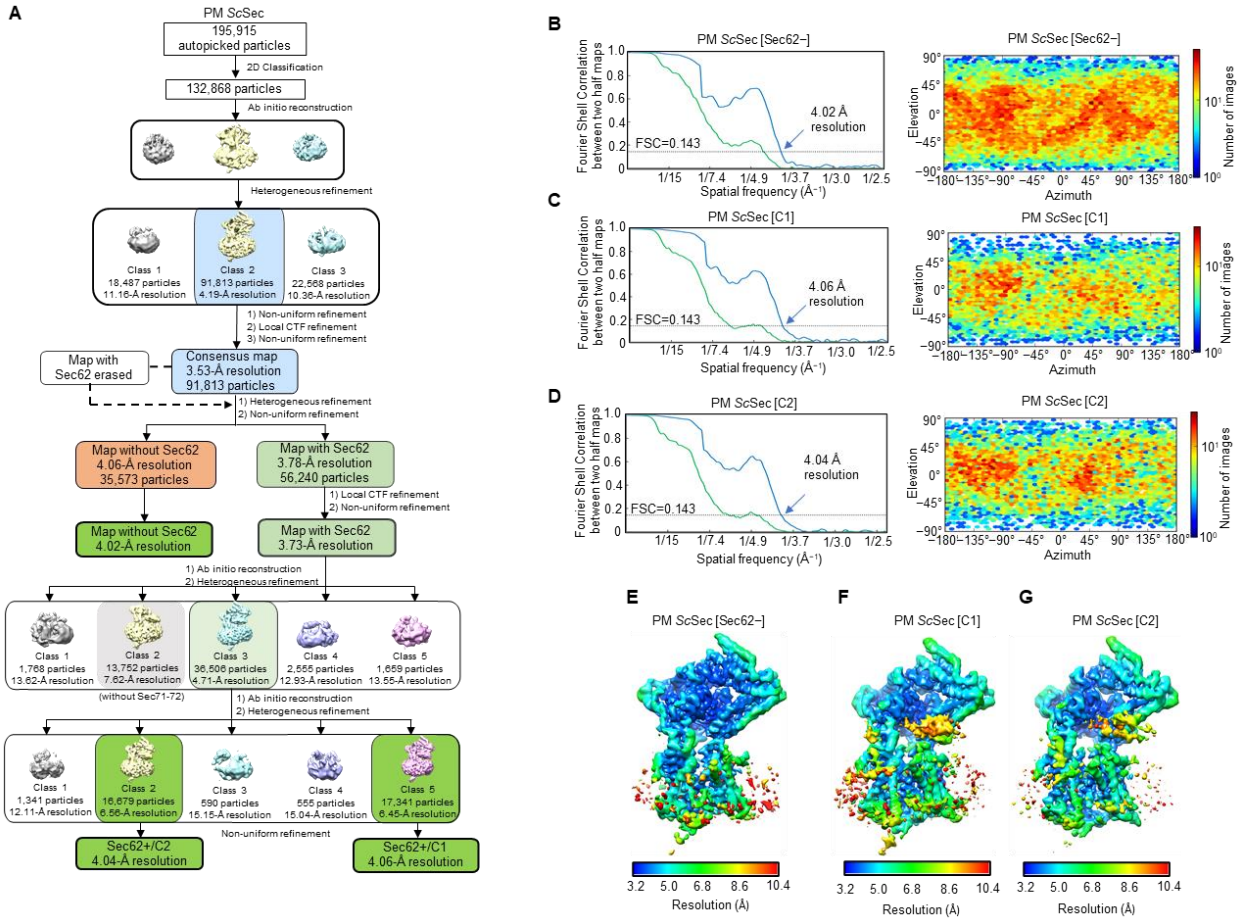

Figure 3.16 Cryo-EM analysis of the pore mutant *S. cerevisiae* Sec complex (*Sc*Sec). A. A diagram of the cryo-EM single particle analysis procedure. **B**-**D**. Fourier shell correlations (FSCs, left) and cryo-EM particle orientations (right) for the Sec62 lacking PM *Sc*Sec complex map (b), and the two conformations with Sec62, PM *Sc*Sec [C1] (c) and PM *Sc*Sec [C2] (d). Blue FSC curve is tight mask (corrected) curve and green is spherical mask curve. **E**-**F** local resolution distribution for the Sec62 lacking PM *Sc*Sec complex map (e), and the two conformations with Sec62, *Sc*Sec [C1] (f) and *Sc*Sec [C2] (j).

(3) FN3mut *Sc*Sec: the single-particle analysis procedure is outlined in Fig. 3.17. The initial set of 1,274,219 auto-picked particles were subjected to 2D classification. After discarding empty micelle classes and classes showing poor features (resulting in 412,129 particles), we generated five initial models with reconstruction from scratch. Only one class showed features of the Sec complex. Particles were subjected to two rounds of heterogeneous refinement to further remove particles of poor quality. The resulting 202,091 particles were used for nonuniform refinement, which was followed by local CTF refinement and a second round of nonuniform refinement to obtain a consensus map at 3.73-Å resolution. Similar to WT *Sc*Sec, these particles were further classified into two classes, one with Sec62 (FN3mut *Sc*Sec[Sec62+], 119,420 particles) and the other without Sec62 (FN3mut *Sc*Sec[Sec62−], 82,671 particles) using the consensus map and Sec62-NTD-erased map as initial references for heterogeneous refinement. FN3mut *Sc*Sec [Sec62+] and [Sec62−] particles were separately subjected to local CTF refinement and nonuniform refinement to yield final maps at 3.90- and 4.01-Å resolution, respectively. Further 3D classification of particles from the [Sec62+] class did not result in classes with a noticeable conformational difference.

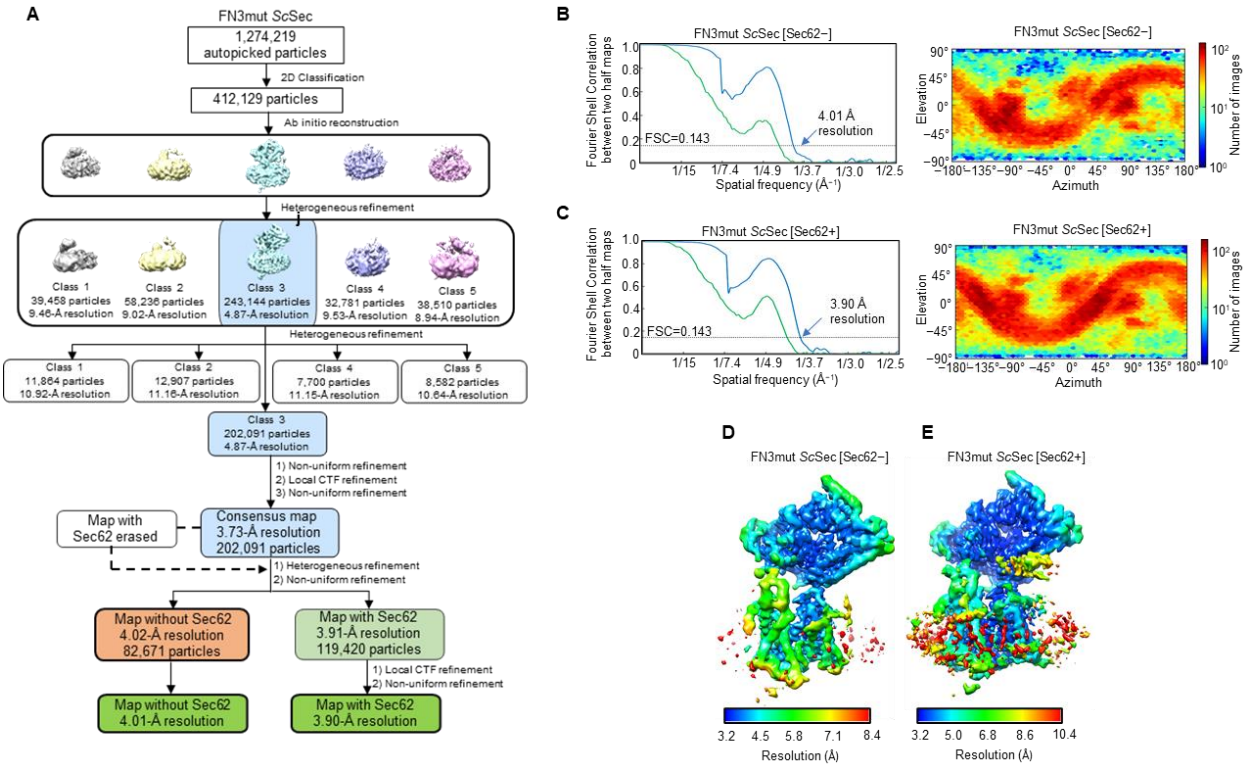

Figure 3.17 Cryo-EM analysis of the FN3 mutant *S. cerevisiae* Sec complex (*Sc*Sec). A. A diagram of the cryo-EM single particle analysis procedure. **B-C**, Fourier shell correlations (FSCs, left) and cryo-EM particle orientations (right) for the Sec62 lacking FN3 *Sc*Sec complex map (B), and Sec62 containing, FN3 *Sc*Sec (C). Blue FSC curve is tight mask (corrected) curve and green is spherical mask curve. **D**-**E** Local resolution distribution for the Sec62 lacking FN3 *Sc*Sec complex map (D), and the Sec62 containing map (E).

(4) FN3mut/PM *Sc*Sec: the single-particle analysis procedure is outlined in Fig. 3.18. The analysis was processed similarly to FN3mut *Sc*Sec. The initial set of 267,541 auto-picked particles was first cleaned up by 2D classification. The resulting 146,399 particles were subjected to reconstruction from scratch (three classes). Only one main class showed features of the Sec complex. The 146,399 particles were then subjected to two rounds of heterogeneous refinement to remove non-Sec-complex particles. The resulting 86,843 particles were then subjected to nonuniform refinement, which was followed by local CTF refinement and a second round of nonuniform refinement to obtain a consensus map at 3.73-Å resolution. The particles were further classified to [Sec62+] and [Sec62−] classes (54,139 and 32,704 particles, respectively) with heterogeneous refinement, and final maps of PM/FN3mut *Sc*Sec [Sec62+] and [Sec62−] at 3.99- and 4.35-Å resolution, respectively, were obtained by nonuniform refinement followed by local CTF refinement and a second round of nonuniform refinement. Further 3D classification of particles from the [Sec62+] class did not yield classes with a noticeable conformational difference.

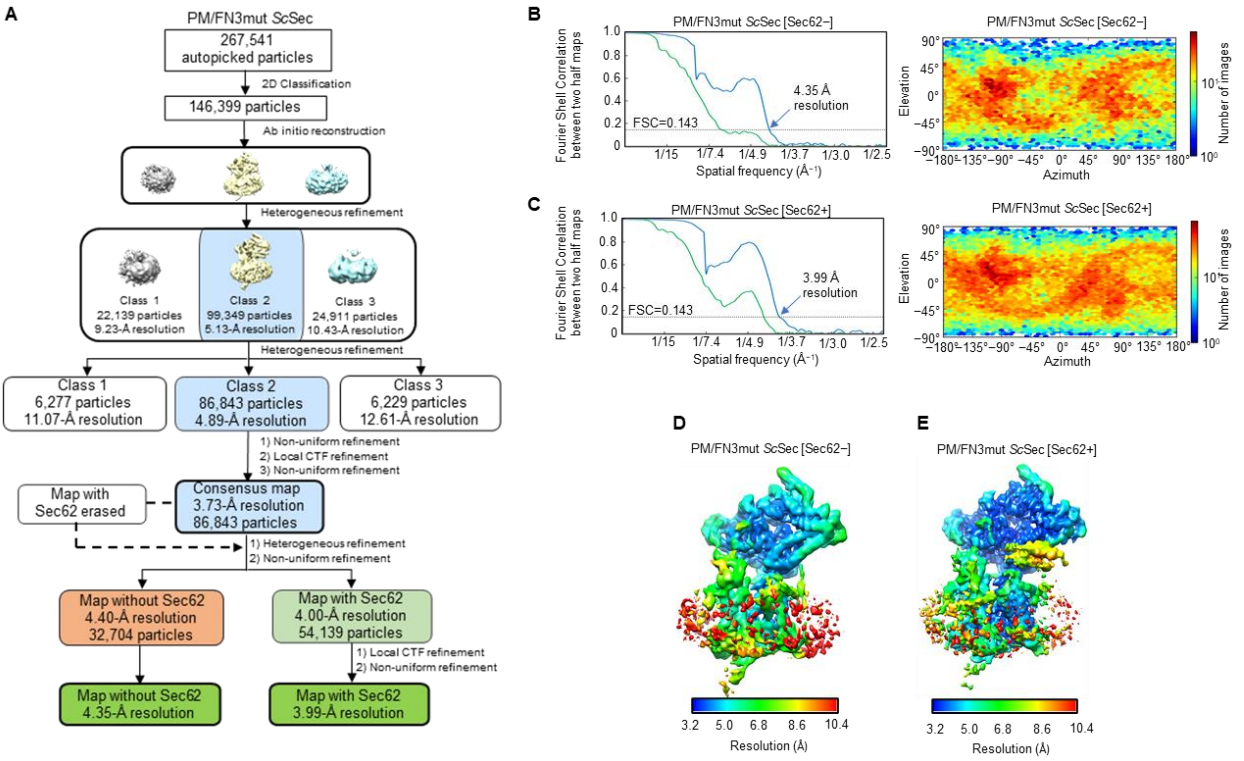

Figure 3.18 Cryo-EM analysis of the FN3 and PM double mutant *S. cerevisiae* Sec complex (*Sc*Sec). A. A diagram of the cryo-EM single particle analysis procedure. **B-C**, Fourier shell correlations (FSCs, left) and cryo-EM particle orientations (right) for the Sec62 lacking PM/FN3mut *Sc*Sec complex map (B), and Sec62 containing, PM/FN3mut *Sc*Sec (C). Blue FSC curve is tight mask (corrected) curve and green is spherical mask curve. **D-E** Local resolution distribution for the Sec62 lacking PM/FN3mut *Sc*Sec complex map (D), and the Sec62 containing map (E).

(5) FN3mut/Δ210–216 *Sc*Sec: the single-particle analysis procedure is outlined in Fig. 3.19. The initial set of 2,270,392 auto-picked particles were cleaned up by 2D classification. The resulting 646,998 particles were used to generate four initial maps with reconstruction from scratch. Only one main class showed features of the Sec complex. Two rounds of heterogeneous refinement (with particle image 2× scaled down to 160 × 160 pixels^2) were performed to enrich particles of the Sec complex. The resulting 282,555 particles were subjected to nonuniform refinement, followed by local CTF refinement and a second round of nonuniform refinement to produce a 3.80-Å resolution map. The particles were then subjected to a second round of reconstruction from scratch and heterogeneous refinement to generate four classes. Of these classes, two showed features of the Sec complex (131,010 and 126,221 particles), maps of which were nearly identical. Particles of the two classes were combined for nonuniform refinement to yield the final map at 3.75-Å resolution.

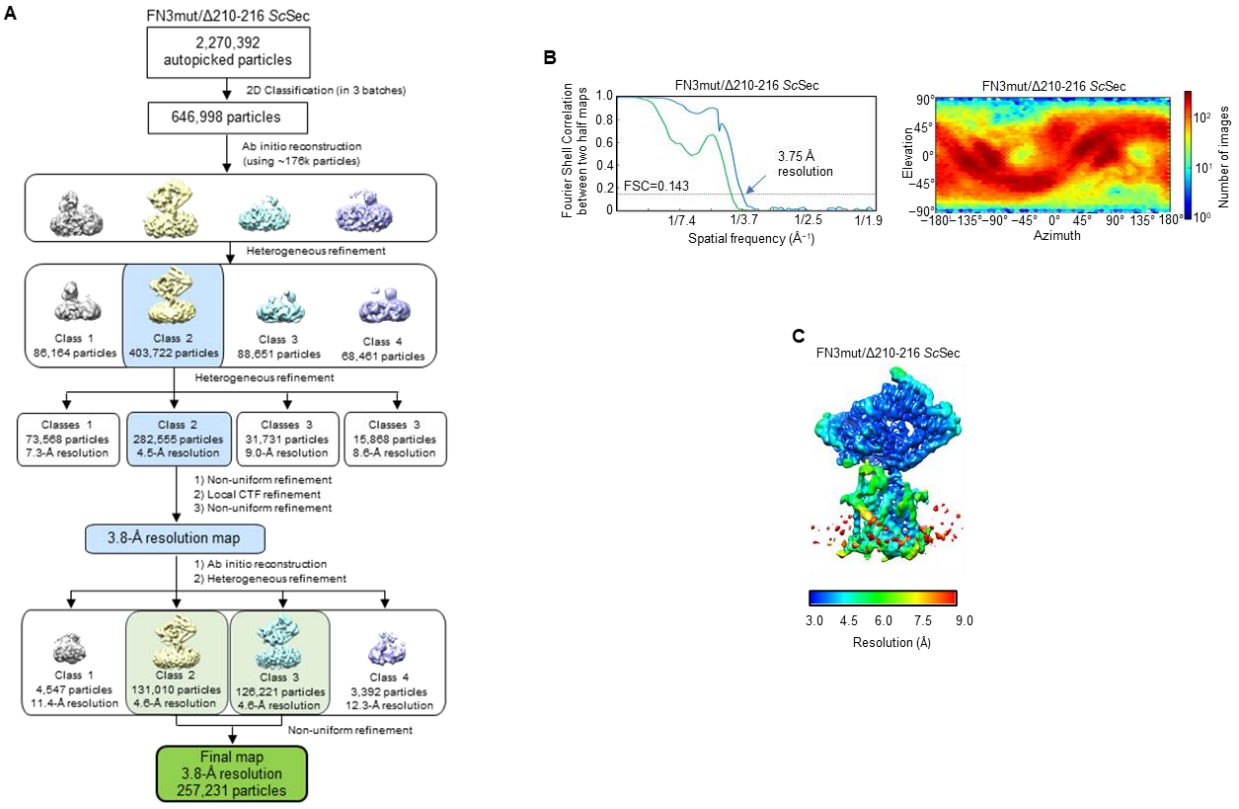

Figure 3.19 Cryo-EM analysis of the FN3 and Δ210-216 double mutant *S. cerevisiae* Sec complex (*Sc*Sec). A. A diagram of the cryo-EM single particle analysis procedure. **B.** Fourier shell correlations (FSCs, left) and cryo-EM particle orientations (right). Blue FSC curve is tight mask (corrected) curve and green is spherical mask curve. **C.** Local resolution distribution.

(6) WT *Tl*Sec: the single-particle analysis procedure is outlined in Fig. 3.20. The initial set of 1,632,719 auto-picked particles was subjected to 2D classification in two batches to remove empty micelles and poor-quality particles. The resulting 789,004 particles were used to generate five initial 3D maps with reconstruction from scratch. Only one (main) class showed features of the Sec complex. The 789,004 particles were subjected to heterogeneous refinement using the initial maps as references, which was followed by a second round of heterogeneous refinement. The resulting main class (427,835 particles) was refined using nonuniform refinement, local CTF refinement and a second nonuniform refinement, yielding a consensus map at 3.61-Å resolution. As with WT *Sc*Sec, particles were further classified to [Sec62+] and [Sec62−] classes with heterogeneous refinement using the consensus map and a Sec62-NTD-erased map as references (272,224 and 155,601 particles, respectively). The classes were further refined with nonuniform refinement yielding a 3.88-Å-resolution map of *Tl*Sec[Sec62−] and a 3.75-Å-resolution map of *Tl*Sec[Sec62+]. Particles of the [Sec62+] class (272,224 particles) were further subjected to reconstruction from scratch and heterogeneous refinement (five classes). Two major classes (114,704 and 143,227 particles) showed the features of the Sec complex, which were further refined to the final maps of [Sec62+/plug-open] and [Sec62+/plug-closed] at overall resolutions of 4.02 and 3.76 Å, respectively. Unlike WT *Sc*Sec, a class lacking Sec71-ec72 was not identified.

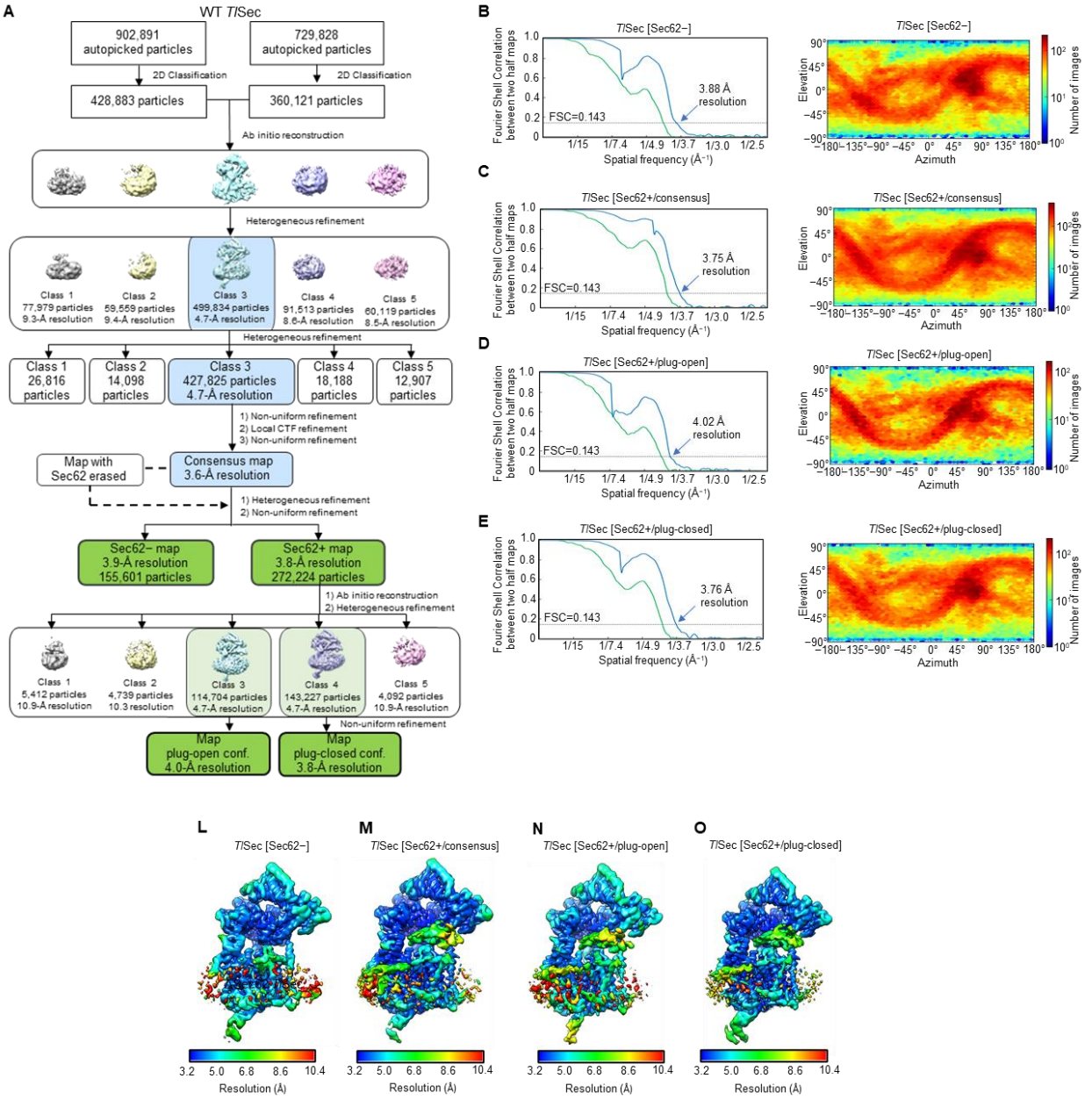

Figure 3.20 Cryo-EM analysis of the wild-type (WT) *T. lanuginosus* Sec complex (*Tl*Sec). A. A diagram of the cryo-EM single particle analysis procedure. **B-F**. Fourier shell correlations (FSCs, left) and cryo-EM particle orientations (right) for the Sec62 lacking *Tl*Sec complex map (B), Sec62 containing consensus map (C), *Tl*Sec [Sec62+/plug-open], (E) and *Tl*Sec [Sec62+/plug-closed] (F). Blue FSC curve is tight mask (corrected) curve and green is spherical mask curve. **G-J.** local resolution distribution for the Sec62 lacking *Tl*Sec complex map (G), Sec62 containing consensus map (H), *Tl*Sec [Sec62+/plug-open] (I) and *Tl*Sec [Sec62+/plug-closed] (J).

(7) ΔSec62 *Tl*Sec: the single-particle analysis procedure is outlined in Fig. 3.21. The initial set of 546,712 auto-picked particles was subjected to two rounds of 2D classification with removal of poor classes in each round, resulting in 258,743 particles. Five initial 3D models were generated from the 258,743 selected particles by reconstruction from scratch and further refined by heterogeneous refinement. This produced two major classes (77,524 and 114,523 particles) which showed features of the Sec complex. Particles from the two classes were combined and refined with nonuniform refinement, local CTF refinement and a second nonuniform refinement, yielding the final map at 3.74-Å overall resolution.

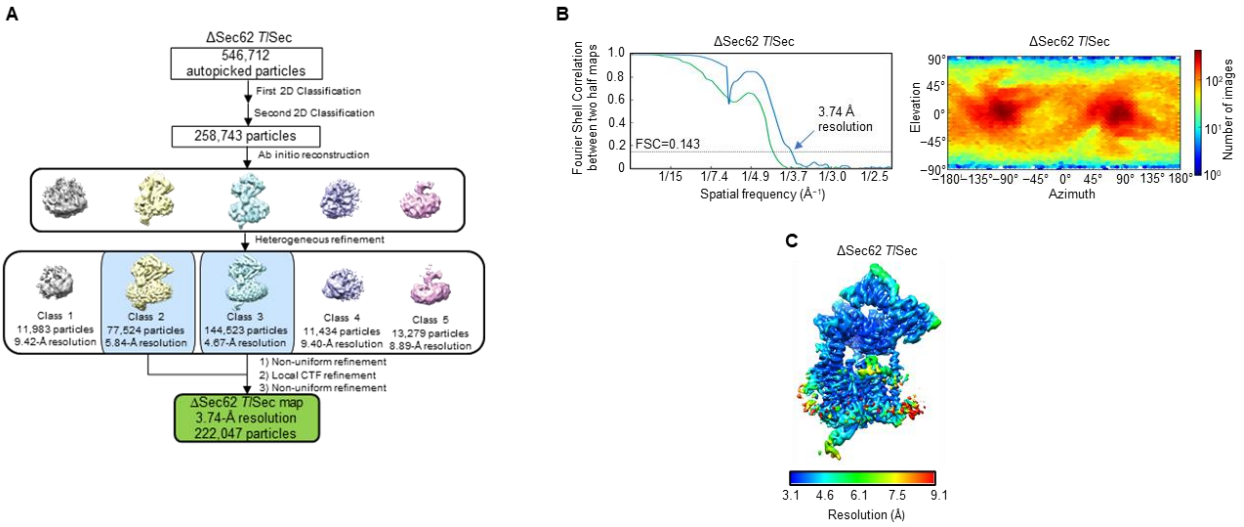

Figure 3. 21 Cryo-EM analysis of the ΔSec62 *T. lanuginosus* Sec complex (*Tl*Sec). A. A diagram of the cryo-EM single particle analysis procedure. **B.** Fourier shell correlations (FSCs, left) and cryo-EM particle orientations (right). Blue FSC curve is tight mask (corrected) curve and green is spherical mask curve. **C.** Local resolution distribution.

(8) Δanchor *Tl*Sec: the initial set of 229,825 auto-picked particles was subjected to 2D classification, resulting in 105,578 particles. Three initial 3D models were generated by reconstruction from scratch and refined by heterogeneous refinement. One major class (76,726 particles) showed features of the Sec complex, and the particles from this class were used to generate the final map at 4.38-Å resolution with nonuniform refinement (Fig 3.22).

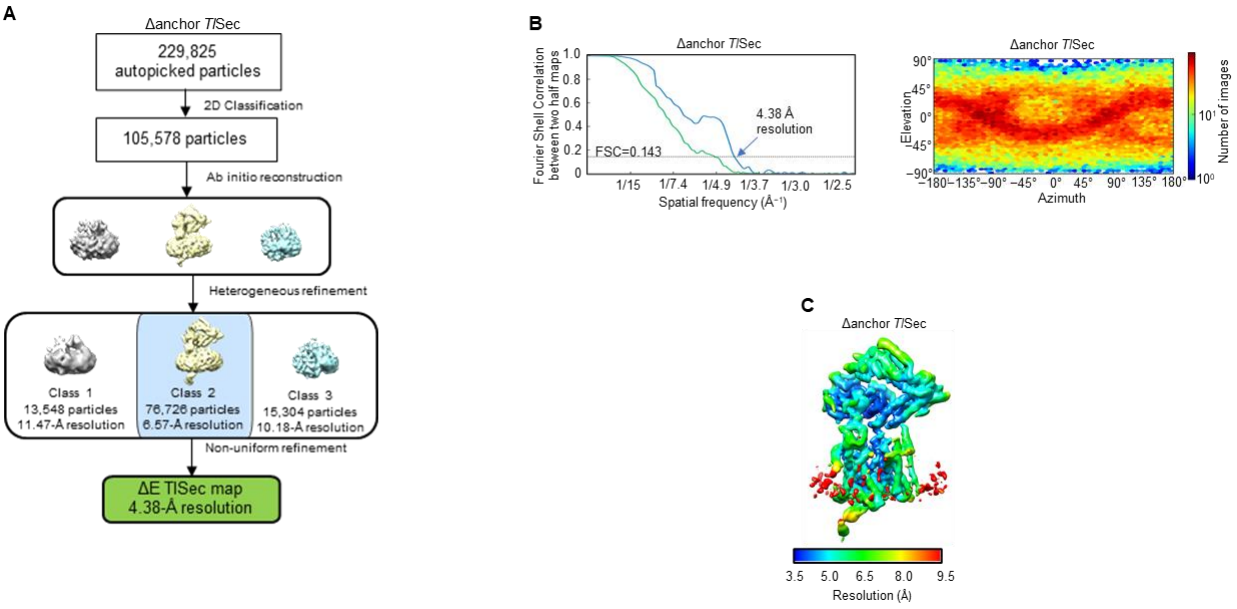

Figure 3. 22 Cryo-EM analysis of the Δanchor *T. lanuginosus* Sec complex (*Tl*Sec). A. A diagram of the cryo-EM single particle analysis procedure. **B.** Fourier shell correlations (FSCs, left) and cryo-EM particle orientations (right). Blue FSC curve is tight mask (corrected) curve and green is spherical mask curve. **C.** Local resolution distribution.

3.4.7 Atomic model building

Atomic models were built using Coot (54). We first built models for *Sc*Sec[Sec62−] and ΔSec62 *Tl*Sec using our previous *Sc*Sec model (PDB 6N3Q) (68) as a template. For ΔSec62 *Tl*Sec, we generated a homology model using SWISS-MODEL (78), which was rebuilt into the map using Coot. The *Sc*Sec[Sec62−] model was then used to build models for *Sc*Sec[C1] and *Sc*Sec[C2]. For *Sc*Sec62, a poly(alanine) model was built into densities. Atomic models for all the mutant ScSec structures lacking Sec62 were also built starting from the *Sc*Sec[Sec62−] model. The *Sc*Sec[Sec62−] model was first fitted into each map using UCSF Chimera and further fitted into the map in groups of domains and subunits using rigid body refinement in Phenix (55). The models were then locally adjusted in Coot. Models for PM *Sc*Sec[C1] and PM *Sc*Sec[C2] were built similarly using the WT *Sc*Sec[C1] and *Sc*Sec[C2] models as starting models. Models for FN3mut *Sc*Sec[Sec62+] and PM/FN3mut *Sc*Sec[Sec62+] were built starting with the WT *Sc*Sec[C2] and PM/FN3mut *Sc*Sec[Sec62−] model, respectively. ΔSec62 *Tl*Sec was used as a starting model to build all *Tl*Sec structures.

The models were refined with Phenix real-space refinement using combined maps that were sharpened with a B factor estimate based on the Guinier plot and low pass filtered at their overall resolution (produced by cryoSPARC). The refinement resolution was also limited to the overall resolution of the maps in Phenix. Secondary structure restraints were used during the refinement. MolProbity (56) was used for structural validation. For refinement and validation statistics, see Tables 3.1 and 3.2.

UCSF Chimera (59), ChimeraX (79) and PyMOL (Schrödinger) were used to prepare figures in the article. Unless stated otherwise, all shown cryo- EM maps are unsharpened maps that were low pass filtered at their overall resolution.

3.4.8 MD simulations

Protein models of *Sc*Sec[C1], *Sc*Sec[C2], *Sc*Sec[Sec62−], WT *Tl*Sec and ΔSec62 *Tl*Sec suitable for MD simulation were built from the cryo-EM-derived atomic models. Missing areas of the overall complexes were modeled in using SWISS-MODEL55, although omitting the unstructured region of *Tl*Sec63, residues 482–526. The sequence of the TM portion of Sec62 was mapped on to the structure; gaps in the structures of other proteins were modeled except for the J domain of Sec63. MD flexible fitting (80) was used to fit the newly modeled pieces of the structures to optimize their positions within the density maps, including the Sec61 plug. All five systems were placed in a realistic yeast ER membrane with 47% POPC, 20% POPE, 10% PLPI, 8% POPS, 3% POPA, 10% ERG, 1% TLCL and 1% DYGL60,61 using CHARMM-GUI (81,82). The membrane protein systems were placed in a TIP3 (83) water box and neutralized with 0.15 M KCl. The all-atom systems ranged from 250,000 to 270,000 atoms in size.

All simulations were run using NAMD 2.14 (84) with the CHARMM36m (protein) (85,86) and CHARMM36 (lipid) (87) force fields as well as hydrogen mass repartitioning (88). Positional restraints were initially placed on all atoms in each system and were gradually released in two consecutive runs: 0.5 ns with only the lipid tails unrestrained and 1 ns with the protein restrained. Subsequent 200-ns runs maintained restraints on the protein backbone to focus on the behavior of lipids for a given conformation of the Sec complex. All simulations were performed at a constant temperature of 310 K using Langevin dynamics (damping coefficient 1/ps), a constant pressure of 1 atm using Langevin piston and periodic boundary conditions. As hydrogen mass repartitioning was used, the time step was set to 4 fs. Short-range, nonbonded interactions were cut off at 12 Å, with a force-based switching function starting at 11 Å. Long-range, nonbonded interactions were calculated using a particle-mesh Ewald method with grid spacing of at least 1/Å3 (89). Total simulation time between all systems was 1.4 μs. Setup, analysis and visualization were carried out using visual molecular dynamics (90).

Supplementary Table 3.1. Yeast strains and plasmids used in this study

Name	Genotype / Description	Source
Yeast strains		
BY4741	*MAT***a** *his3-1*, *leu2-0*, *met15-0*, *ura3-0*	Horizon Discovery
yMLT62	*MAT***a** *leu2-0*::*pACT1-GEV*::*HIS3*, *rps9Δ*, *mek1Δ*, *his3-1*, *met15-0*, *ura3-0*	(74)
R1158	BY4741 *URA3*::*pCMV-tTA*	(73)
TH_4087	R1158 *pSEC61*::*KanMX*-tetO$_7$-*pCYC1*	(73)
TH_5187	R1158 *pSEC63*::*KanMX*-tetO$_7$-*pCYC1*	(73)
ySI7	BY4741 *Sbh1Δ*::*KanMX osw1Δ*::*HphMX*:: *SBH1*-15xGS-*SEC63*-TEV-GFP::*NatMX*	This study (68)
ySI8	ySI7 *SEC61*(PM)*::LEU2*	This study (91)
ySI42	TH_5187 *SEC61*(PM)::*NatMX*	This study (91)
ySI48	TH_5187 *sbh1Δ*::*HphMX*	This study (91)
ySI62	R1158 *pSEC62*::*KanMX*-tetO$_7$-*pCYC1*	This study (91)
ySI67	yMLT62 *ura3-0*::*pGAL1-Tl*Sec::*NatMX*	This study (91)
ySI73	ySI48 *HO*::*SEC63*(E440R/F481S/440Δ7)::*LEU2*	This study (91)
ySI74	ySI42 *sbh1Δ*::*HphMX* *HO*::*SEC63*(E440R/F481S/440Δ7)::*LEU2*	This study (91)
ySI77	yMLT62 *ura3-0*:: *pGAL1-Tl*Sec(Δ*SEC62*)::*NatMX*	This study (91)
ySI89	TH_4087 *SEC63*(E440R/F481S/440Δ7)::*NatMX*,	This study (91)
ySI112	ySI48 *HO*::*SEC63*(E440R/F481S/440Δ7/Δ210-216)::*LEU2*	This study (91)
ySI113	yMLT62 *ura3-0*::*pGAL1- Tl*Sec(Δanchor)::*NatMX*	This study (91)
Plasmids		
pYTK-001	MoClo YTK part plasmid entry vector	(75)
pYTK-095	MoClo YTK AmpR-ColE1 vector	(75)
pYTK-e101	*URA3* integration vector containing a natMX expression cassette	This study (91)
pYTK-e106	*HO* integration vector containing a *LEU2* marker	This study (91)
pYTK-e112	CEN/ARS vector containing a *LEU2* marker	This study (91)
pSI74	pYTK-e106 *Sc*Sbh1-15xGS-*Sc*Sec63 (E440R/F481S/441Δ7)-TEV-GFP (with endogenous Sec63 promoter)	This study (91)
pSI120	pYTK-e106 *Sc*Sbh1-15xGS-*Sc*Sec63-FN3mut/Δ210-216-TEV-GFP (with endogenous Sec63 promoter)	This study (91)
pSI123	pYTK-e112 *Sc*Sec61 (with endogenous Sec61 promoter)	This study (91)
pSI39	pYTK-e112 *Sc*Sec62 (with endogenous Sec62 promoter)	This study (91)
pSI5	pYTK-e112 *Sc*Sec63 (with endogenous Sec63 promoter)	This study (91)
pSI16	pYTK-e112 *Sc*Sec63 (E440R/F481S/441Δ7) (with endogenous Sec63 promoter)	This study (91)
pSI17	pYTK-e112 *Sc*Sec63-TEV-GFP (with endogenous Sec63 promoter)	This study (91)
pSI65	pYTK-e101 *Tl*Sec (each subunit under a *GAL1* promoter)	This study (91)
pSI87	pYTK-e101 ΔSec62-*Tl*Sec (without Sec62)	This study (91)
pSI94	pYTK-e101 Δanchor-*Tl*Sec (with an anchor domain deletion mutant of Sec62)	This study (91)

Chapter Four

Final conclusions and future directions

Our study allowed us to propose a highly polished model for how the Sec61 channel gating is regulated in the post-translational translocation mode. Nevertheless, some questions remain unresolved. When we published our papers, two other papers on the yeast Sec complex were also published (66,92). While the overall structural observations were similar, their structures showed somewhat different conformations, leading them to propose partly different models. The most notable difference is the state of the plug in the Sec complex. While we concluded that the plug is displaced by Sec62, the study from the Rapoport lab reported a closed plug in the presence of Sec62 (66). Although we believe that this discrepancy could be explained by a relatively high heterogeneity of the sample in the Rapoport lab's study and incomplete particle classifications, it is important to note that this issue would need further investigations, in particularly in the context of the native membrane environment. The second study, from the Beckmann lab, used cryo-EM to obtain a substrate engaged map of the yeast Sec complex (92). Although they assumed the plug would remain closed before engaging with a substrate polypeptide, the positions of Sec62 TMs and the model that the signal sequence would egress through TM2 of Sec62 are consistent with our model.

One notable difference in the sample preparation between our labs is the fact that we utilized different detergents to solubilize our samples. One way to simulate a near native membrane environment would be to reanalyze the structural conformations of the Sec complex reconstituted in a nanodisc. Our efforts to obtain meaningful data with such samples have been unsuccessful due to several reasons. First, reconstitution efficiency was low, which yielded micrographs with very few particles. Second, we encountered a significant degree of preferred particle orientations in the images. Last, upon inspection of the three-dimensional reconstructions we saw that Sec62 was significantly destabilized in small diameter nanodiscs. Therefore, while this approach is promising, it will require a significant degree of optimization.

Perhaps one of the most exciting recent developments in structural biology is the advent of AlphaFold2 (93). Although mechanistically AlphaFold2 does not provide much insight to the channel function, it is able to predict the general structure of the Sec complex incredibly accurately. With it, we were able to obtain a model for the complete Sec62 protein that fits our densities accurately, and agrees with the crystal structure of the N-terminal domain (92). Using AlphaFold2 we can propose a full structural model of the Sec complex for the first time (Fig. 4.1).

Even with this new information, the structure of Sec62 remains mysterious to some degree. We were able to propose functions for the TMs and the anchor domain, but the function of the cytosolic N- and C-terminal domains is unclear. The ends of the protein are known to be important for binding to Sec63 through electrostatic interactions (69), but this interaction is unfortunately not captured in the AlphaFold2 model. Additionally, the large globular N-terminal domain is not essential for yeast viability (69). Nevertheless, it would be interesting to understand what function, if any, it serves. With the structural

information, targeted mutagenesis can be more refined and allow researchers to probe Sec62 in a spatially specific manner.

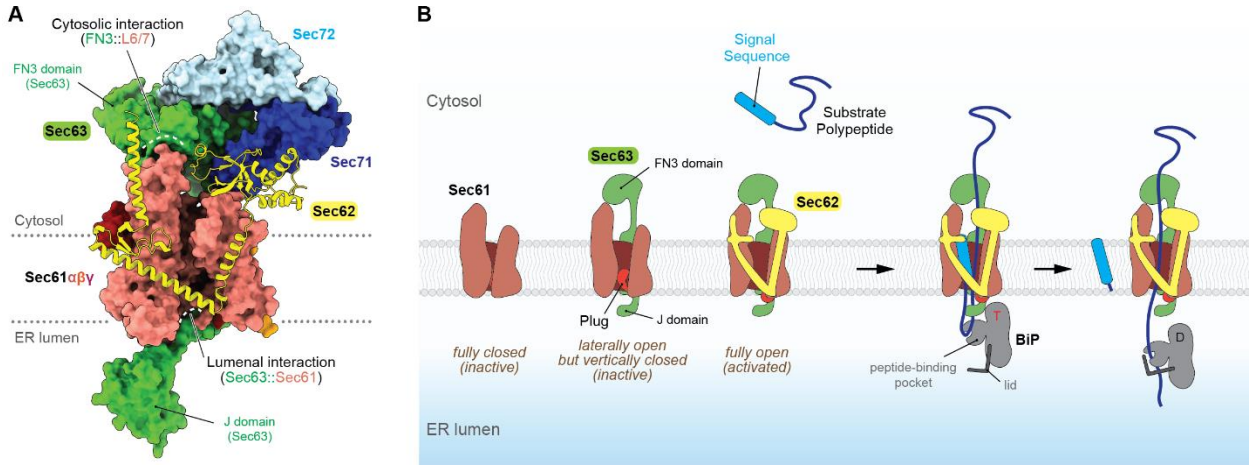

Figure 4.1 Structure of the Sec complex and mechanism of eukaryotic post-translational protein translocation. A. Structure of the Sec complex from yeast (PDB 7KAI; (91)). Shown is a front view, seen from the membrane onto the lateral gate. Sec63 (green) binds to the Sec61 complex from the back. Key allosteric interactions with Sec61 are indicated with white dashed curves. Sec62 (yellow) is shown in a ribbon representation. Note that the lateral gate of Sec61 is open. Sec71 (dark blue) and Sec72 (light blue) are fungal-specific proteins and absent in higher eukaryotes. Sec62 and the J domain of Sec63 were modeled by AlphaFold2 (93) and fit into the cryo-EM density map. **B.** Mechanism of post-translational translocation in eukaryotes. Both Sec63 and Sec62 are required to fully activate (open) the Sec61 channel. The client protein inserts into the activated channel. There is a gap between Sec62 and the lateral gate of Sec61 through which the signal sequence is expected to leave. The signal sequence is cleaved by the signal peptidase (not shown) at some point during the translocation. The ER-resident Hsp70 BiP transiently interacts with the J domain of Sec63, and this triggers hydrolysis of ATP bound to BiP (indicated by "T") to ADP (indicated by "D"). In the ADP-bound state, the lid of BiP closes, causing a tight association of BiP to the client polypeptide. This prevents the polypeptide from sliding back to the cytosol, thus providing a driving force for forward translocation.

The structure of the human Sec61 channel and Sec complex are likely to mirror our findings with the fungal complexes because of large degree of homology, and AlphaFold2 predictions recapitulate this idea. Nevertheless, careful study of the human channel would still be valuable because numerous Sec61 inhibitors have been considered as potentially useful for therapeutic purposes (94). Such inhibitors include cyclic heptadepsipeptides called cotransins (95–97), decatransin (98), apratoxin A (99), mycolactone (100–102), ipomoeassin F (103), and coibamide A (104). The list of inhibitors is likely to continue to expand, and these small molecules and their derivatives carry a potential to function as effective tumor suppressors, antiviral, and antibacterial drugs. The current studies on the mode of action of these inhibitors relies on mutagenesis experimentation and their effect on drug resistance. This approach is only able to estimate the position of the inhibitor binding pocket. Currently, the majority of the mutagenesis analyses have been done around the cytosol-facing funnel of Sec61, and although a clear binding pocket remains unknown several residues have been reported to be critical for drug resistance (94). Cotransins and decatransin have been thought to stabilize a certain

closed conformation of the Sec61 channel, based on the observations that resistant mutations are mostly localized in the plug and the lateral gate (98,105). In contrast, a recent cryo-EM study of a mycolactone-bound Sec61 complex has reported that mycolactone intercalates into the open lateral gate, potentially hindering the insertion of the signal sequence or anchor into the channel (106). Nevertheless, due to limited resolution of the structure, detailed molecular interactions between mycolactone and the channel remain to be determined. Accurate structural data would be critical for a more complete understanding of the drug inhibition mechanism and for further structure-based drug design.

References

1. Blobel G, Sabatini DD. Ribosome-Membrane Interaction In Eukariotic Cells. Biomembranes. 1971. 193–195 p.
2. Van Den Berg B, Clemons WM, Collinson I, Modis Y, Hartmann E, Harrison SC, et al. X-ray structure of a protein-conducting channel. Nature. 2004;427(6969):36–44.
3. VON HEIJNE G. Patterns of Amino Acids near Signal-Sequence Cleavage Sites. Eur J Biochem. 1983;133(1):17–21.
4. von Heijne G. Signal Sequences The Limits of Variation. J Mol Biol. 1985;(184):99–105.
5. Blobel G, Dobberstein B. Transfer of proteins across membranes. I. Presence of proteolytically processed and unprocessed nascent immunoglobulin light chains on membrane-bound ribosomes of murine myeloma. 1975;67:835–51.
6. Friedlander M, Blobel G. Bovine opsin has more than one signal sequence. 1985;318(6044):338–43.
7. Park E, Rapoport TA. Preserving the membrane barrier for small molecules during bacterial protein translocation. Nature. 2011;473(7346):239–42.
8. Ma C, Wu X, Sun D, Park E, Catipovic MA, Rapoport TA, et al. protein translocation machine. Nat Commun [Internet]. (2019):1–9. Available from: http://dx.doi.org/10.1038/s41467-019-10918-2
9. Zimmer J, Nam Y, Rapoport TA. Structure of a complex of the ATPase SecA and the protein-translocation channel. 2008;455:936–42.
10. Tsukazaki T, Mori H, Fukai S, Ishitani R, Mori T, Dohmae N, et al. Conformational transition of Sec machinery inferred from bacterial SecYE structures. Nature. 2008;455(7215):988–91.
11. Li L, Park E, Ling J, Ingram J, Ploegh H, Rapoport TA. Crystal structure of a substrate-engaged SecY protein-translocation channel. Nature. 2016;531(7594):395–9.
12. Voorhees RM, Ferna IS. Structure of the Mammalian Ribosome-Sec61 Complex to 3.4A Resolution. 2014;157:1632–43.
13. Voorhees RM, Hegde RS. Structure of the Sec61 channel Opened By a Signal Sequence. Science (80-). 2016;351(6268):88–91.
14. Gogala M, Becker T, Beckmann R, Berninghausen O, Beatrix B, Armache J-P, et al. Structures of the Sec61 complex engaged in nascent peptide translocation or membrane insertion. Nature [Internet]. 2014;506(7486):107–10. Available from: http://dx.doi.org/10.1038/nature12950
15. Walter P, Blobel G. Purification of a membrane-associated protein complex required for protein translocation across the endoplasmic reticulum Biochemistry : Proc Natl Acad Sci U S A. 1980;77(12):7112–6.
16. Walter P, Blobel G. Translocation of Proteins Across the Endoplasmic Reticulum II . Signal Recognition Protein (SRP) Mediates the Selective Binding to Microsomal Membranes of In-Vitro- Assembled Polysomes Synthesizing Secretory Protein. J c. 1981;91:551–6.

17. Gilmore R, Blobel G, Walter P. Protein Translocation Across the Endoplasmic Reticulum . I . Detection in the Microsomal Membrane of a Receptor for the Signal Recognition Particle. J Cell Biol. 1982;95:463–9.
18. Gilmore R, Walter P, Blobel G. Protein Translocation Across the Endoplasmic Reticulum . II . Isolation and Characterization of the Signal Recognition Particle Receptor. J Cell Biol. 1982;95:470–7.
19. Rothblatt JA, Deshaies RJ, Sanders SL, Daum G, Schekman R. Multiple genes are required for proper insertion of secretory proteins into the endoplasmic reticulum in yeast. J Cell Biol. 1989;109(6 I):2641–52.
20. Deshaies RJ, Sanders SL, Feldheim DA, Schekman R. Assembly of yeast Sec proteins involved in translocation into the endoplasmic reticulum into a membrane-bound multisubunit complex. Nature. 1991;349(6312):806–8.
21. Tripathi A, Mandon EC, Gilmore R, Rapoport TA. Two alternative binding mechanisms connect the protein translocation Sec71-Sec72 complex with heat shock proteins. 2017;292:8007–18.
22. Panzner S, Dreier L, Hartmann E, Kostka S, Rapoport TA. Posttranslational Protein Transport in Yeast Reconstituted with a Purified Complex of Set Proteins and Kar2p. 1995;61:561–70.
23. Matlack KES, Misselwitz B, Plath K, Rapoport TA. BiP Acts as a Molecular Ratchet during Posttranslational Transport of Prepro- alpha Factor across the ER Membrane. 1999;97:553–64.
24. Chitwood PJ, Juszkiewicz S, Guna A, Shao S, Hegde RS, Chitwood PJ, et al. Article EMC Is Required to Initiate Accurate Membrane Protein Topogenesis Article EMC Is Required to Initiate Accurate Membrane Protein Topogenesis. Cell [Internet]. 2018;175(6):1507-1519.e16. Available from: https://doi.org/10.1016/j.cell.2018.10.009
25. Guna A, Volkmar N, Christianson JC, Hegde RS. The ER membrane protein complex is a transmembrane domain insertase. 2018;(January):1–5.
26. Liaci AM, Steigenberger B, Cesar P, Souza T De, Marrink SJ, Scheltema RA, et al. Article Structure of the human signal peptidase complex reveals the determinants for signal peptide cleavage ll Article Structure of the human signal peptidase complex reveals the determinants for signal peptide cleavage. 2021;3934–48.
27. Kalies K-U, Rapoport TA, Hartmann E. The beta Subunit of the Sec61 Complex Facilitates Cotranslational Protein Transport and Interacts with the Signal Peptidase during Translocation. J Cell Biol. 1998;141(4):887–94.
28. Shrimal S, Cherepanova NA, Gilmore R. Seminars in Cell & Developmental Biology Cotranslational and posttranslocational N -glycosylation of proteins in the endoplasmic reticulum. Semin Cell Dev Biol [Internet]. 2015;41:71–8. Available from: http://dx.doi.org/10.1016/j.semcdb.2014.11.005
29. Wiedmann M, Kurzchalia T V, Hartmann E, Rapoport TA. A signal sequence receptor in the endoplasmic reticulum membrane. 1987;328:4–7.
30. Fons RD, Bogert BA, Hegde RS. Substrate-specific function of the translocon-associated across the ER membrane. 2003;160(4):529–39.
31. Losfeld ME, Ng BG, Kircher M, Buckingham KJ, Turner EH, Eroshkin A, et al. A new congenital disorder of glycosylation caused by a mutation in SSR4 , the

signal sequence receptor 4 protein of the TRAP complex. 2014;23(6):1602–5.
32. Sommer N, Junne T, Kalies K, Spiess M, Hartmann E. Biochimica et Biophysica Acta TRAP assists membrane protein topogenesis at the mammalian ER membrane. BBAMCR [Internet]. 2013;1833(12):3104–11. Available from: http://dx.doi.org/10.1016/j.bbamcr.2013.08.018
33. Hegde RS, Keenan RJ. The mechanisms of integral membrane protein biogenesis. Nat Rev Mol Cell Biol. 2022;23(2):107–24.
34. Mckenna M, Sim SS, Ordureau A, Wei L, Harper W, Shao S, et al. The endoplasmic reticulum P5A-ATPase is a transmembrane helix dislocase. 2020;369(6511).
35. Braunger K, Pfeffer S, Shrimal S, Gilmore R, Berninghausen O, Mandon EC, et al. Structural basis for coupling protein transport and N-glycosylation at the mammalian endoplasmic reticulum. Science (80-). 2018;360(6385):215–9.
36. Feldheim D, Rothblatt J, Schekman R. Topology and functional domains of Sec63p, an endoplasmic reticulum membrane protein required for secretory protein translocation. Mol Cell Biol. 1992;12(7):3288–96.
37. Brodsky JL, Schekman R. A Sec63p-BiP Complex from Yeast Is Required for Protein Translocation in a Reconstituted Proteoliposome. 1993;123(6):1355–63.
38. Matlack KES, Plath K, Misselwitz B, Rapoport TA. Protein Transport by Purified Yeast Sec Complex and Kar2p Without Membranes. 1997;277(August).
39. Nguyen THD, Li J, Galej WP, Oshikane H, Newman AJ, Nagai K. Structural basis of Brr2-Prp8 interactions and implications for U5 snRNP biogenesis and the spliceosome active site. Structure [Internet]. 2013;21(6):910–9. Available from: http://dx.doi.org/10.1016/j.str.2013.04.017
40. Cheng Z, Jiang Y, Mandon EC, Gilmore R. Identification of cytoplasmic residues of Sec61p involved in ribosome binding and cotranslational translocation. J Cell Biol. 2005;168(1):67–77.
41. Becker T, Bhushan S, Jarasch A, Armache JP, Funes S, Jossinet F, et al. Structure of monomeric yeast and mammalian Sec61 complexes interacting with the translating ribosome. Science (80-). 2009;326(5958):1369–73.
42. Meyer HA, Grau H, Kraft R, Kostka S, Prehn S, Kalies KU, et al. Mammalian Sec61 is associated with Sec62 and Sec63. J Biol Chem [Internet]. 2000;275(19):14550–7. Available from: http://dx.doi.org/10.1074/jbc.275.19.14550
43. Egea PF, Stroud RM. Lateral opening of a translocon upon entry of protein suggests the mechanism of insertion into membranes. Proc Natl Acad Sci U S A. 2010;107(40):17182–7.
44. Heritage D, Wonderlin WF. Translocon Pores in the Endoplasmic Reticulum Are Permeable to a Neutral, Polar Molecule. J Biol Chem [Internet]. 2001;276(25):22655–62. Available from: http://dx.doi.org/10.1074/jbc.M102409200
45. Hughes TR, Marton MJ, Jones AR, Roberts CJ, Stoughton R, Armour CD, et al. Functional Discovery via a Compendium of Expression Profiles. Cell. 2000;102(1):109–26.
46. Kityk R, Kopp J, Mayer MP. Molecular Mechanism of J-Domain-Triggered ATP Hydrolysis by Hsp70 Chaperones. Mol Cell. 2018;(69):227–37.
47. Ng DTW, Brown JD, Walter P. Signal sequences specify the targeting route to the

endoplasmic reticulum membrane. J Cell Biol. 1996;134(2):269–78.
48. Smith MA, Clemons WM, DeMars CJ, Flower AM. Modeling the effects of prl mutations on the Escherichia coli SecY complex. J Bacteriol. 2005;187(18):6454–65.
49. Trueman SF, Mandon EC, Gilmore R. A gating motif in the translocation channel sets the hydrophobicity threshold for signal sequence function. J Cell Biol. 2012;199(6):907–18.
50. Mastronarde DN. Automated electron microscope tomography using robust prediction of specimen movements. J Struct Biol. 2005;152(1):36–51.
51. Zheng SQ, Palovcak E, Armache JP, Verba KA, Cheng Y, Agard DA. MotionCor2: Anisotropic correction of beam-induced motion for improved cryo-electron microscopy. Nat Methods. 2017;14(4):331–2.
52. Punjani A, Rubinstein JL, Fleet DJ, Brubaker MA. CryoSPARC: Algorithms for rapid unsupervised cryo-EM structure determination. Nat Methods. 2017;14(3):290–6.
53. Rohou A, Grigorieff N. CTFFIND4: Fast and accurate defocus estimation from electron micrographs. J Struct Biol. 2015;192(2):216–21.
54. Emsley P, Lohkamp B, Scott WG, Cowtan K. Features and development of Coot. Acta Crystallogr Sect D Biol Crystallogr. 2010;66(4):486–501.
55. Afonine P V., Poon BK, Read RJ, Sobolev O V., Terwilliger TC, Urzhumtsev A, et al. Real-space refinement in PHENIX for cryo-EM and crystallography. Acta Crystallogr Sect D Struct Biol. 2018;74(6):531–44.
56. Chen VB, Arendall WB, Headd JJ, Keedy DA, Immormino RM, Kapral GJ, et al. MolProbity: All-atom structure validation for macromolecular crystallography. Acta Crystallogr Sect D Biol Crystallogr. 2010;66(1):12–21.
57. Barad BA, Echols N, Wang RYR, Cheng Y, Dimaio F, Adams PD, et al. EMRinger: Side chain-directed model and map validation for 3D cryo-electron microscopy. Nat Methods. 2015;12(10):943–6.
58. Baker NA, Sept D, Joseph S, Holst MJ, McCammon JA. Electrostatics of nanosystems: Application to microtubules and the ribosome. Proc Natl Acad Sci U S A. 2001;98(18):10037–41.
59. Pettersen EF, Goddard TD, Huang CC, Couch GS, Greenblatt DM, Meng EC, et al. UCSF Chimera - A visualization system for exploratory research and analysis. J Comput Chem. 2004;25(13):1605–12.
60. Gumbart J, Chipot C, Schulten K. Free Energy of Nascent-Chain Folding in the Translocon. 2011;7602–7.
61. Park E, Me J, Akey CW. Structure of the SecY channel during initiation of protein translocation ´. 2014;
62. Pfeffer S, Burbaum L, Unverdorben P, Pech M, Chen Y, Zimmermann R, et al. Structure of the native Sec61 protein-conducting channel. 2015;1–7.
63. Flower AM, Osborne RS, Silhavy TJ. double mutants predicts interactive domains of. 1995;14(5):884–93.
64. Harris CR, Silhavy TJ. Mapping an Interface of SecY (PrlA) and SecE (PrlG) by Using Synthetic Phenotypes and In Vivo Cross-Linking. 1999;181(11):3438–44.
65. Hizlan D, Robson A, Whitehouse S, Gold VA, Vonck J, Mills D, et al. Report Structure of the SecY Complex Unlocked by a Preprotein Mimic. 2012;21–8.

66. Wu X, Cabanos C, Rapoport TA. Structure of the post-translational protein translocation machinery of the ER membrane. Nature. 2019;566(7742):136–9.
67. Tanaka Y, Sugano Y, Takemoto M, Mori T, Furukawa A, Kusakizako T, et al. Crystal Structures of SecYEG in Lipidic Cubic Phase Elucidate a Precise Resting and a Peptide-Bound State. Cell Rep [Internet]. 2015;13(8):1561–8. Available from: http://dx.doi.org/10.1016/j.celrep.2015.10.025
68. Itskanov S, Park E. Structure of the posttranslational Sec protein-translocation channel complex from yeast. Science (80-). 2019;363(6422):84–7.
69. Wittke S, Dunnwald M, Johnsson N. Sec62p, A Component of the Endoplasmic Reticulum Protein Translocation Machinery, Contains Multiple Binding Sites for the Sec-Complex. Mol Biol Cell. 2000;11(11):3859–71.
70. Willer M, Jermy AJ, Young BP, Stirling CJ. Identification of novel protein – protein interactions at the cytosolic surface of the Sec63 complex in the yeast ER membrane. 2003;133–48.
71. Deshaies RJ, Schekman R. SEC62 Encodes a Putative Membrane Protein Required for Protein Translocation into the Yeast Endoplasmic Reticulum. 1989;109(6):2653–64.
72. Voorhees RM, Hegde RS. Toward a structural understanding of co-translational protein translocation. Curr Opin Cell Biol [Internet]. 2016;41:91–9. Available from: http://dx.doi.org/10.1016/j.ceb.2016.04.009
73. Kater L, Frieg B, Kedrov A, Berninghausen O, Gohlke H, Beckmann R. Partially inserted nascent chain unzips the lateral gate of the Sec translocon. 2019;1–13.
74. Hentges P, Driessche B Van, Tafforeau L, Vandenhaute J, Carr AM. Three novel antibiotic marker cassettes for gene disruption and marker switching in Schizosaccharomyces pombe. 2005;1013–9.
75. McIsaac RS, Silverman SJ, McClean MN, Gibney PA, Macinskas J, Hickman MJ, et al. Fast-acting and nearly gratuitous induction of gene expression and protein depletion in Saccharomyces cerevisiae. Mol Biol Cell. 2011;22(22):4447–59.
76. Lee ME, Deloache WC, Cervantes B, Dueber JE. A Highly Characterized Yeast Toolkit for Modular, Multipart Assembly. 2015;
77. Tegunov D, Cramer P. preprocessing with Warp. Nat Methods [Internet]. 2019;16(November). Available from: http://dx.doi.org/10.1038/s41592-019-0580-y
78. Waterhouse A, Bertoni M, Bienert S, Studer G, Tauriello G, Gumienny R, et al. SWISS-MODEL : homology modelling of protein structures and complexes. 2018;46(May):296–303.
79. Goddard TD, Huang CC, Meng EC, Pettersen EF, Couch GS, Morris JH, et al. TOOLS FOR PROTEIN SCIENCE UCSF ChimeraX : Meeting modern challenges in visualization and analysis. 2018;27:14–25.
80. Trabuco LG, Villa E, Mitra K, Frank J, Schulten K. Technical Advance Flexible Fitting of Atomic Structures into Electron Microscopy Maps Using Molecular Dynamics. 2008;(May):673–83.
81. Jo S, Kim T, Iyer VG, Im W. Software News and Updates CHARMM-GUI : A Web-Based Graphical User Interface for CHARMM. 2008;
82. Wu EL, Cheng X, Jo S, Rui H, Song KC. CHARMM-GUI Membrane Builder Toward Realistic Biological Membrane Simulations. 2014;1997–2004.
83. Jorgensen WL, Chandrasekhar J, Madura JD. Comparison of simple potential

functions for simulating liquid water liquid water. 1983;926(March 1983).
84. Phillips JC, Braun R, Wang WEI, Gumbart J, Tajkhorshid E, Villa E, et al. Scalable Molecular Dynamics with NAMD. 2005;
85. Best RB, Zhu X, Shim J, Lopes PE, Mittal J, Feig M, et al. Optimization of the additive CHARMM all-atom protein force field targeting improved sampling of the backbone φ, ψ and side- chain χ1 and χ2 dihedral angles. 2012;8(9):3257–73.
86. Huang J, Rauscher S, Nawrocki G, Ran T, Feig M, Groot BL De, et al. CHARMM36m : an improved force field for folded and intrinsically disordered proteins. 2017;14(1).
87. Klauda JB, Venable RM, Freites JA, Connor JWO, Tobias DJ, Mondragon-ramirez C, et al. Update of the CHARMM All-Atom Additive Force Field for Lipids : Validation on Six Lipid Types. 2010;2:7830–43.
88. Balusek C, Hwang H, Lau CH, Lundquist K, Hazel A, Lynch DL, et al. HHS Public Access. 2019;15(8):4673–86.
89. Darden T, York D, Pedersen L. Particle mesh Ewald : An N · log (N) method for Ewald sums in large systems in large systems. 1993;98(April 1993):10089–92.
90. Humphrey W, Dalke A, Schulten K. VMD : Visual Molecular Dynamics. 1996;7855(October 1995):33–8.
91. Itskanov S, Kuo KM, Gumbart JC, Park E. Stepwise gating of the Sec61 protein-conducting channel by Sec63 and Sec62. Nat Struct Mol Biol [Internet]. Available from: http://dx.doi.org/10.1038/s41594-020-00541-x
92. Weng T, Steinchen W, Beatrix B, Berninghausen O, Becker T, Bange G, et al. Architecture of the active post-translational Sec translocon. EMBO J. 2021;40(3):1–12.
93. Jumper J, Evans R, Pritzel A, Green T, Figurnov M, Ronneberger O, et al. Highly accurate protein structure prediction with AlphaFold. Nature [Internet]. 2021;596(7873):583–9. Available from: http://dx.doi.org/10.1038/s41586-021-03819-2
94. Pauwels E, Schülein R, Vermeire K. Inhibitors of the Sec61 Complex and Novel High Throughput Screening Strategies to Target the Protein Translocation Pathway. 2021;
95. Besemer J, Harant H, Wang S, Oberhauser B, Marquardt K, Foster CA, et al. Selective inhibition of cotranslational translocation of vascular cell adhesion molecule 1. Nature. 2005;436(July):290–3.
96. Garrison JL, Kunkel EJ, Hegde RS, Taunton J. A substrate-specific inhibitor of protein translocation into the endoplasmic reticulum. Nature. 2005;436(July):285–9.
97. Mackinnon AL, Garrison JL, Hegde RS, Taunton J. Photo-Leucine Incorporation Reveals the Target of a Cyclodepsipeptide Inhibitor of Cotranslational Translocation. 2007;14560–1.
98. Junne T, Wong J, Studer C, Aust T, Bauer BW, Beibel M, et al. Decatransin , a new natural product inhibiting protein translocation at the Sec61 / SecYEG translocon. 2015;1217–29.
99. Paatero AO, Kellosalo J, Dunyak BM, Gerwick WH, Taunton J, Paavilainen VO, et al. Apratoxin Kills Cells by Direct Blockade of the Sec61 Protein Translocation Channel Brief Communication Apratoxin Kills Cells by Direct Blockade of the

Sec61 Protein Translocation Channel. Cell Chem Biol [Internet]. 2016;23(5):561–6. Available from: http://dx.doi.org/10.1016/j.chembiol.2016.04.008
100. Hall BS, Hill K, Mckenna M, Ogbechi J, High S, Willis AE, et al. The Pathogenic Mechanism of the Mycobacterium ulcerans Virulence Factor , Mycolactone , Depends on Blockade of Protein Translocation into the ER. 2014;10(4):15–7.
101. Mckenna M, Simmonds RE, High S. Mechanistic insights into the inhibition of Sec61-dependent co- and post-translational translocation by mycolactone. 2016;1:1404–15.
102. Baron L, Paatero AO, Morel JD, Impens F, Macé LG, Auret S Saint, et al. Mycolactone subverts immunity by selectively blocking the Sec61 translocon. J Exp Med. 2016;2885–96.
103. Zong G, Hu Z, Keefe SO, Tranter D, Iannotti MJ, Baron L, et al. Ipomoeassin F Binds Sec61 α to Inhibit Protein Translocation. 2019;
104. Tranter D, Paatero AO, Kawaguchi S, Kazemi S, Serrill D, Kellosalo J, et al. Coibamide A Targets Sec61 to Prevent Biogenesis of Secretory and Membrane Proteins. 2020;
105. MacKinnon AL, Paavilainen VO, Sharma A, Hegde RS, Taunton J. An allosteric Sec61 inhibitor traps nascent transmembrane helices at the lateral gate. Elife. 2014;2014(3):1–23.
106. Gerard SF, Hall BS, Zaki AM, Corfield KA, Mayerhofer PU, Costa C, et al. Article Structure of the Inhibited State of the Sec Translocon ll Structure of the Inhibited State of the Sec Translocon. Mol Cell. 2020;(79):406–15.